Integrated study of active and passive mechanisms associated with insect flapping flights

昆虫羽ばたき飛行における能動的・受動的原理の統合的研究

August 2021

XUEFEI CAI

Graduate School of
Science and Engineering
CHIBA UNIVERSITY

（千葉大学審査学位論文）

Integrated study of active and passive mechanisms associated with insect flapping flights

昆虫羽ばたき飛行における能動的・受動的原理の統合的研究

August 2021

XUEFEI CAI

Graduate School of
Science and Engineering
CHIBA UNIVERSITY

Abstract

Flying insects are masters of agile and robust flights in various complex environments. Flapping-wing flights in insects is achieved through a closed-loop system via integral of an internal working system comprising sensorimotor neurobiology and muscoloskeletal mechanics and an external mechanical system featured by multiple mechanical interactions.

To tackle a central problem of active and passive mechanisms associated with insect flight, we developed an integrated simulation-based framework, which consists of a fully nonlinear dynamic model, capable of modeling flapping-wing dynamics and aerodynamics in free or trimmed flights with flexible wing hinges, and a computational fluid dynamics (CFD) data-driven aerodynamic model (CDAM), which is proposed for fast and precise prediction of flapping unsteady aerodynamics in various flight velocities and wing kinematics, serving as an alternative to expensive CFD simulations.

With the simulator, we first investigated whether elastic storage enables robustness of flapping wing dynamics through fluid-structure interaction modeling that couples unsteady flapping aerodynamics and torsional-spring-based elastic wing-hinge dynamics to determine passive and active mechanisms in bumblebee hovering. We find that a strategy of active-controlled stroke, passive-controlled wing pitch and deviation achieves optimal elastic storage, and the flapping-wing dynamics displays robustness in producing aerodynamic force while achieving high power efficiency over a broad range of wing-hinge stiffness.

We then established a control-theoretic analysis framework based on a proportional-derivative (PD) control strategy in terms of Laplace transformation and root locus method and discovered that a fast or minimized flight stabilization can be achieved through passive aerodynamic damping and neural feedback delay, universally in various insects and hummingbird. We further found that a bioinspired PD controller is suitable for longitudinal and full 6 DoF flight control even under large perturbations.

Acknowledgement

Throughout the writing of this dissertation I have received a great deal of support and assistance.

First and foremost, I am extremely grateful to my supervisor, Prof. Hao Liu, director of the Center for Aerial Intelligent Vehicles, whose expertise was invaluable in formulating the research questions and methodology. His immense knowledge and plentiful experience have encouraged me in all the time of my academic research.

I sincerely thank Dr. Dmitry Kolomenskiy and Prof. Toshiyuki Nakata for giving the encouragement, sharing insightful suggestions and improving my writing skills. They provide me with the tools that I needed to choose the right direction and successfully complete my dissertation.

I would like to thank Dr. Ru Xu for the wonderful collaboration and giving me many helps in the past three years, and Mr. Yuma Yoshinaga for helping me adapt to the life in Japan.

I would also like to thank all the members in our lab for their help, support and the fun-time we spent together.

In addition, I must express my very profound gratitude to my parents, my sister and my two cute nieces for providing me with unfailing support and continuous encouragement throughout my years of study.

On a more personal level, I must thank my patient and understanding girlfriend Chen. Her comfort and encouragement through daily phone calls give me the courage and confidence to accomplish my study.

This work was supported by the Japan Society for the Promotion of Science (JSPS) (KAKENHI No. 19H02060 and No. 18K13693) and the Excellent International Student Scholarship provided by Chiba University.

Xuefei Cai
Chiba University
May 2021

Content

Abstract i

Acknowledgement i

Nomenclature v

1 Introduction 1

1.1 Insect Flights 1

1.2 Flapping aerodynamics of insects 2

1.3 Passive and active perspectives in flapping flights 3

1.4 Objective and approach 4

References 4

2 Simulation-based framework of flapping flight 7

2.1 Introduction 7

2.2 CFD data-driven aerodynamic model (CDAM) 8

2.2.1 Nomenclature and coordinate system 9

2.2.2 Quasi-steady model for flapping wing 10

2.2.3 Simplified aerodynamic model for moving body 13

2.2.4 A CFD simulator for insect flight 14

2.3 Construction of CFD database 16

2.4 Accuracy validation on CDAM 17

2.4.1 Quasi-steady model for flapping wing 17

2.4.2 Simplified aerodynamic model for moving body 19

2.4.3 Aerodynamic performance of CDAM of bumblebee 19

2.5 Discussion 19

2.5.1 Aerodynamics of forward flight condition 19

2.5.2 Trim state of modeled bumblebee in forward flight 20

2.6 Fully nonlinear dynamic model 22

2.6.1 Dynamic model establishment 22

2.6.2 Time independence validation 25

References 25

List of figures 29

List of tables 42

3 Effects of wing hinge flexibility 46

3.1 Introduction 46

3.2 Flexibility of the wing hinge in bumblebee 46

3.3 Aerodynamics of passive feathering and elevation 49
References 52
List of figures 54
4 Fast stabilization control 58
4.1 Introduction 58
4.2 Flapping flight dynamics 60
4.3 Closed-loop time constant 61
4.4 Restoring process under perturbations 62
4.5 Results 64
4.5.1 Effects of aerodynamic damping 64
4.5.2 Oscillatory mode can accelerate stabilization 64
4.5.3 Restoring time 65
4.5.4 Generalization to other species 66
4.6 Discussions 67
4.6.1 Effects of aerodynamic damping and time delay 67
4.6.2 Multi-degree stabilization 68
4.6.3 The role of aerodynamic damping 70
4.6.4 Compare P, D and PD control 71
References 72
List of figures 76
List of tables 83
5 Bioinspired PD controller 84
5.1 Introduction 84
5.2 Longitudinal stabilization control for hovering bumblebee 85
5.2.1 Construction of longitudinal PD controller 85
5.2.2 Implementation of PD controller 89
5.2.3 Validation on the longitudinal PD controller 89
5.3 Full six-degree-of-freedom stabilization control for hovering bumblebee 91
5.3.1 Construction of 6 DoF PD controller 91
5.3.2 Stabilization control under small perturbations 97
5.3.3 Flight stabilization with large perturbations 98
References 100
List of figures 104
List of tables 113
6 Concluding remarks and future tasks 114

6.1 Conclusions......114
6.2 Future tasks......115
    6.2.1 Implementations to FMAVs......115
    6.2.2 Active and passive roles of insect body......115
References......115
Appendix......117

Nomenclature

${}_{g}\cdot$	quantity expressed in ground frame
${}_{b}\cdot$	quantity expressed in body-fixed frame
${}_{sp}\cdot$	quantity expressed in stroke plane frame
${}_{w}\cdot$	quantity expressed in wing-fixed frame
$\cdot_{\cdot R}$	quantity of right wing
$\cdot_{\cdot L}$	quantity of left wing
θ_{SP}	stroke plane angle
φ	positional angle
θ	elevation angle
η	feathering angle
ψ	body yaw angle
χ	body pitch angle
ρ	body roll angle
g	gravity acceleration
α	angle of attack of flapping wing
λ	angle of attack of moving body; pseudo-compressibility coefficient
ρ_{aero}	density of air
m_b	body mass
m_w	wing mass
m_t	total mass $m_b + 2m_w$
${}_{w}I_{w}$	moment of inertia of wing ($I_{w,xx}$, $I_{w,yy}$, $I_{w,xy}$, $I_{w,zz}$)
${}_{b}I_{b}$	moment of inertia of body ($I_{b,xx}$, $I_{b,yy}$, $I_{b,zz}$)
R	wing length
L	body length
${}_{b}R_{h}$	location of wing base
${}_{w}R_{wg}$	location of center of mass of the wing
c_m	mean chord length
f	flapping frequency
T	stroke period
U_{ref}	reference velocity
β	actuation coefficient
k_p	proportional gain
k_d	derivative gain

Chapter 1

1 Introduction

1.1 Insect Flights

Flying insects, the smallest natural fliers, are masters of agile and robust flights in various complex environments by continuously varying their wing kinematics and deformations, as well as body inclination and deflexion (Ennos 1989; Sane and Dickinson 2001), normally at Reynolds number below 10^4. Unlike the counterparts with larger size such as birds and bats whose wings are supported by skeletons, the flapping wings of flying insects are thin membranes supported by a system of veins (Michener 2000; Kolomenskiy, Ravi *et al.* 2019). After the first successful flight in air dating back to Carboniferous, the flying insects have evolved extraordinary to locomote in air, such as executing rapid responds to external stimuli (Cheng, Deng *et al.* 2011; Muijres, Elzinga *et al.* 2014), maintaining extremely stable hovering, precisely tracking interested targets (Matthews and Sponberg 2018). The reciprocating wings with large flapping amplitude and angle of attack capable of generating sufficient aerodynamic force to suspend the insect in air are actuated and steered by muscles within the thorax (Deora, Gundiah *et al.* 2017). The insects of the orders Ephemeroptera and Odonata power their wings by the muscles directly inserted at the wing base. On the other hand, insects of other orders Diptera, Hymenoptera, Coleoptera and some Hemiptera adopt the indirect muscles to power the wings, which are antagonistically arranged in the thorax called dorso-longitudinal muscles (DLMs) and dorso-ventral muscles (DVMs). Meanwhile, a set of tiny, highly specialized synchronous muscles are directly inserted within the wing hinge to subtly tune the wing motion required for rapid maneuvers and flight stability (Lindsay, Sustar *et al.* 2017).

Controlled flight in insects requires an integrated system consisting of multimodal sensors to assess the flight condition, a central nervous system (CNS) to actuate the muscles, muscles to move the wings and wings to generate aerodynamic force. Uncovering the novel mechanisms how insects control flight needs to unpick the complexity of the sensorimotor neurobiology (motor pattern, central nervous system and sensory feedback), the musculoskeletal mechanics (muscles, skeletons and muscle physiology and anatomy) (Sadaf, Reddy *et al.* 2015), the highly unsteady three-dimensional aerodynamics (Liu and Kawachi 1998; Liu 2009) and high-degree-of-freedom fluid-structure interactions (flexible wing and body dynamics) (Sun, Wang *et al.* 2007; Chang and Wang 2014).

1.2 Flapping aerodynamics of insects

At first glance, insect flight seems improbable according to conventional standard aerodynamic theory since the flapping wings undergo large angle of attack, from which the leading edge vortex results grows in size and detach from the wing surface. The broken leading edge vortex results in a large drop in lift, and the wing is stalled. However, at lower Reynolds number, the leading edge vortex was not shed for long distance of translation, which was confirmed by the experimentally measured forces on model fruit fly wings (Dickinson, Lehmann *et al.* 1999) and high-fidelity CFD simulations (Liu, Ellington *et al.* 1998; Liu and Kawachi 1998; Liu 2009). Besides of the stable LEV, or delayed stall, a variety of other lift-enhancement unsteady mechanisms have been proposed till now, including clap-and-fling, added mass and wake capture (Sedov 1965; Lighthill 1973; Weis-Fogh 1973; Dickinson 1994; Sane 2003; Shyy, Aono *et al.* 2013).

Deeper understanding of the aerodynamics mechanisms of flapping flight makes it possible to establish algebraic models in the structure of the state-of-the-art quasi-steady formulas that typically include the translational terms (Dickinson, Lehmann *et al.* 1999), the added mass term (Sedov 1965) and rotational terms (Pesavento and Wang 2004; Whitney and Wood 2010; Van Veen, van Leeuwen *et al.* 2019). The translational terms include translational circulation force and translational drag. The rotational terms include the rotational circulation force and rotational drag. It is presumed that the aerodynamic force of a flapping wing at any time point is fully determined, under the quasi-steady assumption, by the instantaneous motion of the wing. It is important to note that, unlike translating airfoils, a flapping wing rotates around the wing hinge, so the incoming flow velocity in the reference frame of the wing is nonuniform. Hence, the blade element method (Osborne 1951; Glauert 1983) is commonly adopted. The wing is divided into a series of small elements in the spanwise direction, and each element is treated as a pitching and heaving airfoil. Then, the aerodynamic forces and torques are calculated for each blade element using a two-dimensional quasi-steady model. Finally, the elementary forces and torques are summed up to obtain the total aerodynamic forces and torques on the entire flapping wing.

1.3 Passive and active perspectives in flapping flights

Flight systems of insects are an integration of active muscle-driven rotational wing dynamics and passive reactions of various flexible structures including wings, exoskeletal elements, wing hinges, and musculoskeletal elements (Walker, Schwyn *et al.* 2014; Liu, Ravi *et al.* 2016; Liu 2020). Wing hinges in insects' flapping wings are considered capable of inducing passive feathering motion due to interaction between the aerodynamic, inertial and elastic restoring forces (Beatus and Cohen 2015; Kolomenskiy, Ravi *et al.* 2019). The insects can perform slight active actuation to asymmetrically change the spring rest feathering angles to generate turn maneuvers (Bergou, Ristroph *et al.* 2010). Yet, we still know less about how these flexible wing hinges work interactively and complementarily with active-actuation mechanisms to achieve a systematically efficient flapping performance and flight stabilization.

Besides of the passive responds of the flexible wing hinges to the active actuations, insects also undergo passive aerodynamic damppings. Hedrick *et al* (Hedrick, Cheng *et al.* 2009) compared two hypotheses: a passive model with the turning torque proportional to rotation rate and an active model with constant turning torque and found that the exponential decay observed by experimental measurements is well consistent with the prediction of passive model, suggesting that the flight stabilization is largely mediated by the passive damping. However, Beatus et al (Beatus, Guckenheimer *et al.* 2015) found that the recovery roll manoeuvre of fruit flies *Drosophila melanogaster* with passive damping solely is much slower than the experimental data, indicating the necessity of active feedback control through wing mediation. Elzinga et al (Elzinga, Dickson *et al.* 2012) pointed out that the exponential decay could also be induced by proportional active feedback, a similar role of passive damping by introducing a feedback proportional to the rotation rate. How the active control compensates the passive aerodynamic damping to achieve fast flight stabilization still remains unknown.

Unveiling the passive and active mechanisms in concert with the inner flexible structures and outer aerodynamic dampings integrated with the active actuated and steered flight systems may offer a novel solution to the tradeoff in biological flights and, thereby, further bring breakthroughs to the biomimetic systematic design and miniaturization for insect-scale autonomous flapping-wing micro air vehicles (FMAVs) with capabilities to achieve controlled and efficient flight autonomy.

1.4 Objective and approach

In this study, to tackle a central problem of the novel active and passive mechanisms associated with insect flight, we first established an integrated simulation-based framework, which consists of a fully nonlinear dynamic model, capable of modeling flapping-wing dynamics and aerodynamics in free or trimmed flights with flexible wing hinges, and a computational fluid dynamics (CFD) data-driven aerodynamic model (CDAM), which is proposed for fast and precise prediction of flapping unsteady aerodynamics in various flight velocities and wing kinematics, serving as an alternative to expensive CFD simulations. The CDAM is validated through comparison with the numerical simulated results of the bumblebee and hawkmoth in terms of cycle-averaged and time-resolved aerodynamic forces, torques and power assumptions.

With this simulator, we first investigate whether the active-actuation elastic-storage mechanism enables the robust flapping wing dynamics through fluid-structure interaction coupling the unsteady aerodynamics and torsional-spring-based wing-hinge dynamics to determine the passive and active mechanism of bumblebee hovering. We then established a control-theoretic analysis framework based on a proportional-derivative (PD) control strategy in terms of Laplace transformation and root locus method to determine how insects achieve fast flight stabilization through passive aerodynamic damping and neural feedback delay. We further build up a bioinspired PD controller with the control parameters optimized for fast stabilization suitable for longitudinal and 6 DoF flight control even under large perturbations.

References

Beatus, T., Cohen, I., Wing-Pitch Modulation in Maneuvering Fruit Flies Is Explained by an Interplay between Aerodynamics and a Torsional Spring, Physical Review E, Vol. 92, No. 2 (2015),pp. 022712.

Beatus, T., Guckenheimer, J. M., Cohen, I., Controlling Roll Perturbations in Fruit Flies, Journal of the Royal Society Interface, Vol. 12, No. 105 (2015),pp. 20150075.

Bergou, A. J., Ristroph, L., Guckenheimer, J., Cohen, I., Wang, Z. J., Fruit Flies Modulate Passive Wing Pitching to Generate in-Flight Turns, Physical Review Letters, Vol. 104, No. 14 (2010),pp. 148101.

Chang, S., Wang, Z. J., Predicting Fruit Fly's Sensing Rate with Insect Flight Simulations, Proceedings of the National Academy of Sciences, Vol. 111, No. 31 (2014),pp. 11246.

Cheng, B., Deng, X., Hedrick, T. L., The Mechanics and Control of Pitching Manoeuvres in a Freely Flying Hawkmoth (*Manduca Sexta*), Journal of Experimental Biology, Vol. 214, No. 24 (2011),pp. 4092.

Deora, T., Gundiah, N., Sane, S. P., Mechanics of the Thorax in Flies, Journal of Experimental Biology, Vol. 220, No. 8 (2017),pp. 1382.

Dickinson, M., The Effects of Wing Rotation on Unsteady Aerodynamic Performance at Low Reynolds Numbers, The Journal of Experimental Biology, Vol. 192, No. 1 (1994),pp. 179.

Dickinson, M. H., Lehmann, F.-O., Sane, S. P., Wing Rotation and the Aerodynamic Basis of Insect Flight, Science, Vol. 284, No. 5422 (1999),pp. 1954.

Elzinga, M. J., Dickson, W. B., Dickinson, M. H., The Influence of Sensory Delay on the Yaw Dynamics of a Flapping Insect, Journal of the Royal Society Interface, Vol. 9, No. 72 (2012),pp. 1685-1696.

Ennos, A. R., The Kinematics and Aerodynamics of the Free Flight of Some Diptera, Journal of Experimental Biology, Vol. 142, No. 1 (1989),pp. 49-85.

Glauert, H., The Elements of Aerofoil and Airscrew Theory, Cambridge University Press (1983)

Hedrick, T. L., Cheng, B., Deng, X., Wingbeat Time and the Scaling of Passive Rotational Damping in Flapping Flight, Science, Vol. 324, No. 5924 (2009),pp. 252.

Kolomenskiy, D., Ravi, S., Xu, R., Ueyama, K., Jakobi, T., Engels, T., Nakata, T., Sesterhenn, J., Schneider, K., Onishi, R., Liu, H., The Dynamics of Passive Feathering Rotation in Hovering Flight of Bumblebees, Journal of Fluids and Structures, Vol. 91, No. (2019),pp. 102628.

Lighthill, M. J., On the Weis-Fogh Mechanism of Lift Generation, Journal of Fluid Mechanics, Vol. 60, No. 1 (1973),pp. 1-17.

Lindsay, T., Sustar, A., Dickinson, M., The Function and Organization of the Motor System Controlling Flight Maneuvers in Flies, Current Biology, Vol. 27, No. 3 (2017),pp. 345-358.

Liu, H., Integrated Modeling of Insect Flight: From Morphology, Kinematics to Aerodynamics, Journal of Computational Physics, Vol. 228, No. 2 (2009),pp. 439-459.

Liu, H., Simulation-Based Insect-Inspired Flight Systems, Current Opinion in Insect Science, Vol. 42, No. (2020),pp. 105-109.

Liu, H., Ellington, C. P., Kawachi, K., van den Berg, C., Willmott, A. P., A Computational Fluid Dynamic Study of Hawkmoth Hovering, The Journal of Experimental Biology, Vol. 201, No. 4 (1998),pp. 461.

Liu, H., Kawachi, K., A Numerical Study of Insect Flight, Journal of Computational Physics, Vol. 146, No. 1 (1998),pp. 124-156.

Liu, H., Ravi, S., Kolomenskiy, D., Tanaka, H., Biomechanics and Biomimetics in Insect-Inspired Flight Systems, Philosophical Transactions of the Royal Society B: Biological Sciences, Vol. 371, No. 1704 (2016),pp. 20150390.

Matthews, M., Sponberg, S., Hawkmoth Flight in the Unsteady Wakes of Flowers, The Journal of Experimental Biology, Vol. 221, No. 22 (2018),pp. jeb179259.

Michener, C. D., The Bees of the World, JHU press (2000)

Muijres, F. T., Elzinga, M. J., Melis, J. M., Dickinson, M. H., Flies Evade Looming Targets by Executing Rapid Visually Directed Banked Turns, Science, Vol. 344, No. 6180 (2014),pp. 172.

Osborne, M., Aerodynamics of Flapping Flight with Application to Insects, Journal of Experimental Biology, Vol. 28, No. 2 (1951),pp. 221-245.

Pesavento, U., Wang, Z. J., Falling Paper: Navier-Stokes Solutions, Model of Fluid Forces, and Center of Mass Elevation, Physical Review Letters, Vol. 93, No. 14 (2004),pp. 144501.

Sadaf, S., Reddy, O. V., Sane, S. P., Hasan, G., Neural Control of Wing Coordination in Flies, Current Biology, Vol. 25, No. 1 (2015),pp. 80-86.

Sane, S. P., The Aerodynamics of Insect Flight, Journal of Experimental Biology, Vol. 206, No. 23 (2003),pp. 4191.

Sane, S. P., Dickinson, M. H., The Control of Flight Force by a Flapping Wing: Lift and Drag Production, Journal of Experimental Biology, Vol. 204, No. 15 (2001),pp. 2607.

Sedov, L. I., Two-Dimensional Problems in Hydrodynamics and Aerodynamics, Interscience Publishers (1965)

Shyy, W., Aono, H., Kang, C.-k., Liu, H., An Introduction to Flapping Wing Aerodynamics, Cambridge, Cambridge University Press (2013)

Sun, M., Wang, J., Xiong, Y., Dynamic Flight Stability of Hovering Insects, Acta Mechanica Sinica, Vol. 23, No. 3 (2007),pp. 231-246.

Van Veen, W. G., van Leeuwen, J. L., Muijres, F. T., A Chordwise Offset of the Wing-Pitch Axis Enhances Rotational Aerodynamic Forces on Insect Wings: A Numerical Study, Journal of the Royal Society Interface, Vol. 16, No. 155 (2019),pp. 20190118.

Walker, S. M., Schwyn, D. A., Mokso, R., Wicklein, M., Müller, T., Doube, M., Stampanoni, M., Krapp, H. G., Taylor, G. K., In Vivo Time-Resolved Microtomography Reveals the Mechanics of the Blowfly Flight Motor, PLoS Biology, Vol. 12, No. 3 (2014),pp. e1001823.

Weis-Fogh, T., Quick Estimates of Flight Fitness in Hovering Animals, Including Novel Mechanisms for Lift Production, Journal of Experimental Biology, Vol. 59, No. 1 (1973),pp. 169.

Whitney, J. P., Wood, R. J., Aeromechanics of Passive Rotation in Flapping Flight, Journal of Fluid Mechanics, Vol. 660, No. (2010),pp. 197.

Chapter 2

2 Simulation-based framework of flapping flight

2.1 Introduction

Accurate evaluation of aerodynamic loads that act on a flying insect is a key issue in the analysis of its flight behavior (Liu, Ravi *et al.* 2016). High-fidelity numerical simulations by solving the Navier–Stokes equations (Liu, Ellington *et al.* 1998; Liu and Kawachi 1998; Liu 2009; Engels, Kolomenskiy *et al.* 2016; Nguyen, Sundar *et al.* 2016; Cheng and Sun 2018; Ishihara 2018; Zhang, Hedrick *et al.* 2019; Oh, Lee *et al.* 2020) have been implemented to reveal the flow structures, time-dependent aerodynamic forces, torques and power consumption for the past few decades. However, such simulations are always source- and time consuming and unable to supply promptly instantaneously aerodynamical information such as aerodynamic forces and torques, which become less helpful when a large number of different designs are compared, as in the geometric optimization, or when the long-time evolution of the aerodynamic forces is required for problems such as flight control (Deng, Schenato *et al.* 2006; Ma, Chirarattananon *et al.* 2013; Fei, Tu *et al.* 2019). Mathematical modelling is then taken as an alternative to numerical simulations. Deeper understanding of the aerodynamics mechanisms of flapping flight is reflected in the structure of the state-of-the-art quasi-steady formulas that typically include the translational terms (Dickinson, Lehmann *et al.* 1999), the added mass term (Sedov 1965) and rotational terms (Pesavento and Wang 2004; Whitney and Wood 2010; Van Veen, van Leeuwen *et al.* 2019). The diversity of flapping flight systems that exist in nature and appear in biomimetic mechanical devices is so vast that it hardly can be encompassed in one universal quasi-steady model. Instead, the existing models often specialize in a certain flight regime, e.g., hovering (Nabawy and Crowther 2014), focus on selected species, e.g., locust (Jensen 1956), beetle (Oh, Lee *et al.* 2020) and predict a number of selected quantities of interest, such as the mean lift and power (Nabawy and Crowther 2014), wing pitching moments (Wang, Goosen *et al.* 2016), etc. The architecture of a quasi-steady model is determined by its intended area of application.

The insect flight is achieved through actuating the wings back and forth in a manner of fluid-structure interaction. The aerodynamic loads on a flying insect resulting from flapping wing and body motion determine its dynamics. For instance, the insects experience passive aerodynamic damping (also termed as flight-counter torque (Hedrick, Cheng *et al.* 2009)) while performing rotations, which help to flight stabilization. In terms of active feedback control, the flight is mediated by tuning the aerodynamic loads via adjusting wing kinematics. In addition, the wing also passively reflects to the active actuation through the flexible wing hinge and the aerodynamic loads (Bergou, Ristroph *et al.* 2010; Beatus and Cohen 2015; Kolomenskiy, Ravi *et al.* 2019).

In this chapter, we developed an integrated simulation-based framework, which consists of a fully nonlinear dynamic model and a computational fluid dynamics (CFD) data-driven aerodynamic model (CDAM), which is proposed for fast and precise prediction of flapping unsteady aerodynamics in various flight velocities and wing kinematics. The dynamic model is versatile, capable of modeling free or trimmed flapping-wing flights with rigid or flexible wing hinges. Combined with active control strategies, the dynamic model can serve as a virtual physical engine to study the autocontrol of flying insects and FWMAVs. The CDAM comprises a quasi-steady model for flapping wings and an aerodynamic model for a moving body, which is informed by high-fidelity CFD simulations using overset meshes to enable precise and fast prediction of both cycle-averaged and transient aerodynamic force, torque and power with a variety of flying motions and wing kinematics.

2.2 CFD data-driven aerodynamic model (CDAM)

In this section, a CFD data-driven aerodynamic model (CDAM) is constructed to predict the aerodynamic force, torque and power consumption of a flying bumblebee *Bombus ignitus*. It consists of two components: a CFD-informed quasi-steady model for flapping wings and a simplified aerodynamic model for a moving body. The flapping wing model can account for a variety of flying velocities and wing kinematics which is based on the blade element method. The wings are assumed to be flat and rigid. They are divided into small elements. The quasi-steady model is applied on each element to obtain the aerodynamic force, torque and power which are consequently summed up over the entire wing. Next, the simplified aerodynamic model for the moving body is established to obtain the lift and drag on the body. This methodology is also generalized to the hawkmoth *Manduca sexta* to test its limits at high Reynolds number.

2.2.1 Nomenclature and coordinate system

In the wing model, the angle of attack of each element is calculated by identifying the direction of the velocity of each element in the wing-fixed frame of reference. This includes summation of the wing rotation relative to the stroke plane and the body motion relative to the ground. Therefore, the wing velocity and the body velocity need to be transformed into the wing-fixed frame of reference. Similarly, to calculate aerodynamic forces that act on the body, the body velocity needs to be transformed into the body fixed frame of reference. For these purposes, let us introduce the coordinate transforms between different coordinate frames. As is shown in Figure 2.1, a modelled bumblebee is distinguished between the ground frame, the body-fixed frame, a right wing-fixed frame, a left wing-fixed frame and corresponding stroke plane frames. Table 2.1 summarizes the values of the morphology parameters of the bumblebee.

In this study, the flapping wing is assumed to be flat, rigid and rotating around the wing base with respect to stroke plane as shown in Figure 2.1. Therefore, the wing kinematics can be defined by the given flapping angles called positional, elevation and feathering angles. The angle θ_{SP} is the stroke plane angle with respect to the horizontal plane. The "rotation axis" in our terminology is the longitudinal axis of the wing. The positional angle φ is measured between the lateral direction and the projection of the rotation axis on the stroke plane; the elevation angle θ is the deviation angle of the rotation axis from the stroke plane; the feathering angle η is the angular displacement of the wing about the rotation axis, as plotted in Figure 2.2, which are expressed in Fourier series if prescribed, such as

$$\varphi = \sum_{n=0}^{4} a_{\varphi,n} \cos(2\pi n f t) + b_{\varphi,n} \sin(2\pi n f t) \tag{2.1}$$

$$\theta = \sum_{n=0}^{4} a_{\theta,n} \cos(2\pi n f t) + b_{\theta,n} \sin(2\pi n f t) \tag{2.2}$$

$$\eta = \sum_{n=0}^{4} a_{\eta,n} \cos(2\pi n f t) + b_{\eta,n} \sin(2\pi n f t) \tag{2.3}$$

where t is time. The moving body is also assumed to be rigid, which can be defined as the body angles called yaw, pitch and roll angles. The yaw angle ψ measures the rotation of the body around vertical axis; the pitch angle χ is the inclination of the body between the horizontal plane; the roll angle ρ is the angular displacement of the body about its longitudinal axis. The body angle and stroke plane angle in hovering are $\frac{\pi}{4}$ and 0, respectively.

The coordinate transformation matrix $E_{g\to w}$ that converts a vector from the ground frame $({}_{g}x,\ {}_{g}y,\ {}_{g}z)$ to the wing-fixed frame $({}_{w}x,\ {}_{w}y,\ {}_{w}z)$ can be expressed as

$$E_{g\to w} = E_{\theta\to w}E_{\varphi\to\theta}E_{sp\to\varphi}E_{g\to sp} \tag{2.4}$$

where

$$E_{g\to sp} = \begin{pmatrix} \sin\theta_{SP} & 0 & -\cos\theta_{SP} \\ 0 & 1 & 0 \\ \cos\theta_{SP} & 0 & \sin\theta_{SP} \end{pmatrix} \tag{2.5}$$

$$E_{sp\to\varphi} = \begin{pmatrix} 1 & 0 & 0 \\ 0 & \cos\varphi & \sin\varphi \\ 0 & -\sin\varphi & \cos\varphi \end{pmatrix} \tag{2.6}$$

$$E_{\varphi\to\theta} = \begin{pmatrix} \cos\theta & \sin\theta & 0 \\ -\sin\theta & \cos\theta & 0 \\ 0 & 0 & 1 \end{pmatrix} \tag{2.7}$$

$$E_{\theta\to w} = \begin{pmatrix} \cos\eta & 0 & -\sin\eta \\ 0 & 1 & 0 \\ \sin\eta & 0 & \cos\eta \end{pmatrix} \tag{2.8}$$

$E_{g\to sp}$ is the coordinate transformation matrix that converts a vector from the ground frame $({}_{g}x,\ {}_{g}y,\ {}_{g}z)$ to the stroke plane frame $({}_{sp}x, {}_{sp}y, {}_{sp}z)$ which is coinciding with the wing-fixed frame when φ, θ and η are 0. Similarly, the coordinate transformation matrix $E_{g\to b}$ that converts a vector from the ground frame $({}_{g}x,\ {}_{g}y,\ {}_{g}z)$ to the body-fixed frame $({}_{b}x,\ {}_{b}y,\ {}_{b}z)$ can be expresses as

$$E_{g\to b} = \begin{pmatrix} \sin\chi & 0 & -\cos\chi \\ 0 & 1 & 0 \\ \cos\chi & 0 & \sin\chi \end{pmatrix} \tag{2.9}$$

The angular velocity of the wing in the stroke plane frame is

$${}_{sp}\boldsymbol{\omega} = \begin{pmatrix} \dot{\varphi} \\ 0 \\ 0 \end{pmatrix} + E'_{\varphi\to\theta}\begin{pmatrix} 0 \\ 0 \\ \dot{\theta} \end{pmatrix} + E'_{\varphi\to\theta}E'_{\theta\to w}\begin{pmatrix} 0 \\ \dot{\eta} \\ 0 \end{pmatrix} \tag{2.10}$$

The representative velocity of each blade element is defined by the velocity and sampled along the rotation axis, i.e. at points with coordinates $(0, r, 0)'$ in the wing-fixed frame, as illustrated in Figure 2.1, which can be presented in stroke plane frame, such as

$${}_{sp}\boldsymbol{v}_{w}(r) = {}_{sp}\boldsymbol{\omega} \times \left[E'_{sp\to w}\begin{pmatrix} 0 \\ r \\ 0 \end{pmatrix}\right] + {}_{sp}\boldsymbol{v}_{b} \tag{2.11}$$

2.2.2 Quasi-steady model for flapping wing

The quasi-steady model proposed in this study should give high precision for a range of velocity of the insect (forward/backward velocity, lateral velocity and vertical velocity), that is, this model should be applicable to the three-dimensional velocity space, which we define to be a cuboid ranging from $-0.4U_{ref}$ to $0.4U_{ref}$ in forward/backward direction, $-0.4U_{ref}$ to $0.4U_{ref}$ in lateral direction, 0 to $0.4U_{ref}$ in vertical direction. The forward velocity can affect the lift and drag coefficients (Dickson and Dickinson 2004). The coefficients parameterizing the quasi-steady model in this paper also vary with the velocity of the modeled bumblebee. Thus, we construct a CFD database covering a variety of flying velocities and wing kinematics which are discrete points in the three-dimensional velocity space. The wing kinematics of hovering flight are used as baseline in the study, see Figure 2.2. Then the coefficients are fitted for all the discrete points separately. Finally, interpolation method is adopted to calculate the coefficients for any point in the three-dimensional velocity space.

In this study, the instantaneous aerodynamic force F_{aero} generated by the flapping wing can be decomposed into five quasi-steady forces based on the blade element method: translational circulation force F_{tc}, rotational circulation force F_{rc}, translational drag F_{td}, rotational drag F_{rd} and force due to added mass F_{am}. CFD simulation of flapping-wing insect has shown that the aerodynamic force applied on the flapping wing is mainly normal to the wing surface (Nakata, Liu *et al.* 2015) when the Reynolds number is of the order of several hundreds or thousands because the aerodynamic force in those wings is dominated by the pressure. Therefore, the aerodynamic force is assumed to be normal to the wing surface (Sane and Dickinson 2002; Wang, Goosen *et al.* 2016; Bluman and Kang 2017) in this study, of which only the normal component of the instantaneous aerodynamic force is calculated as a sum of terms,

$$F_{aero,N} = F_{tc,N} + F_{rc,N} + F_{td,N} + F_{rd,N} + F_{am,N} \qquad (2.12)$$

Previous work on quasi-steady models mainly focused on hovering flight (Sane and Dickinson 2002; Whitney and Wood 2010; Nakata, Liu *et al.* 2015; Lee, Lua *et al.* 2016), in which the velocity of each wing blade had zero spanwise component. In our study, the absolute velocity of each wing element includes a non-zero spanwise component due to the body velocity $\boldsymbol{v}_b$. According to (Dudley and Ellington 1990), the spanwise component of the velocity does not contribute to the aerodynamic force production. Therefore, only the velocity component normal to the rotation axis is taken into account in the blade element method. Based on the blade element method and zero spanwise velocity assumption, the total quasi-steady aerodynamic force on a wing element is decomposed in five contributions, as shown in Figure 2.3, and the following expressions are used to evaluate these terms

$$F_{tc,N} = \int_0^R -\rho_{aero} c(r) C_T \cos^2 \alpha \left|{}_w v_{wn}\right| {}_w v_{wn,z} dr \qquad (2.13)$$

$$F_{rc,N} = \int_0^R -\frac{1}{2}\rho_{aero} C_R \dot{\eta} c^2(r)\, {}_w v_{wn,x} dr \tag{2.14}$$

$$F_{td,N} = \int_0^R -\frac{1}{2}\rho_{aero} c(r) C_D \sin^2\alpha \left|{}_w v_{wn}\right| {}_w v_{wn,z} dr \tag{2.15}$$

$$F_{rd,N} = \int_0^R -\frac{1}{6}\rho_{aero} C_{rd} |\dot{\eta}| \dot{\eta} \left(f_l^3(r) + f_t^3(r)\right) dr \tag{2.16}$$

$$F_{am,N} = \int_0^R -A_1 \frac{\pi\rho_{aero}}{4} c^2(r)\, {}_w a_{w,z} dr + \int_0^R -A_2 \frac{\pi\rho_{aero}}{8} \left(f_l(r) + f_t(r)\right) c^2(r)\, {}_w \omega_{w,y} dr \tag{2.17}$$

where $c(r)$ is the local chordwise length, f_l and f_t are the curves of leading edge and trailing edge of the wing, ${}_w v_{wn}$ is the velocity component normal to the rotation axis of wing element, $\left|{}_w v_{wn}\right|$ represents its magnitude, C_T is the translational circulation coefficient, C_R is the rotational circulation drag coefficient, C_D is the translational drag coefficient, C_{rd} is the rotational drag coefficient, A_1 and A_2 are the added mass coefficients, α is the angle of attack ranging from 0 to π,

$$\alpha = \cos^{-1}\left(-\frac{{}_w v_{wn,x}}{\left|{}_w v_{wn}\right|}\right) \tag{2.18}$$

Equations (2.13)~(2.17) can be written in summation

$$F_{aero,N} = \sum_{i=1}^{6} I_i F_i \tag{2.19}$$

where

$$I = [C_T, C_R, C_D, C_{rd}, A_1, A_2] \tag{2.20}$$

$$F = \begin{pmatrix} \int_0^R -\rho_{aero} c(r) \cos^2\alpha \left|{}_w v_{wn}\right| {}_w v_{wn,z} dr \\ \int_0^R -\frac{1}{2}\rho_{aero} \dot{\eta} c^2(r)\, {}_w v_{wn,x} dr \\ \int_0^R -\frac{1}{2}\rho_{aero} c(r) \sin^2\alpha \left|{}_w v_{wn}\right| {}_w v_{wn,z} dr \\ \int_0^R -\frac{1}{6}\rho_{aero} |\dot{\eta}| \dot{\eta} \left(f_l^3(r) + f_t^3(r)\right) dr \\ \int_0^R -\frac{\pi\rho_{aero}}{4} c^2(r)\, {}_w a_{w,z} dr \\ \int_0^R -\frac{\pi\rho_{aero}}{8} \left(f_l(r) + f_t(r)\right) c^2(r)\, {}_w \omega_{w,y} dr \end{pmatrix} \tag{2.21}$$

To close the quasi-steady model for aerodynamic force, coefficients (2.20) must be determined theoretically (Sedov 1965; Fung 2008), experimentally (Dickinson, Lehmann *et al.* 1999; Sane and Dickinson 2002; Andersen, Pesavento *et al.* 2005; Whitney and Wood 2010) or computationally (Pesavento and Wang 2004; Nakata, Liu *et al.* 2015; Bluman and Kang 2017). Nakata et al (Nakata, Liu *et al.* 2015) identified these coefficients for hovering flight by fitting the instantaneous aerodynamic forces from a computational high-fidelity model (Liu, Ellington *et al.* 1998; Liu and Kawachi 1998; Liu 2009) using the least square method. A similar approach is adopted in this study. It is pointed out by Nakata et al (Nakata, Liu *et al.* 2015) that increasing the size of input CFD database with different wing kinematics can improve the accuracy of the quasi-steady model.

It is noted that the aerodynamic moment around the rotation axis is below 2 mNmm except for stroke reversal (below 5 mNmm), the cycle-averaged chordwise location of aerodynamic force is fitted from the CFD simulation which is found to be only about $0.03c_m$ away from the “rotation axis”, so the chordwise location of aerodynamic force is assumed to be zero. Hence, the aerodynamic torque with respect to the center of mass of the modeled bumblebee in the body-fixed frame can be expressed as

$${}_b\boldsymbol{T}_{aero} = \int_0^R \left[{}_bR_h + E_{w\to b}\begin{pmatrix}0\\ r\\ 0\end{pmatrix}\right] \times \left[E_{w\to b}\begin{pmatrix}0\\ 0\\ F_{aero,N}(r)\end{pmatrix}\right]\mathrm{d}r \tag{2.22}$$

The aerodynamic power required to move the wings through the air is

$$P_{aero} = \int_0^R \begin{pmatrix}0\\ 0\\ F_{aero,N}(r)\end{pmatrix} \cdot {}_wv_w \mathrm{d}r \tag{2.23}$$

2.2.3 Simplified aerodynamic model for moving body

The contribution of moving body to the total aerodynamic force and torque cannot be neglected. The aerodynamics of a moving insect body on its own is simpler than the unsteady aerodynamics of flapping wings. However, the interaction between the body and the wings alters the total aerodynamic performance of the body (Yu and Sun 2009; Liu, Dong *et al.* 2016). The aerodynamic force of the body fluctuates due to the reciprocating motion of the wings, and it is difficult to describe this effect by means of pure theoretical analysis. In this study, we construct a simplified aerodynamic model based on the quasi-steady approximation with coefficients fitted to the CFD data. The model consists in the dynamical similarity formulas for the lift

$$F_{bd,L} = \rho_{aero}R^2 C_{bd,L}\sin 2\lambda\, |u|^2 \left(\hat{u} \times \left(\hat{u} \times {}_b\hat{x}\right)\right) \tag{2.24}$$

$$F_{bd,D} = -\rho_{aero}R^2 \left[C_{bd,D}(0)\cos^2\lambda + C_{bd,D}\left(\frac{\pi}{2}\right)\sin^2\lambda\right]|u|^2\hat{u} \tag{2.25}$$

where $\hat{u}$ is the unit vector in the direction of the body velocity, $C_{bd,L}$ is the lift coefficient,

$C_{bd,D}(0)$ and $C_{bd,D}\left(\frac{\pi}{2}\right)$ are the drag coefficients that correspond to the angle of attack of the body equal to 0 and $\frac{\pi}{2}$, respectively. The body angle of attack λ varies between 0 and π, and it is calculated as

$$\lambda = \cos^{-1}\left(-\frac{{}_{b}u_x}{|{}_{b}u|}\right) \tag{2.26}$$

The direction of the lift $F_{bd,L}$ is defined by $\hat{u} \times (\hat{u} \times {}_{b}\hat{x})$ which is normal to the direction of the velocity u. $F_{bd,L}$, u and ${}_{b}\hat{x}$ lie in the same plane. ${}_{b}\hat{x}$ is the unit vector along the *x*-direction in the body-fixed frame. Because the aerodynamic models for the flapping wings and the moving body are independent, $C_{bd,L}$, $C_{bd,D}(0)$ and $C_{bd,D}\left(\frac{\pi}{2}\right)$ are independent of wing kinematics and, in addition, are assumed to be independent of the flying velocity. Because the body has bilateral symmetry, the center of the aerodynamic force is assumed to locate on the plane of symmetry which can be expressed in the body frame as $(x_p, 0, z_p)'$. The locations x_p and z_p are also treated as coefficients needed to be fitted from CFD database. The aerodynamic torque in the body frame is

$${}_{b}\boldsymbol{T}_{aero} = \begin{pmatrix} x_p \\ 0 \\ z_p \end{pmatrix} \times (F_{bd,L} + F_{bd,D}) \tag{2.27}$$

2.2.4 A CFD simulator for insect flight

The flow field around a flying insect is simulated by solving the three-dimensional, incompressible, unsteady Navier-Stokes equations numerically written in strong conservation form for mass and momentum. The artificial compressibility method is used by adding a pseudo time derivative of pressure to the equation of continuity. For an arbitrary deformable control volume V(t), the non-dimensionalized governing equations are:

$$\int_{V(t)} \left(\frac{\partial \boldsymbol{Q}}{\partial t} + \frac{\partial \boldsymbol{q}}{\partial \tau}\right) dV + \int_{V(t)} \left(\frac{\partial \boldsymbol{F}}{\partial x} + \frac{\partial \boldsymbol{G}}{\partial y} + \frac{\partial \boldsymbol{H}}{\partial z} + \frac{\partial \boldsymbol{F}_v}{\partial x} + \frac{\partial \boldsymbol{G}_v}{\partial y} + \frac{\partial \boldsymbol{H}_v}{\partial z}\right) dV = 0 \tag{2.28}$$

where

$$\boldsymbol{Q} = \begin{pmatrix} u \\ v \\ w \\ 0 \end{pmatrix}, \boldsymbol{q} = \begin{pmatrix} u \\ v \\ w \\ p \end{pmatrix}, \boldsymbol{F} = \begin{pmatrix} u^2 + p \\ uv \\ uw \\ \lambda u \end{pmatrix}, \boldsymbol{G} = \begin{pmatrix} vu \\ v^2 + p \\ vw \\ \lambda v \end{pmatrix}, \boldsymbol{H} = \begin{pmatrix} wu \\ wv \\ w^2 + p \\ \lambda w \end{pmatrix},$$

$$\boldsymbol{F}_v = -\frac{1}{Re}\begin{pmatrix} 2u_x \\ u_y + v_x \\ u_z + w_x \\ 0 \end{pmatrix}, \boldsymbol{G}_v = -\frac{1}{Re}\begin{pmatrix} v_x + u_y \\ 2v_y \\ v_z + w_y \\ 0 \end{pmatrix}, \boldsymbol{H}_v = -\frac{1}{Re}\begin{pmatrix} w_x + u_z \\ w_y + v_z \\ 2w_z \\ 0 \end{pmatrix}$$

In the preceding equations, λ is the pseudo-compressibility coefficient, p the pressure, u, v and w are velocity components in the global Cartesian coordinate system, t the physical time while τ the pseudo time, and Re the Reynolds number. The term $\boldsymbol{q}$ associated with the pseudo time is designed for an inner-iteration at each physical time step, and will vanish when the divergence of velocity is driven to zero so as to satisfy the equation of continuity. By introducing the generalized Reynolds transport theorem and by employing the Gauss integration theorem, an integrated form of equation (2.28) in general curvilinear coordinate system is gained as

$$\int_{V(t)} \frac{\partial \boldsymbol{q}}{\partial \tau} dV + \frac{\partial}{\partial t}\int_{V(t)} \boldsymbol{Q} dV + \oint_{S(t)} \left(\boldsymbol{f} - \boldsymbol{Q}\boldsymbol{u}_g\right) \cdot \boldsymbol{n} dS = 0 \qquad (2.29)$$

Where $\boldsymbol{f} = (\boldsymbol{F} + \boldsymbol{F}_v, \boldsymbol{G} + \boldsymbol{G}_v, \boldsymbol{H} + \boldsymbol{H}_v)$, $S(t)$ the surface of the control volume, $\boldsymbol{n} = \left(n_x, n_y, n_z\right)$ the components of the unit outward normal vector corresponding to all the faces of the polyhedron cell, $\boldsymbol{u}_g$ the local velocity of the moving cell surface. For a structured, boundary-fitted, and cell-centered storage architecture, we can further reform equation (2.29) in terms of the semi-discrete form, where (i, j, k) denote the cell index, such that

$$\frac{\partial}{\partial t}[V\boldsymbol{Q}]_{ijk} + \boldsymbol{R}_{ijk} + V_{ijk}\left(\frac{\partial \boldsymbol{q}}{\partial \tau}\right)_{ijk} = 0 \qquad (2.30)$$

where

$$\boldsymbol{R}_{ijk} = \left(\widehat{\boldsymbol{F}} + \widehat{\boldsymbol{F}}_v\right)_{i+\frac{1}{2},j,k} - \left(\widehat{\boldsymbol{F}} + \widehat{\boldsymbol{F}}_v\right)_{i-\frac{1}{2},j,k} + \left(\widehat{\boldsymbol{G}} + \widehat{\boldsymbol{G}}_v\right)_{i,j+\frac{1}{2},k} - \left(\widehat{\boldsymbol{G}} + \widehat{\boldsymbol{G}}_v\right)_{i,j-\frac{1}{2},k} + \left(\widehat{\boldsymbol{H}} + \widehat{\boldsymbol{H}}_v\right)_{i,j,k+\frac{1}{2}} - \left(\widehat{\boldsymbol{H}} + \widehat{\boldsymbol{H}}_v\right)_{i,j,k-\frac{1}{2}}$$

e.g. $\widehat{\boldsymbol{F}} + \widehat{\boldsymbol{F}}_v = \left(\boldsymbol{f} - \boldsymbol{Q}\boldsymbol{u}_g\right) \cdot \boldsymbol{S}_n^{\xi}$, $\boldsymbol{S}_n^{\xi} = \left[S_{nx}^{\xi}, S_{ny}^{\xi}, S_{nz}^{\xi}\right]$, $\boldsymbol{n} = \frac{\boldsymbol{S}_n^{\xi}}{S}$,

$$S = \sqrt{{S_{nx}^{\xi}}^2 + {S_{ny}^{\xi}}^2 + {S_{nz}^{\xi}}^2}$$

The term V_{ijk} is the volume of the cell (i, j, k). Note that the unit outward normal vector $\boldsymbol{n}$ can be calculated using the areas of the cell faces, e.g. $\boldsymbol{S}_n^{\xi}$ in ξ-direction. A detailed description of evaluation of the inviscid flux and the viscous flux can be found in (Liu and Kawachi 1998; Liu 2005; Liu 2009).

The fortified approach is used to solve the subset equations by adding forcing terms to the Navier-Stokes algorithm in the appropriate flow regions (Fujii 1995), for the semi-discrete form, such as

$$\frac{\partial}{\partial t}[V\boldsymbol{Q}]_{ijk} + \boldsymbol{R}_{ijk} + V_{ijk}\left(\frac{\partial \boldsymbol{q}}{\partial \tau}\right)_{ijk} = \sigma(\boldsymbol{q}_f - \boldsymbol{q}) \qquad (2.31)$$

Where the switching parameter σ is set to be sufficiently large, compared to the all the terms in the region, where the solution $\boldsymbol{q}_f$ is available by the subset equations, and zero outside the region. In a wider sense, this method provides a potential payoff to an improvement of both the efficiency and accuracy of any governing equations but not limited to the NS equations. The Pade scheme is employed for the time integration

$$\frac{\partial}{\partial t} = \frac{1}{\Delta \mathrm{t}}\frac{\Delta}{1 + \vartheta\Delta} \qquad (2.32)$$

where parameter ϑ is taken to be 0.5 for the implicit Euler scheme with second-order accuracy in time, $\Delta \mathrm{t}$ the time increment, and $\Delta\boldsymbol{q} = \boldsymbol{q}^{(n+1)} - \boldsymbol{q}^{(n)}$.

The CFD simulation of the bumblebee contains four overset grids, i.e. body grid (37×39 ×19), right wing grid (37×33×11), left wing grid (37×33×11) and background grid (92×84× 68). Body grid, right wing grid, left wing grid are body-fitted grids, see Figure 2.4. To establish the communication between overlapped grids, the Newton's method is employed to determine the location of a point inside a cell using tri-linear interpolation (Liu 2009) After 3 flapping cycles, the flow is fully developed and the quantities are periodic, which is independent of the starting position.

2.3 Construction of CFD database

To inform the CDAM, we do CFD simulations in different velocities, see Table 2.2. For each velocity, several CFD simulations are run with different wing kinematics, see Table 2.3, to obtain training data. The range of wing kinematics are created by varying wing beat frequency, as well as the positional and the feathering angles profiles. The elevation kinematics remains unchanged. Total 71 cases are used to inform the quasi-steady model for flapping wing and simplified aerodynamic model for moving body, which we denote as the training data set. To test the accuracy and generality of the quasi-steady model for flapping wings, simplified aerodynamic model for the moving body and the entire CDAM, 15 more CFD cases with randomly selected flight velocities and wing kinematics were run, forming a test data set, see Table 2.4. Each case can be finished within 20 hours on a computer with 12 cores, hence, it takes about one month to complete the database. Online supplementary material includes the body grid, the wing grid along with the wing kinematics of the bumblebee model and the results (force, torque and power) of CFD simulations.

2.4 Accuracy validation on CDAM

In this section, we fit the CDAM coefficients to the CFD training data and test the performance of the model on the CFD test data.

2.4.1 Quasi-steady model for flapping wing

In each CFD case, the modeled bumblebee begins to flap in quiescent air and the near flow field becomes quasi-periodic after three wing beats. Therefore, for each CFD case, we select 1000 uniformly distributed points in time over the fourth cycle to fit the model coefficients of quasi-steady model. For example, for a specified velocity $\boldsymbol{u}_{eg}$, a total of n CFD cases with different wing kinematics are run. Then, total of $1000n$ data samples of the CFD forces are selected and $1000n$ instantaneous forces of quasi-steady model are evaluated. The least square error of the force evaluated by the quasi-steady model relative to the CFD reference data is calculated as

$$\begin{aligned}\varepsilon_{ls}(\boldsymbol{u}_{eg}) &= \sum_{i=1}^{n}\sum_{k=1}^{1000}\left[F_{QSM,N}^{i}(t_k) - F_{CFD,N}^{i}(t_k)\right]^2 \\ &= \sum_{i=1}^{n}\sum_{k=1}^{1000}\left[\sum_{j=1}^{6} I_j(\boldsymbol{u}_{eg})F_j^i(t_k) - F_{CFD,N}^{i}(t_k)\right]^2 \end{aligned} \qquad (2.33)$$

where $F_{QSM,N}^{i}(t_k)$ is the aerodynamic force normal to the wing surface calculated by equations (2.13)~(2.17), $F_{CFD,N}^{i}(t_k)$ is the aerodynamic force normal to wing surface from the CFD simulation. Then the coefficients parameterizing the quasi-steady model for this velocity $\boldsymbol{u}_{eg}$ can be obtained by minimizing $\varepsilon_{ls}(\boldsymbol{u}_{eg})$, so called least square method

$$\begin{aligned} I_j(\boldsymbol{u}_{eg}) &= \left[\sum_{i=1}^{n}\sum_{k=1}^{1000}\begin{pmatrix} F_1^i(k)F_1^i(k) & \cdots & F_6^i(k)F_1^i(k) \\ \vdots & \ddots & \vdots \\ F_1^i(k)F_6^i(k) & \ldots & F_6^i(k)F_6^i(k)\end{pmatrix}\right]^{-1} \\ &\quad \cdot \left[\sum_{i=1}^{n}\sum_{k=1}^{1000}\begin{pmatrix} F_{CFD,N}^{i}(k)F_1^i(k) \\ \vdots \\ F_{CFD,N}^{i}(k)F_6^i(k)\end{pmatrix}\right] \end{aligned} \qquad (2.34)$$

As can be seen from Table 2.2, 12 different velocities are selected, so 12 sets of $[C_T, C_R, C_D, C_{rd}, A_1, A_2]$ are fitted here. Then, an interpolation method is adopted to predict the coefficients for arbitrary velocity of the insect. We adopt Kriging surrogate model as the interpolation method which is available as a MATLAB toolbox DACE (Lophaven, Nielsen *et al.* 2002). The procedure is graphically illustrated in Figure 2.5. 12 distinct velocities as shown in Table 2.2 and the corresponding 12 sets of fitted coefficients $[C_T, C_R, C_D, C_{rd}, A_1, A_2]$ are the inputs and outputs, respectively, to inform the Kriging surrogate model.

Figure 2.6 shows the comparison of cycle-averaged aerodynamic quantities between the prediction of the quasi-steady model and CFD results. It can be seen that all the dots are close to the diagonal solid line which indicates that the predictions of the quasi-steady model approach is close to the CFD results for both training data set and test data set. This validates the predictive capacity of the quasi-steady model. Thus, the quasi-steady model adequately approximates the aerodynamic mechanisms of flapping wings using a reduced parameter space.

Figure 2.7a and b show the comparison of lift and drag coefficients between the quasi-steady model and CFD results. The translational lift and drag generated by CFD simulation is obtained by subtracting the rotational circulation force, rotational drag and added mass from the force simulated by the CFD. Figure 2.7c shows the comparison of torque coefficients between the quasi-steady model and CFD results. The lift, drag and torque coefficients are defined as

$$C_L = \frac{2Lift}{\int_0^R \rho c v^2 \mathrm{d}r}, C_D = \frac{2Drag}{\int_0^R \rho c v^2 \mathrm{d}r}, C_M = \frac{2Torque}{\int_0^R \rho c r v^2 \mathrm{d}r} \tag{2.35}$$

Both lift and drag coefficients of quasi-steady model agree with CFD results well. When the angle of attack is large, the torque coefficient of the quasi-steady model is generally lower than that of CFD. This may be because of the underestimation of spanwise torque for high angle of attack. Figure 2.7d, e and f show the comparison between the quasi-steady model and CFD for three different flight velocities. The translational lift and drag are the dominant contributors to the force generation. The rotational circulation force is also an important component for force generation, which captures the coupling effect between translation motion and rotation motion. The added mass effect plays a minor role in force generation. The contribution to vertical force of rotation drag is very small, partly because the rotation velocity peaks during the stroke reversal where the rotational drag is almost horizontal. The lift and drag coefficients for hovering revolving wing by the proposed model is also compared with the experimental results (Usherwood and Ellington 2002) as shown in Figure 2.7a and (b). The lift coefficient by the proposed model is almost identical to the experimental results and the proposed model overestimates the drag coefficient for angle of attack larger than 40 degrees. This overestimation may be because the drag coefficient by the proposed model is fitted from a flapping wing rather than a revolving wing.

2.4.2 Simplified aerodynamic model for moving body

Five constant coefficients $\left[C_{bd,L}, C_{bd,D}(0), C_{bd,D}\left(\frac{\pi}{2}\right), x_p, z_p\right]$ parameterizing the simplified aerodynamic model are fitted by minimizing the least square error for the CFD training data set. The results for a bumblebee are listed in Table 2.5. Figure 2.8 shows the comparison of the cycle-averaged aerodynamic quantities between the simplified aerodynamic model and CFD results for the moving body. The simplified aerodynamic model performs consistently on both training data set and test data set.

2.4.3 Aerodynamic performance of CDAM of bumblebee

Sections 2.2, 2.4.1 and 2.4.2 discussed and validated the quasi-steady model for flapping wings and the simplified aerodynamic model for a moving body separately. Here, we combine them in one model, i.e. the CFD data-driven aerodynamic model. Figure 2.9 shows the comparison between the predictions using CDAM and the results of CFD simulation. The predictions by the CDAM are well consistent with the CFD results.

2.5 Discussion

2.5.1 Aerodynamics of forward flight condition

The quasi-steady approach only uses the instantaneous motion of the flapping wing to predict the aerodynamic loads, while the real fluid motion around the wing has time memory. Taking hovering as an example, as shown in Figure 2.10, compared to the first stroke cycle, the vertical force of the following stroke cycles decreases by about 15%. This reduction is due to the existence of downwash as shown in Figure 2.11.

Although there exist reliable downwash models for hovering flight (Oh, Lee *et al.* 2020), they are unlikely to generalize to arbitrary flight conditions. As shown in Figure 2.10, the wake is almost fully developed at the second stroke cycle. The variation of peak value during downstroke is negative for hovering and slow forward speed 1 m/s and positive for relatively fast forward speeds 2 m/s, 3 m/s, 4 m/s and 5 m/s. The variation reaches maximum for medium forward velocity 2 m/s and 3 m/s.

In comparison with the flapping in quiescent air during the first stroke cycle, the surrounding flow (during the second stroke cycle) induced by the previous cycle varies with the flight speed. Figure 2.11 shows the flow field around the mid-downstroke during the first and second stroke cycles. It can be seen that before the mid-downstroke for hovering, there exists a large area of flow with downward velocity, called downwash. When the wing encounters with this downwash, the effective angle of attack decreases which causes the reduction of lift. In this study, the effect of downwash is included into the fitted coefficients. Conversely, for forward speed 3 m/s, there exists an area of flow with upward velocity, we call it upwash. During the downstroke, the wing encounters with this upwash, the effective angle of attack increases which causes the rise of lift. For large forward speed 5 m/s, there also exists an area of flow with upward velocity, but it is weaker than that for 3 m/s forward speed, so its contribution to lift enhancement is small. To elucidate how the downwash and upwash are generated and how they interact with the flapping wing, we illustrate the vortex structure around the flying bumblebee, see Figure 2.12. For all the three forward speeds, there is a vortex tube connecting to the wing tip behind the wing during upstroke which originates from the detached trailing edge vortex, see Figure 2.12*a*, *b* and *c*. The fluid flows downward through the area bounded by the vortex tube and the wing. Outside this area, the fluid flows upward. Such fluid motion is maintained by the vortex tube in the following downstroke but its interaction with the flapping wing varies with forward speed. For hovering, the downwash locates by the side of the body. This downwash interacts with the flapping wing, resulting in reduction of force, see Figure 2.12*d*. For the forward speed 3m/s, the vortex tube moves behind the bumblebee and the upwash moves to the side of the body and interacts with the flapping wing resulting in increment of force, see Figure 2.12*e*. For the forward speed 5m/s, the vortex tube moves further behind the bumblebee and both the areas of downwash and upwash move behind the bumblebee, so there are almost no interactions between the downwash and/or upwash and flapping wing, see Figure 2.12*f*.

2.5.2 Trim state of modeled bumblebee in forward flight

The CDAM is demonstrated to precisely predict the aerodynamic force, torque and power for a flying bumblebee with vast range of velocity and various wing kinematics. Now, we further demonstrate the predictive capacity of CDAM by finding the trim state of a bumblebee in forward flight. In forward flight, the body posture, stroke plane and wing kinematics differ from those in hovering flight. If a bumblebee flies forward at a constant speed, its equilibrium state has to satisfy three conditions (so called trim conditions): cycle-averaged forward/backward aerodynamic force equals zero; cycle averaged vertical aerodynamic force equals the weight of the bumblebee; cycle-averaged aerodynamic pitching moment equals zero. Here, a genetic optimization algorithm based on the derandomized evolution strategy with covariance matrix adaptation (CMA-ES) is used to find the trim state (Hansen, Müller *et al.* 2003; Hansen and Kern 2004). The cost function is defined as

$$c = {}_g\bar{F}_x^2 + \left({}_g\bar{F}_z - W\right)^2 + {}_b\bar{T}_y^2 \tag{2.36}$$

Where ${}_g\bar{F}_x$ is the cycle-averaged forward/backward aerodynamic force, ${}_g\bar{F}_z$ is the cycle-averaged vertical aerodynamic force, W is the weight of the bumblebee, ${}_b\bar{T}_y$ is the cycle-averaged aerodynamic pitching moment.

Keeping the body angle, the stroke plane angle and the forward velocity constant, we tune the wingbeat frequency, the positional angle amplitude and mean value, and the feathering amplitude and mean value. The minimal positional angle (φ_{min}) is varied to control the flapping amplitude and mean value, while the maximal positional angle (φ_{max}) remains constant during the optimization. The maximal feathering angle (η_{max}) is varied to control the feathering amplitude and mean value, while the minimal feathering angle (η_{min}) remains constant during the optimization. This is illustrated in Figure 2.13. The genetic algorithm is used to tune the three input variables (*f*, φ_{min} and η_{max}) to minimize the cost function. If the trim condition is reached, the cost function becomes zero. The initial value of the frequency is 136 Hz, the initial flapping angle amplitude is 137 degrees and the initial feathering angle amplitude is 125 degrees. According to the measurements on the bumblebees done by (Dudley and Ellington 1990), we set the upper bound in genetic optimization algorithm (Hansen, Müller *et al.* 2003; Hansen and Kern 2004) to be [175 Hz, 140 degrees, 140 degrees] and lower bound to be [120 HZ, 90 degrees, 100 degrees]. We set initial population with size 50 randomly sampled within the lower bound and upper bound. It would be prohibitively time-consuming to minimize the cost function (2.36) using CFD simulation directly to calculate the aerodynamic forces and torques. Instead, we use CDAM. It took about 1000 evaluations (~10 minutes) to complete the optimization. Here, we focus on the flight with forward speed 1.005 m/s. The trim states found are listed in Table 2.6. To check the accuracy of the trim states found by the CDAM, the predictions of both CDAM and CFD are plotted in Figure 2.9a, c, e and g. The agreement is satisfactory.

The solution for the trim conditions is the intersection of three isosurfaces, i.e. ${}_g\bar{F}_x = 0$, ${}_g\bar{F}_z = W$ and ${}_b\bar{T}_y = 0$. Here, we plot the three isosurfaces for case 6 listed in Table 2.6 with the body angle and the stroke plane angle similar to those measured by (Dudley and Ellington 1990; Dudley and Ellington 1990), see Figure 2.14. For the isosurface ${}_g\bar{F}_x = 0$, feathering amplitude is almost constant, so the forward/backward force ${}_g\bar{F}_x$ is sensitive to the feathering amplitude and insensitive to the flapping amplitude and frequency. From the isosurface ${}_g\bar{F}_z = W$, it can be concluded that the vertical force ${}_g\bar{F}_z$ is weakly sensitive to feathering amplitude. From the isosurface ${}_b\bar{T}_y = 0$, it can be concluded that the pitch torque ${}_b\bar{T}_y$ is not sensitive to the flapping frequency. To balance the pitch torque, feathering amplitude has to be increased for smaller flapping amplitude, and vice versa. There is only one point of intersection of the three isosurfaces, hence, there is only one solution to the trim conditions, if the body and the stroke plane angles are prescribed.

2.6 Fully nonlinear dynamic model

2.6.1 Dynamic model establishment

Insects with paired wings are usually assumed as a rigid body (Sun and Xiong 2005; Gao, Aono *et al.* 2009; Gao, Aono *et al.* 2011), of which the inertial force induced by reciprocating wings is neglected. This assumption is reasonable when the wing beat frequency is high or the wing is light (Sun, Wang *et al.* 2007; Taha, Kiani *et al.* 2020). In addition, many dynamic equations of flapping-wing insects are only applicable to small deviations from equilibrium state (Gao, Aono *et al.* 2011; Taha, Tahmasian *et al.* 2015; Zhang and Liu 2018) by neglecting high-order terms, which is not suitable for extreme motions under large perturbations. Furthermore, few dynamic models (Bluman, Sridhar *et al.* 2018) are available to simulate the free flapping flight with passive responds of the wing (flexible wing hinge or deformable wing membrane) to active actuation and unsteady aerodynamic loads. In order to derive a versatile fully nonlinear dynamic model applicable to arbitrary pair-winged systems like flapping-wing insects and FWMAVs in free or trimmed flights with flexible wing hinges that take the effects of reciprocating wings into account, here we propose a dynamic simulator extended from prior work (Gebert, Gallmeier *et al.* 2002; Sun, Wang *et al.* 2007), which is capable of simulating the interactions between insect body and wings. The governing dynamic equations of the insect body can be given as,

$$\begin{pmatrix} m_b + a_{1v} & A_{1o} & B_{1wR} & B_{1wL} \\ A_{2vR} + A_{2vL} & I_{bd} + A_{2oR} + A_{2oL} & B_{2wR} & B_{2wL} \end{pmatrix} \frac{\mathrm{d}}{\mathrm{d}t} \begin{pmatrix} {}_b\boldsymbol{v}_{cg} \\ {}_b\boldsymbol{\omega}_{bd} \\ \boldsymbol{\omega}_{R0b} \\ \boldsymbol{\omega}_{L0b} \end{pmatrix} =$$

$$\begin{pmatrix} {}_b\boldsymbol{F}_{a,bd} + {}_b\boldsymbol{F}_{a,R} + {}_b\boldsymbol{F}_{a,L} + m_b\,{}_b g - m_b\,{}_b\boldsymbol{\omega}_{bd} \times {}_b\boldsymbol{v}_{cg} - a_1 - b_1 \\ {}_b\boldsymbol{M}_{a,bd} + {}_b\boldsymbol{M}_{a,R} + {}_b\boldsymbol{M}_{a,L} - {}_b\boldsymbol{\omega}_{bd} \times \left(I_{bd}\,{}_b\boldsymbol{\omega}_{bd}\right) - (a_{2R} + a_{2L}) - (b_{2R} + b_{2L}) \end{pmatrix} \tag{2.37}$$

where expressions of the coefficients a_{1v}, A_{1o}, B_{1wR}, B_{1wL}, a_1, b_1, A_{2vR}, A_{2vL}, A_{2oR}, A_{2oL}, B_{2wR}, B_{2wL}, a_{2R}, a_{2L}, b_{2R} and b_{2L} are summarized in *Appendix*. ${}_b\boldsymbol{F}_{a,bd}$, ${}_b\boldsymbol{F}_{a,R}$, ${}_b\boldsymbol{F}_{a,L}$, ${}_b\boldsymbol{M}_{a,bd}$, ${}_b\boldsymbol{M}_{a,R}$ and ${}_b\boldsymbol{M}_{a,L}$ are the aerodynamic forces and moments acting on the body, right wing and left wing, respectively, which can be calculated through the CDAM, CFD simulation (Liu and Kawachi 1998; Liu 2009) or experimental measurement (Dickinson, Lehmann *et al.* 1999) in the manner of loose coupling, therefore, the dynamic simulator accounts for the fluid-structure interaction (FSI). The dynamic equations of right and left wings can be further defined as,

$$\begin{pmatrix} A_{2vR} + C_{vR} & A_{2oR} - C_{oR} & B_{2wR} - C_{wR} & 0 \\ A_{2vL} + C_{vL} & A_{2oL} - C_{oL} & 0 & B_{2wL} - C_{wL} \end{pmatrix} \frac{\mathrm{d}}{\mathrm{d}t} \begin{pmatrix} {}_b\boldsymbol{v}_{cg} \\ {}_b\boldsymbol{\omega}_{bd} \\ \boldsymbol{\omega}_{R0b} \\ \boldsymbol{\omega}_{L0b} \end{pmatrix} - \begin{pmatrix} \boldsymbol{M}_{b2R} \\ \boldsymbol{M}_{b2L} \end{pmatrix}$$

$$= \begin{pmatrix} {}_b\boldsymbol{M}_{a,R} - a_{2R} - b_{2R} + c_R \\ {}_b\boldsymbol{M}_{a,L} - a_{2L} - b_{2L} + c_L \end{pmatrix} \tag{2.38}$$

where expressions of the coefficients C_{vR}, C_{oR}, C_{wR}, c_R, C_{vL}, C_{oL}, C_{wL} and c_L are also summarized in *Appendix*. $\boldsymbol{M}_{b2R}$ and $\boldsymbol{M}_{b2L}$ are the torques due to the interactions between the body and two wings, which determine the wing motion. The relation between the velocity and position is

$$\frac{\mathrm{d}\boldsymbol{r}}{\mathrm{d}t} = E_{b2g}\,{}_b\boldsymbol{v}_{cg} \tag{2.39}$$

To avoid the singularity, the quaternion is adopted here to describe the attitude of the insect body, thus the relation between the angular velocity of the body and quaternion is

$$\frac{\mathrm{d}}{\mathrm{d}t}\begin{pmatrix} q_1 \\ q_2 \\ q_3 \\ q_4 \end{pmatrix} = \frac{1}{2}\begin{pmatrix} -q_2 & -q_3 & -q_4 \\ q_1 & -q_4 & q_3 \\ q_4 & q_1 & -q_2 \\ -q_3 & q_2 & q_1 \end{pmatrix} {}_b\boldsymbol{\omega}_{bd} \tag{2.40}$$

The relations between the angular velocities of the right and left wing and the wing Euler angles are

$$E_{spR2b}E_{dEulerR2sp}\frac{\mathrm{d}}{\mathrm{d}t}\begin{pmatrix} \varphi_R \\ \theta_R \\ \eta_R \end{pmatrix} = \boldsymbol{\omega}_{R0b} \tag{2.41}$$

$$E_{spL2b}E_{dEulerL2sp}\frac{\mathrm{d}}{\mathrm{d}t}\begin{pmatrix} \varphi_L \\ \theta_L \\ \eta_L \end{pmatrix} = \boldsymbol{\omega}_{L0b} \tag{2.42}$$

To simulate the tethered flight, it is easy to just add the following two equations,

$$\frac{d\ {}_{b}\boldsymbol{v}_{cg}}{dt}=0 \tag{2.43}$$

$$\begin{pmatrix} -q_2-q_3 & q_2-q_3 & q_1-q_4 \\ q_1 & -q_4 & q_3 \\ q_4 & q_1 & -q_2 \end{pmatrix}\frac{\mathrm{d}\ {}_{b}\boldsymbol{\omega}_{bd}}{\mathrm{d}t}+$$
$$\begin{pmatrix} {}_{b}\boldsymbol{\omega}_{bd,z} & -{}_{b}\boldsymbol{\omega}_{bd,x}+{}_{b}\boldsymbol{\omega}_{bd,y} & -{}_{b}\boldsymbol{\omega}_{bd,x}-{}_{b}\boldsymbol{\omega}_{bd,y} & -{}_{b}\boldsymbol{\omega}_{bd,z} \\ {}_{b}\boldsymbol{\omega}_{bd,x} & 0 & {}_{b}\boldsymbol{\omega}_{bd,z} & -{}_{b}\boldsymbol{\omega}_{bd,y} \\ {}_{b}\boldsymbol{\omega}_{bd,y} & -{}_{b}\boldsymbol{\omega}_{bd,z} & 0 & {}_{b}\boldsymbol{\omega}_{bd,x} \end{pmatrix}\frac{\mathrm{d}}{\mathrm{d}t}\begin{pmatrix} q_1 \\ q_2 \\ q_3 \\ q_4 \end{pmatrix}=0 \tag{2.44}$$

Equation (2.43) forces the insect not to move and equation (2.44) forces the insect not to rotate.

(i) To achieve a desired wing motion M_{b2R} and M_{b2L} need to be precisely tuned. To link the M_{b2R} and M_{b2L} and the desired wing kinematics of a flapping wing system, we need to further add the following equations,

$$\dot{E}_{dEulerR2sp}^{-1}E'_{spR2b}\boldsymbol{\omega}_{R0b}+E_{dEulerR2sp}^{-1}E'_{spR2b}\frac{d\boldsymbol{\omega}_{R0b}}{dt}=\begin{pmatrix} \ddot{\varphi}_R \\ \ddot{\theta}_R \\ \ddot{\eta}_R \end{pmatrix} \tag{2.45}$$

$$\dot{E}_{dEulerL2sp}^{-1}E'_{spL2b}\boldsymbol{\omega}_{L0b}+E_{dEulerL2sp}^{-1}E'_{spL2b}\frac{d\boldsymbol{\omega}_{L0b}}{dt}=\begin{pmatrix} \ddot{\varphi}_L \\ \ddot{\theta}_L \\ \ddot{\eta}_L \end{pmatrix} \tag{2.46}$$

where the second derivatives of flapping angles $\ddot{\varphi}_R$, $\ddot{\theta}_R$, $\ddot{\eta}_R$, $\ddot{\varphi}_L$, $\ddot{\theta}_L$ and $\ddot{\eta}_L$ are the wing kinematics inputs. The motion of a flapping-wing system can be solved by integrating equations (2.37) ~ (2.46).

(ii) The dynamic simulator can be directly applied to the case where the wing hinge is (partially) flexible. For instance, the positional motion is prescribed under active actuation control and the elevation and feathering motions are passively driven by the interaction among the torsional spring at the wing hinge, the inertial load and aerodynamic load. To this extent, the interactions between the wing and body along elevation and feathering are

$$M_{k,elev}=-k_{elev}(\theta-\theta_0)-c_\theta\dot{\theta} \tag{2.47}$$
$$M_{k,feath}=-k_{feath}(\eta-\eta_0)-c_\eta\dot{\eta} \tag{2.48}$$

where k_{elev} and k_{feath} are the stiffness, c_θ and c_η are the damping coefficients, θ_0 and η_0 are the resting position. Furthermore, the positional motion can also be modelled to be actuated by active-drive spring torque, such as

$$M_{k,posi}=-k_{posi}(\varphi-\varphi_0)+d\,\mathrm{sgn}(\dot{\varphi}) \tag{2.49}$$

where k_{posi} is the stiffness, d is the driving torque, φ_0 is the resting position.

2.6.2 Time independence validation

The dynamic model is loosely coupled with either the CFD simulation or CDAM. Here, we validate the dynamic model by coupling with CFD simulation. The accuracy on the grids for flapping wing insects has been validated repeatedly by the CFD simulator (Liu and Kawachi 1998; Liu 2009). We hereby further validate the accuracy on time step of the proposed dynamic simulator under passive elevation and feathering. The testing case are taken at the elevation stiffness equaling $190k_0$, feathering stiffness equaling k_0, positional stiffness equaling $15k_0$ with power source $d = 2.8 \times 10^{-5} Nm$, where $k_0 = 2.61 \times 10^{-6} Nm$ is taken from (Kolomenskiy, Ravi *et al.* 2019). Figure 2.15 shows the dependence of wing kinematics on different time steps of the flapping wing driven passively. It can be seen that the resultant wing motion is independent on the time steps.

References

Andersen, A., Pesavento, U., Wang, Z. J., Unsteady Aerodynamics of Fluttering and Tumbling Plates, Journal of Fluid Mechanics, Vol. 541, No. (2005),pp. 65-90.

Beatus, T., Cohen, I., Wing-Pitch Modulation in Maneuvering Fruit Flies Is Explained by an Interplay between Aerodynamics and a Torsional Spring, Physical Review E, Vol. 92, No. 2 (2015),pp. 022712.

Bergou, A. J., Ristroph, L., Guckenheimer, J., Cohen, I., Wang, Z. J., Fruit Flies Modulate Passive Wing Pitching to Generate in-Flight Turns, Physical Review Letters, Vol. 104, No. 14 (2010),pp. 148101.

Bluman, J., Kang, C.-K., Wing-Wake Interaction Destabilizes Hover Equilibrium of a Flapping Insect-Scale Wing, Bioinspiration & Biomimetics, Vol. 12, No. 4 (2017),pp. 046004.

Bluman, J. E., Sridhar, M. K., Kang, C.-k., Chordwise Wing Flexibility May Passively Stabilize Hovering Insects, Journal of the Royal Society Interface, Vol. 15, No. 147 (2018),pp. 20180409.

Cheng, X., Sun, M., Very Small Insects Use Novel Wing Flapping And drag Principle to Generate the Weight-Supporting Vertical Force, Journal of Fluid Mechanics, Vol. 855, No. (2018),pp. 646-670.

Deng, X., Schenato, L., Sastry, S. S., Flapping Flight for Biomimetic Robotic Insects: Part Ii-Flight Control Design, IEEE Transactions on Robotics, Vol. 22, No. 4 (2006),pp. 789-803.

Dickinson, M. H., Lehmann, F.-O., Sane, S. P., Wing Rotation and the Aerodynamic Basis of Insect Flight, Science, Vol. 284, No. 5422 (1999),pp. 1954.

Dickson, W. B., Dickinson, M. H., The Effect of Advance Ratio on the Aerodynamics of

Revolving Wings, Journal of Experimental Biology, Vol. 207, No. 24 (2004),pp. 4269-4281.

Dudley, R., Ellington, C. P., Mechanics of Forward Flight in Bumblebees: I. Kinematics and Morphology, Journal of Experimental Biology, Vol. 148, No. 1 (1990),pp. 19.

Dudley, R., Ellington, C. P., Mechanics of Forward Flight in Bumblebees: Ii. Quasi-Steady Lift and Power Requirements, Journal of Experimental Biology, Vol. 148, No. 1 (1990),pp. 53-88.

Engels, T., Kolomenskiy, D., Schneider, K., Sesterhenn, J. r., Flusi: A Novel Parallel Simulation Tool for Flapping Insect Flight Using a Fourier Method with Volume Penalization, SIAM Journal on Scientific Computing, Vol. 38, No. 5 (2016),pp. S3-S24.

Fei, F., Tu, Z., Yang, Y., Zhang, J., Deng, X. Flappy Hummingbird: An Open Source Dynamic Simulation of Flapping Wing Robots and Animals. 2019 International Conference on Robotics and Automation (ICRA), IEEE, 2019

Fujii, K., Unified Zonal Method Based on the Fortified Solution Algorithm, Journal of Computational Physics, Vol. 118, No. 1 (1995),pp. 92-108.

Fung, Y. C., An Introduction to the Theory of Aeroelasticity, Courier Dover Publications (2008)

Gao, N., Aono, H., Liu, H., A Numerical Analysis of Dynamic Flight Stability of Hawkmoth Hovering, Journal of Biomechanical Science and Engineering, Vol. 4, No. 1 (2009),pp. 105-116.

Gao, N., Aono, H., Liu, H., Perturbation Analysis of 6dof Flight Dynamics and Passive Dynamic Stability of Hovering Fruit Fly Drosophila Melanogaster, Journal of Theoretical Biology, Vol. 270, No. 1 (2011),pp. 98-111.

Gebert, G., Gallmeier, P., Evers, J., Equations of Motion for Flapping Flight, Aiaa Atmospheric Flight Mechanics Conference and Exhibit, American Institute of Aeronautics and Astronautics (2002)

Hansen, N., Kern, S. Evaluating the Cma Evolution Strategy on Multimodal Test Functions, Berlin, Heidelberg, Springer Berlin Heidelberg, 2004

Hansen, N., Müller, S. D., Koumoutsakos, P., Reducing the Time Complexity of the Derandomized Evolution Strategy with Covariance Matrix Adaptation (Cma-Es), Evolutionary Computation, Vol. 11, No. 1 (2003),pp. 1-18.

Hedrick, T. L., Cheng, B., Deng, X., Wingbeat Time and the Scaling of Passive Rotational Damping in Flapping Flight, Science, Vol. 324, No. 5924 (2009),pp. 252.

Ishihara, D., Role of Fluid-Structure Interaction in Generating the Characteristic Tip Path of a Flapping Flexible Wing, Physical Review E, Vol. 98, No. 3 (2018),pp. 032411.

Jensen, M., Biology and Physics of Locust Flight. Iii. The Aerodynamics of Locust Flight, Philosophical Transactions of the Royal Society of London. Series B, Biological Sciences, Vol. 239, No. 667 (1956),pp. 511-552.

Kolomenskiy, D., Ravi, S., Xu, R., Ueyama, K., Jakobi, T., Engels, T., Nakata, T., Sesterhenn, J., Schneider, K., Onishi, R., Liu, H., The Dynamics of Passive Feathering Rotation in Hovering Flight of Bumblebees, Journal of Fluids and Structures, Vol. 91, No. (2019),pp. 102628.

Lee, Y. J., Lua, K. B., Lim, T. T., Yeo, K. S., A Quasi-Steady Aerodynamic Model for Flapping Flight with Improved Adaptability, Bioinspiration & Biomimetics, Vol. 11, No. 3 (2016),pp. 036005.

Liu, G., Dong, H., Li, C., Vortex Dynamics and New Lift Enhancement Mechanism of Wing–Body Interaction in Insect Forward Flight, Journal of Fluid Mechanics, Vol. 795, No. (2016),pp. 634-651.

Liu, H., Simulation-Based Biological Fluid Dynamics in Animal Locomotion, Applied Mechanics Reviews, Vol. 58, No. 4 (2005),pp. 269-282.

Liu, H., Integrated Modeling of Insect Flight: From Morphology, Kinematics to Aerodynamics, Journal of Computational Physics, Vol. 228, No. 2 (2009),pp. 439-459.

Liu, H., Ellington, C. P., Kawachi, K., van den Berg, C., Willmott, A. P., A Computational Fluid Dynamic Study of Hawkmoth Hovering, The Journal of Experimental Biology, Vol. 201, No. 4 (1998),pp. 461.

Liu, H., Kawachi, K., A Numerical Study of Insect Flight, Journal of Computational Physics, Vol. 146, No. 1 (1998),pp. 124-156.

Liu, H., Ravi, S., Kolomenskiy, D., Tanaka, H., Biomechanics and Biomimetics in Insect-Inspired Flight Systems, Philosophical Transactions of the Royal Society B: Biological Sciences, Vol. 371, No. 1704 (2016),pp. 20150390.

Lophaven, S. N., Nielsen, H. B., Sondergaard, J., Dace, A., A Matlab Kriging Toolbox, Technical University of Denmark Report IMM-TR-2002-12, Vol. (2002),pp.

Ma, K. Y., Chirarattananon, P., Fuller, S. B., Wood, R. J., Controlled Flight of a Biologically Inspired, Insect-Scale Robot, Science, Vol. 340, No. 6132 (2013),pp. 603.

Nabawy, M. R., Crowther, W. J., On the Quasi-Steady Aerodynamics of Normal Hovering Flight Part Ii: Model Implementation and Evaluation, Journal of the Royal Society Interface, Vol. 11, No. 94 (2014),pp. 20131197.

Nakata, T., Liu, H., Bomphrey, R. J., A Cfd-Informed Quasi-Steady Model of Flapping-Wing Aerodynamics, Journal of Fluid Mechanics, Vol. 783, No. (2015),pp. 323-343.

Nguyen, T., Sundar, D. S., Yeo, K. S., Lim, T. T., Modeling and Analysis of Insect-Like Flexible Wings at Low Reynolds Number, Journal of Fluids and Structures, Vol. 62, No. (2016),pp. 294-317.

Oh, S., Lee, B., Park, H., Choi, H., Kim, S.-T., A Numerical and Theoretical Study of the Aerodynamic Performance of a Hovering Rhinoceros Beetle (Trypoxylus Dichotomus), Journal of Fluid Mechanics, Vol. 885, No. (2020),pp. A18.

Pesavento, U., Wang, Z. J., Falling Paper: Navier-Stokes Solutions, Model of Fluid Forces, and Center of Mass Elevation, Physical Review Letters, Vol. 93, No. 14 (2004),pp. 144501.

Sane, S. P., Dickinson, M. H., The Aerodynamic Effects of Wing Rotation and a Revised Quasi-Steady Model of Flapping Flight, Journal of Experimental Biology, Vol. 205, No. 8 (2002),pp. 1087-1096.

Sedov, L. I., Two-Dimensional Problems in Hydrodynamics and Aerodynamics, Interscience Publishers (1965)

Sun, M., Wang, J., Xiong, Y., Dynamic Flight Stability of Hovering Insects, Acta Mechanica Sinica, Vol. 23, No. 3 (2007),pp. 231-246.

Sun, M., Xiong, Y., Dynamic Flight Stability of a Hovering Bumblebee, The Journal of Experimental Biology, Vol. 208, No. 3 (2005),pp. 447.

Taha, H. E., Kiani, M., Hedrick, T. L., Greeter, J. S. M., Vibrational Control: A Hidden Stabilization Mechanism in Insect Flight, Science Robotics, Vol. 5, No. 46 (2020),pp. eabb1502.

Taha, H. E., Tahmasian, S., Woolsey, C. A., Nayfeh, A. H., Hajj, M. R., The Need for Higher-Order Averaging in the Stability Analysis of Hovering, Flapping-Wing Flight, Bioinspiration & Biomimetics, Vol. 10, No. 1 (2015),pp. 016002.

Usherwood, J. R., Ellington, C. P., The Aerodynamics of Revolving Wings Ii. Propeller Force Coefficients from Mayfly to Quail, Journal of Experimental Biology, Vol. 205, No. 11 (2002),pp. 1565-1576.

Van Veen, W. G., van Leeuwen, J. L., Muijres, F. T., A Chordwise Offset of the Wing-Pitch Axis Enhances Rotational Aerodynamic Forces on Insect Wings: A Numerical Study, Journal of the Royal Society Interface, Vol. 16, No. 155 (2019),pp. 20190118.

Wang, Q., Goosen, J., Van Keulen, F., A Predictive Quasi-Steady Model of Aerodynamic Loads on Flapping Wings, J. Fluid Mech, Vol. 800, No. (2016),pp. 688-719.

Whitney, J. P., Wood, R. J., Aeromechanics of Passive Rotation in Flapping Flight, Journal of Fluid Mechanics, Vol. 660, No. (2010),pp. 197.

Yu, X., Sun, M., A Computational Study of the Wing–Wing and Wing–Body Interactions of a Model Insect, Acta Mechanica Sinica, Vol. 25, No. 4 (2009),pp. 421-431.

Zhang, C., Hedrick, T. L., Mittal, R., An Integrated Study of the Aeromechanics of Hovering Flight in Perturbed Flows, AIAA Journal, Vol. 57, No. 9 (2019),pp. 3753-3764.

Zhang, X., Liu, H., A Three-Axis Pd Control Model for Bumblebee Hovering Stabilization, Journal of Bionic Engineering, Vol. 15, No. 3 (2018),pp. 494-504.

List of figures

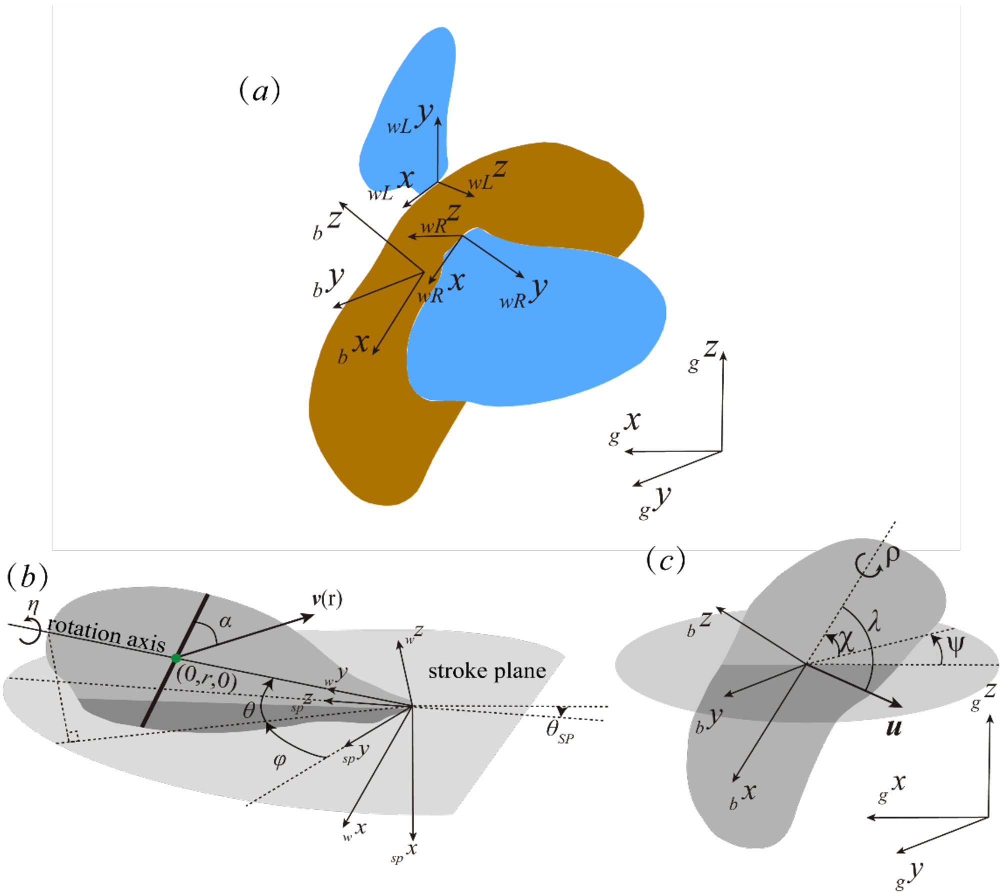

Figure 2.1 (*a*) An overview of the integrated wing-body model of a bumblebee with the definitions of right wing-fixed frame $\left({}_{wR}x, {}_{wR}y, {}_{wR}z\right)$, left wing-fixed frame $\left({}_{wL}x, {}_{wL}y, {}_{wL}z\right)$, body-fixed frame $\left({}_{b}x,\ {}_{b}y,\ {}_{b}z\right)$ and ground frame $\left({}_{g}x,\ {}_{g}y,\ {}_{g}z\right)$. (*b*) A sketch of a single wing (either right wing or left wing) with the definitions of the stroke plane frame $\left({}_{sp}x, {}_{sp}y, {}_{sp}z\right)$, stroke plane angle θ_{SP}, positional angle φ, elevation angle θ and feathering angle η. $\boldsymbol{v}(r)$ represents the velocity of a blade element on the wing with the distance r to the wing base and α represents the corresponding angle of attack. (*c*) A sketch of the body with the definitions of the yaw angle ψ, the pitch angle χ and the roll angle ρ. $\boldsymbol{u}$ represents the velocity of the body and λ represents the corresponding angle of attack.

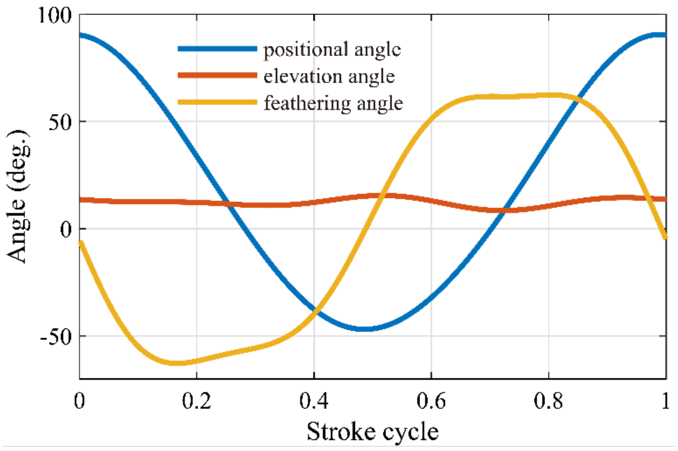

Figure 2.2 Wing kinematics of a hovering bumblebee (adopted from Kolomenskiy et al (Kolomenskiy, Ravi *et al.* 2019)).

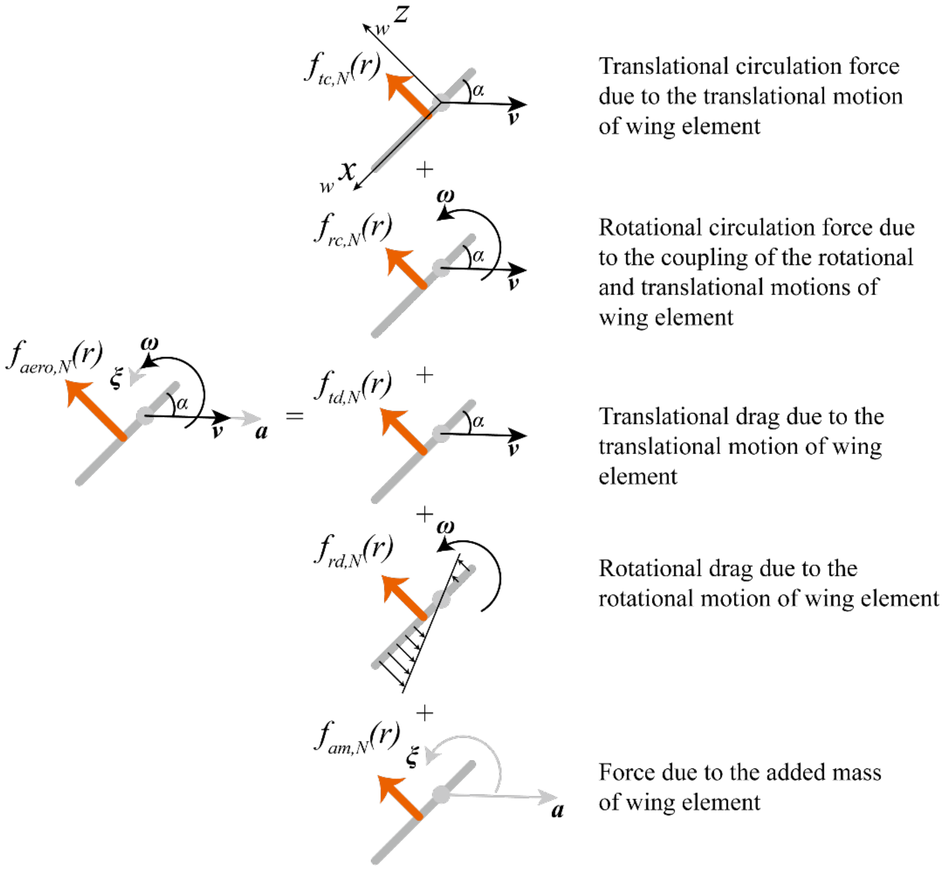

Figure 2.3 Total aerodynamic force on a wing element can be decomposed into five quasi-steady terms.

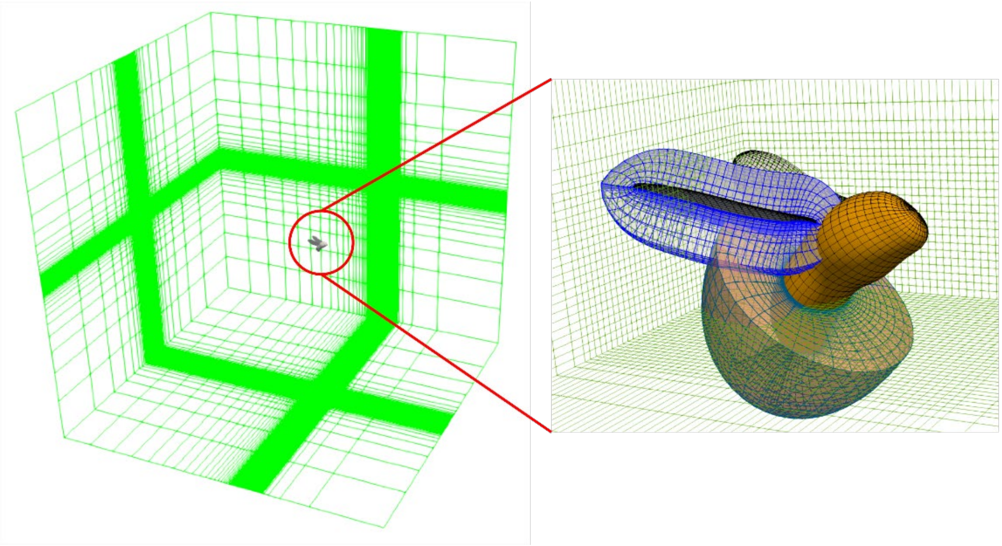

Figure 2.4 An overview of the integrated wing-body CFD model of a bumblebee.

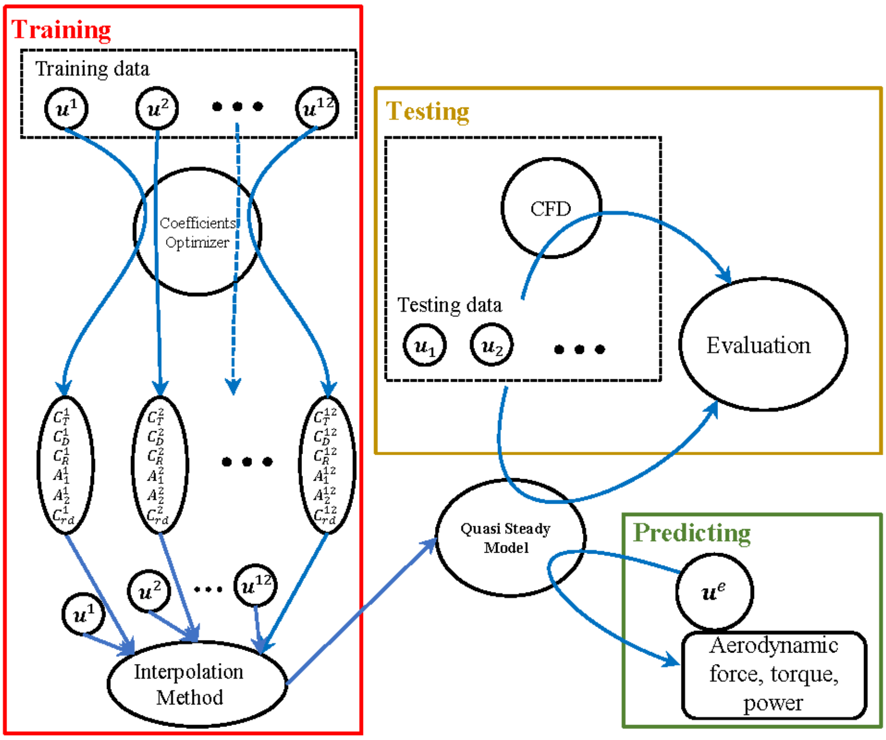

Figure 2.5 The whole procedure to construct the quasi-steady model for a flapping wing. Coefficients Optimizer is formulized by equation (2.34) which is used to fit the coefficients of selected velocities. The interpolation method is implemented to obtain the coefficients for arbitrary flying velocity to enclose the quasi-steady model for flapping wing which is realized by a MATLAB toolbox DACE (Lophaven, Nielsen *et al.* 2002). Random velocities are selected as testing data to evaluate the accuracy of the quasi-steady model by comparing the simulation results from quasi-steady model and CFD. Thereafter, the quasi-steady model can be used to predict the aerodynamic force, torque and power of flapping wings.

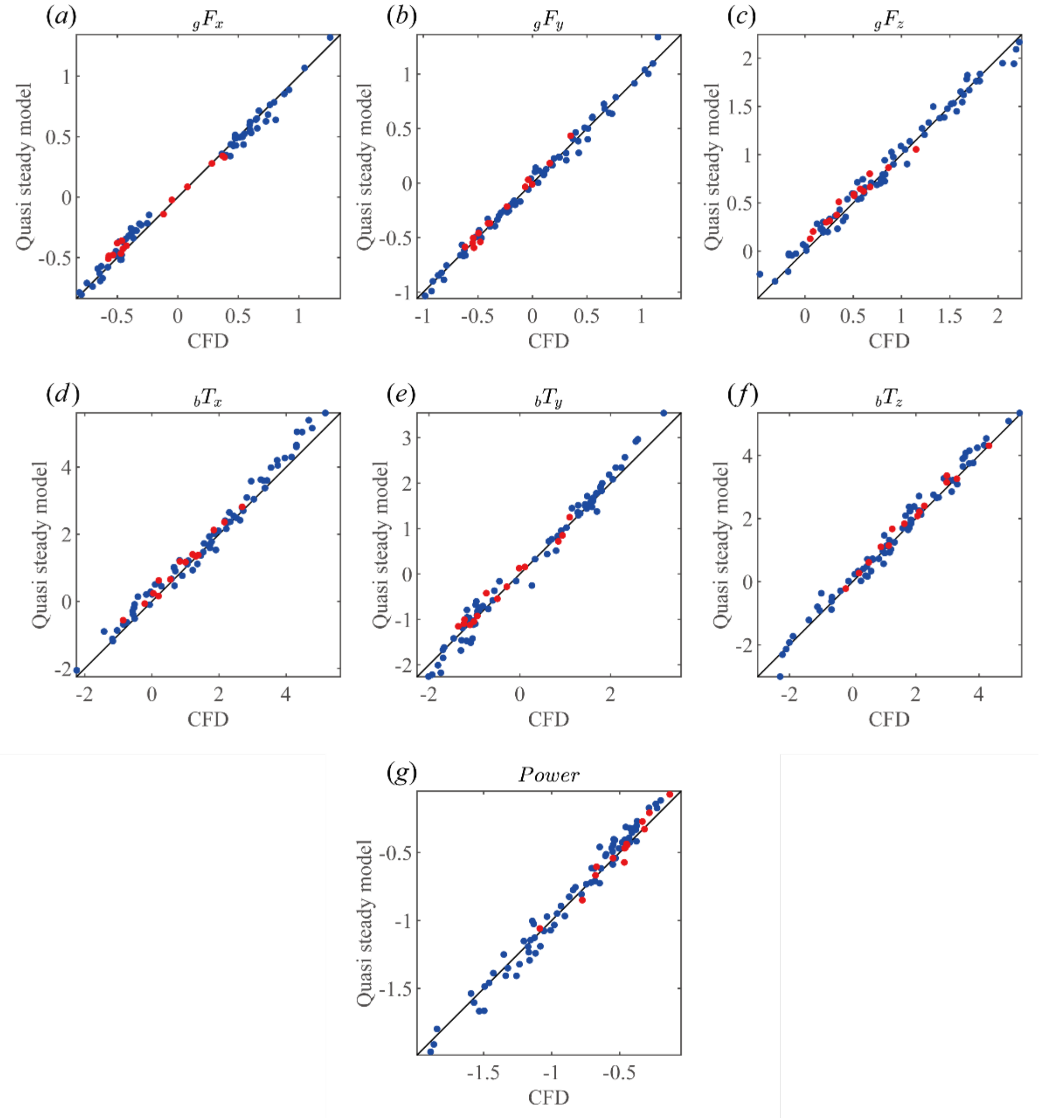

Figure 2.6 Comparison between prediction of quasi-steady model and CFD database for flapping wing. (*a*-*c*) Aerodynamic forces in ground frame, nondimensionalized by $\rho U_{ref}^2 c_m^2$. (*d*-*f*) Aerodynamic torques with respect to center of body mass of modeled bumblebee in body-fixed frame, nondimensionalized by $\rho U_{ref}^2 c_m^3$. (g) Aerodynamic power consumptions, nondimensionalized by $\rho U_{ref}^3 c_m^2$. Blue: Training database. Red: Test database. Solid line represents the equality of prediction of quasi-steady model and CFD results.

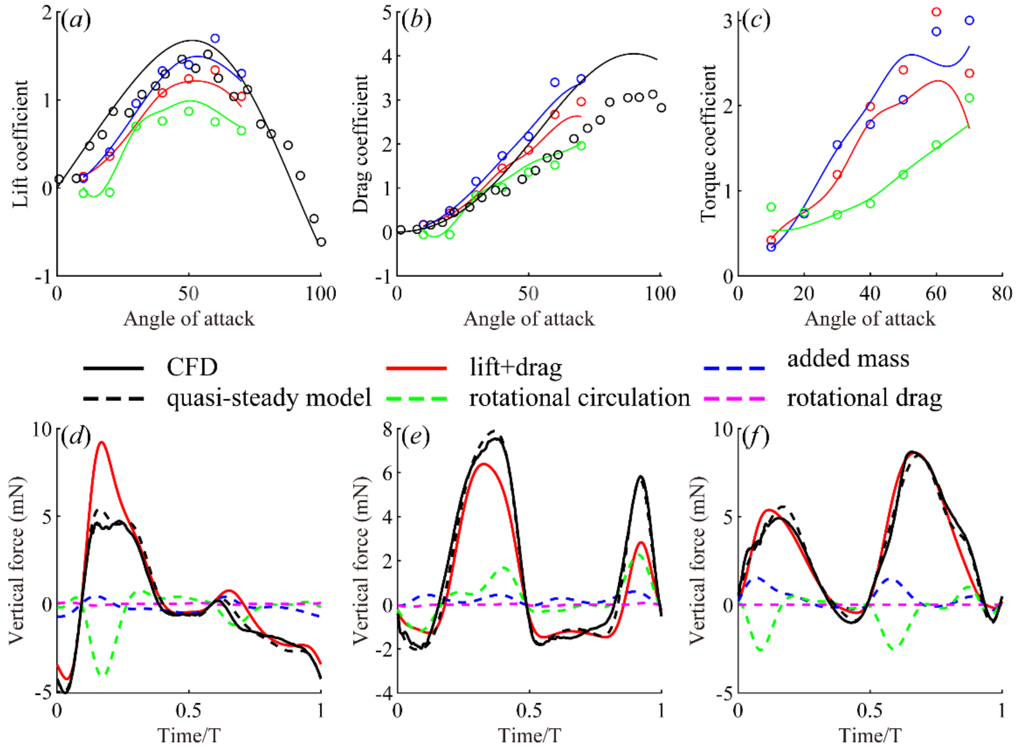

Figure 2.7 (*a*) Translational lift, (*b*) translational drag and (*c*) torque coefficients for forward $0.4U_{ref}$, rightward $0.4U_{ref}$ and upward $0.4U_{ref}$ (red), forward $0.4U_{ref}$, leftward $0.4U_{ref}$ and upward $0.4U_{ref}$ (blue) and backward $0.4U_{ref}$, rightward $0.4U_{ref}$ and zero vertical speed (green). Line: quasi-steady model. Circle: CFD. The lift coefficient (*a*) and drag coefficient (*b*) for hovering revolving wing by present model (black line) and measured by (Usherwood and Ellington 2002) (black circles) are also shown for comparison. (*d*) to (*f*): Force components of the quas-steady model in comparison with the CFD results corresponding to the three flying velocities: $(-0.4,\ 0.4,\ 0.4)\ U_{ref}$, $(-0.4, -0.4,\ 0.4)\ U_{ref}$ and $(0.4,\ 0.4,\ 0)\ U_{ref}$.

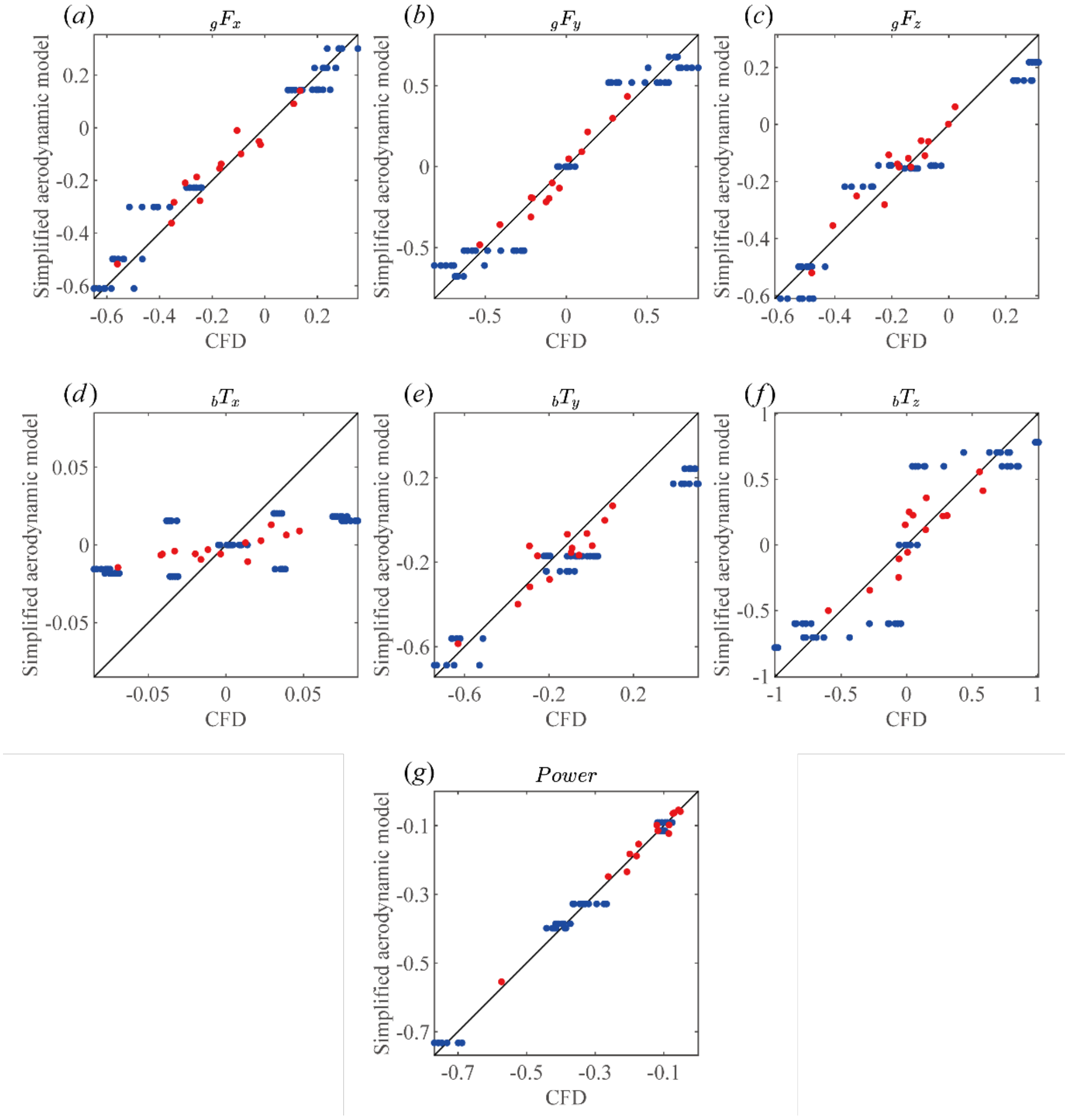

Figure 2.8 Comparison between prediction of simplified aerodynamic model and CFD database for moving body. (*a*-*c*) Aerodynamic forces in ground frame, nondimensionalized by $\rho U_{ref}^2 c_m^2$. (*d*-*f*) Aerodynamic torques with respect to center of body mass of modeled bumblebee in body-fixed frame, nondimensionalized by $\rho U_{ref}^2 c_m^3$. (g) Aerodynamic power consumptions, nondimensionalized by $\rho U_{ref}^3 c_m^2$. Blue: Training database. Red: Test database. Solid line represents the equality of prediction of simplified aerodynamic model and CFD results.

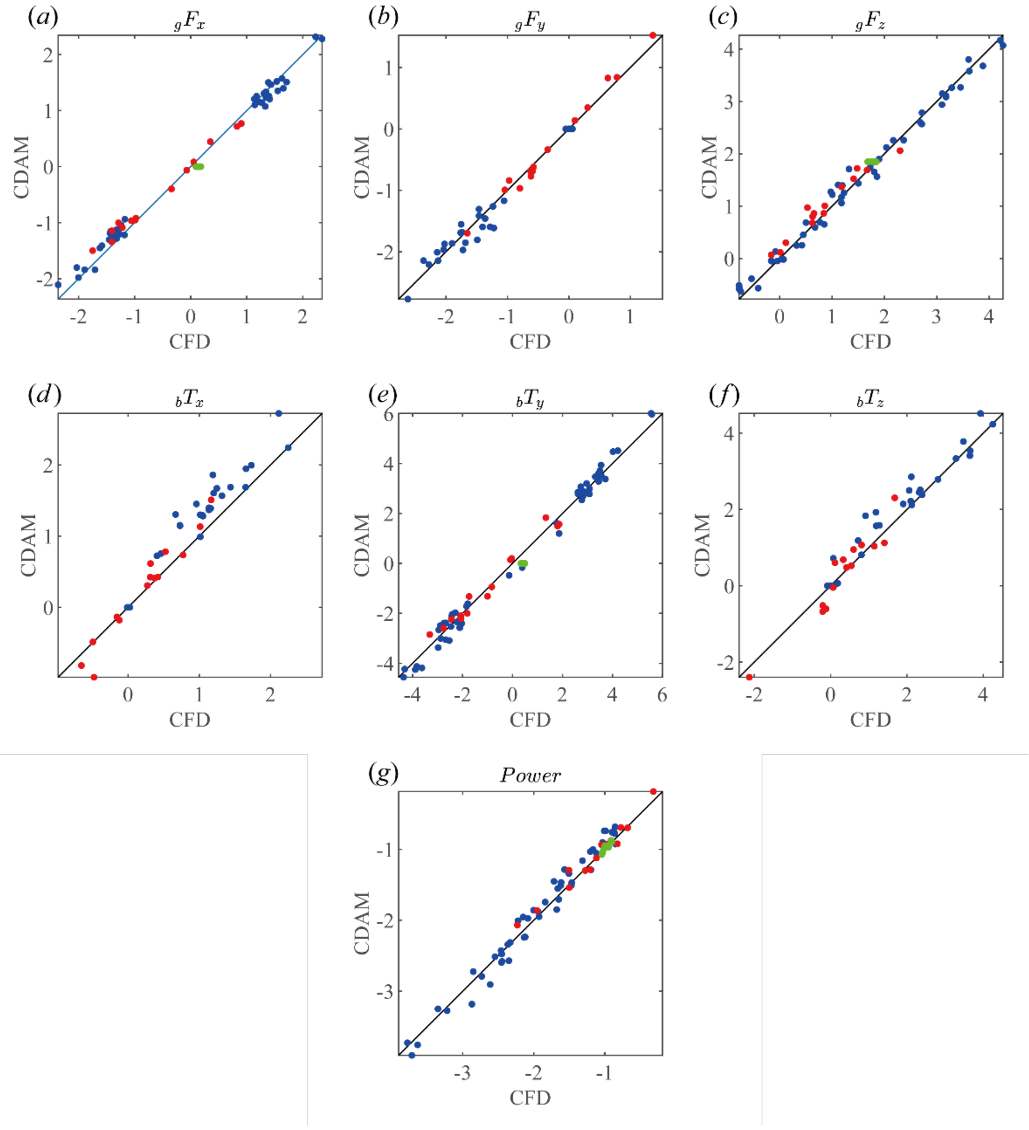

Figure 2.9 Comparison between prediction of CDAM and CFD database for bumblebee. (*a*-*c*) Aerodynamic forces in ground frame, nondimensionalized by $\rho U_{ref}^2 c_m^2$. (*d*-*f*) Aerodynamic torques with respect to center of body mass of modeled bumblebee in body-fixed frame, nondimensionalized by $\rho U_{ref}^2 c_m^3$ (g) Aerodynamic power consumptions, nondimensionalized by $\rho U_{ref}^3 c_m^2$. Blue: Training database. Red: Test database. Green: Trim states listed in Table 2.6. Solid line represents the equality of prediction of quasi-steady model and CFD results.

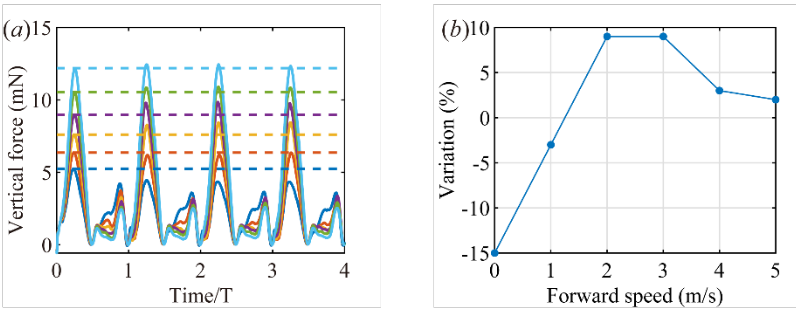

Figure 2.10 (*a*) Time course of the vertical force with the corresponding colored dashed lines representing the peak value of the downstroke in the first stroke cycle from bottom up: hovering (0 m/s) and forward speed 1 m/s, 2 m/s, 3 m/s, 4 m/s and 5 m/s. (*b*) Difference of the peak value of vertical force in downstroke between first and second stroke cycle.

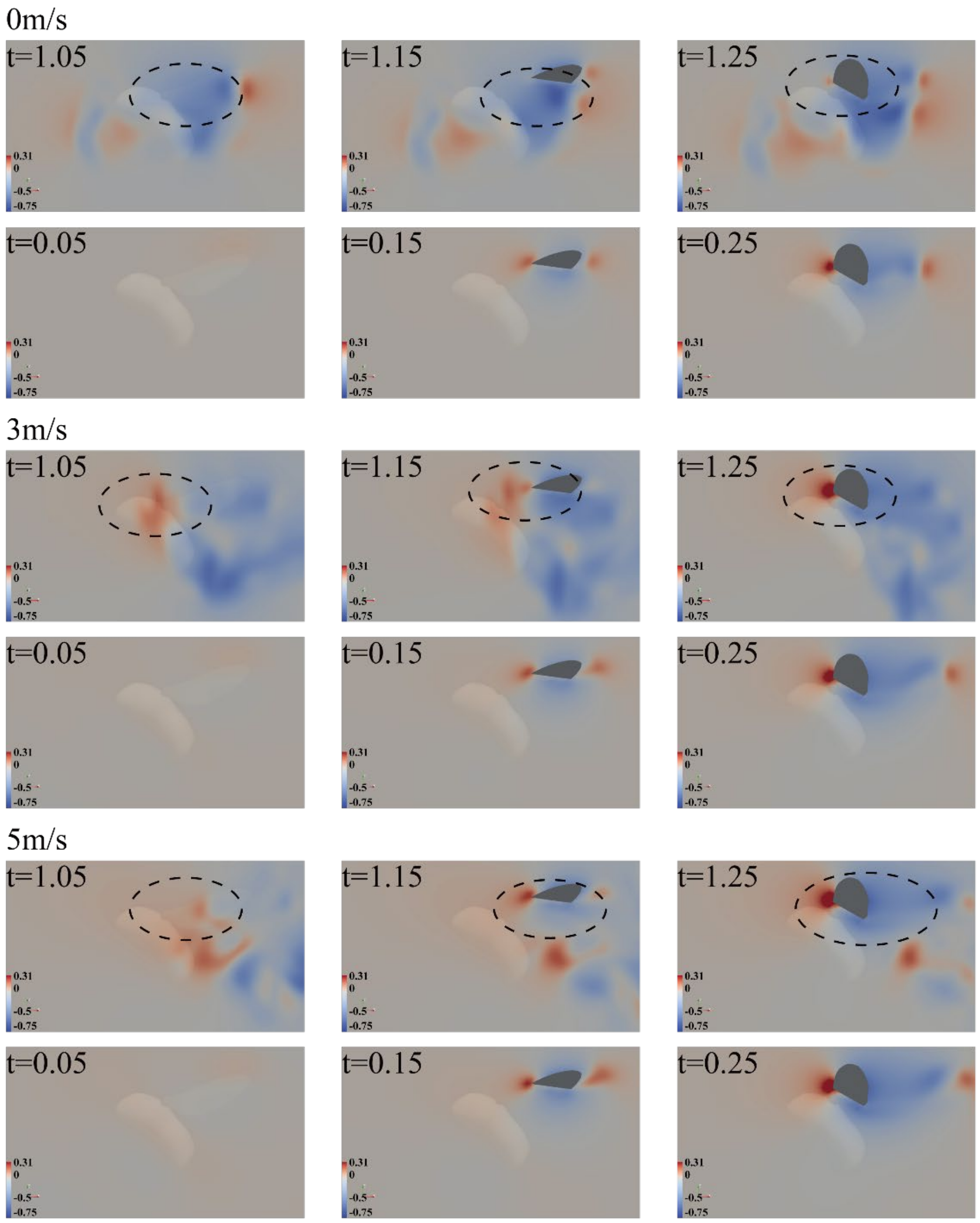

Figure 2.11 The vertical flow velocity nondimensionalized by U_{ref} of the air flow on the vertical cut plane 2 cm away from the sagittal plane of bumblebee for hovering, forward speed 3 m/s and 5 m/s in the first and second stroke cycle. Red indicates the air flowing upward and blue indicates the air flowing downward.

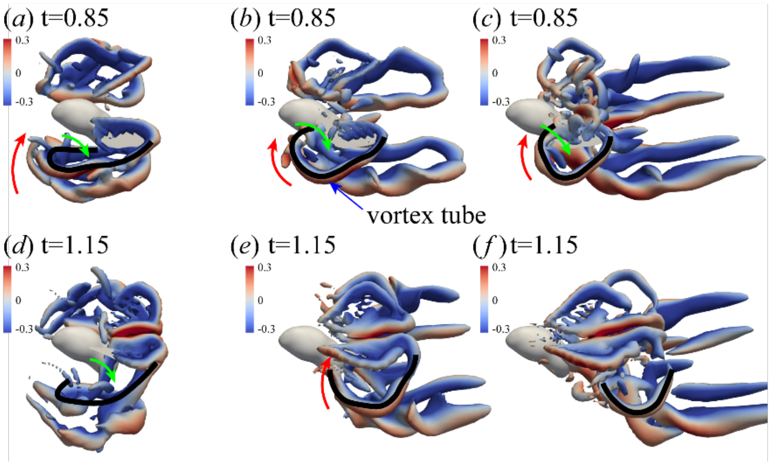

Figure 2.12 Vortical structures around flying bumblebee (isosurface with Q=0.1, colored by vertical velocity nondimensionalized by U_{ref}). (*a*) and (*d*) Hovering; (*b*) and (*e*) Forward speed 3m/s; (*c*) and (*f*) Forward speed 5m/s. Red arrows: upward flow; green arrows: downward flow. Black curve: vortex tube.

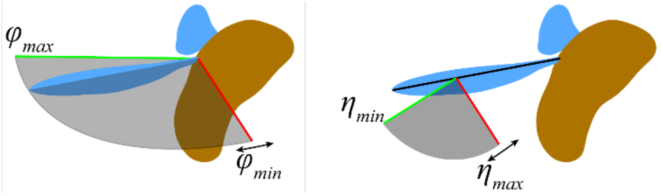

Figure 2.13 Sketch of the extrema of wing kinematics. Left: Positional angle. Right: Feathering angle.

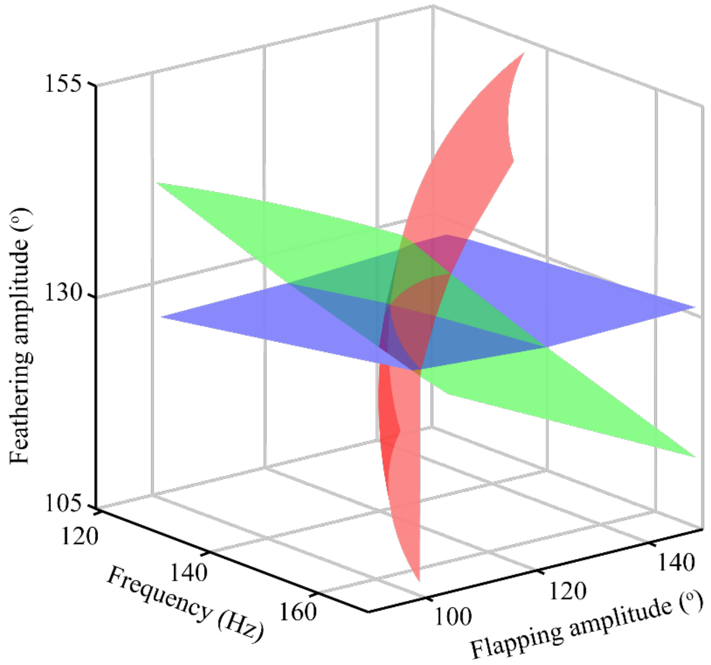

Figure 2.14 Isosurface, $_{g}\bar{F}_x = 0$ (blue), $_{g}\bar{F}_z = W$ (red) and $_{b}\bar{T}_y = 0$ (green) in the space spanned by the feathering amplitude, frequency and flapping amplitude.

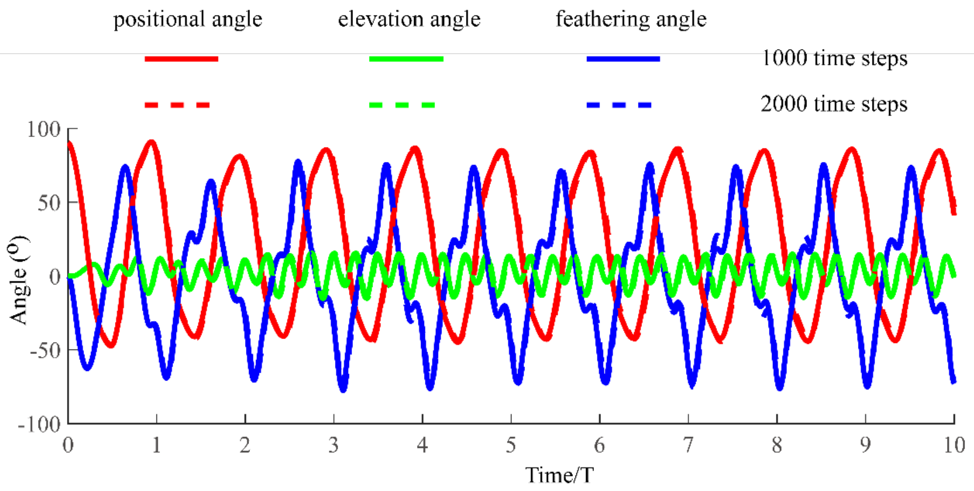

Figure 2.15 Time step independence test.

Kolomenskiy, D., Ravi, S., Xu, R., Ueyama, K., Jakobi, T., Engels, T., Nakata, T., Sesterhenn, J., Schneider, K., Onishi, R., Liu, H., The Dynamics of Passive Feathering Rotation in Hovering Flight of Bumblebees, Journal of Fluids and Structures, Vol. 91, No. (2019),pp. 102628.

Lophaven, S. N., Nielsen, H. B., Sondergaard, J., Dace, A., A Matlab Kriging Toolbox, Technical University of Denmark Report IMM-TR-2002-12, Vol. (2002),pp.

Usherwood, J. R., Ellington, C. P., The Aerodynamics of Revolving Wings Ii. Propeller Force Coefficients from Mayfly to Quail, Journal of Experimental Biology, Vol. 205, No. 11 (2002),pp. 1565-1576.

List of tables

Table 2.1 The values of the morphology parameters of the bumblebee *Bombus ignitus*.

m_b	390.99 mg
m_w	0.76 mg
$I_{w,xx}$	4.1×10^{-11} kgm^2
$I_{w,yy}$	1.3×10^{-12} kgm^2
$I_{w,xy}$	-2×10^{-12} kgm^2
$I_{w,zz}$	4.2×10^{-11} kgm^2
$I_{b,xx}$	2.2×10^{-9} kgm^2
$I_{b,yy}$	7.5×10^{-9} kgm^2
$I_{b,zz}$	7.7×10^{-9} kgm^2
R	15.2 mm
L	16.3 mm
${}_bR_h$	$(-6.8,2.6,2.6)'$ mm
${}_wR_{wg}$	$(0.9,8.0,0)'$ mm
c_m	4.1 mm
f	139 Hz
U_{ref}	10.05 m/s

Table 2.2 Adopted flight velocities of modeled bumblebee for training data set.

#	Forward/backward (U_{ref})	Lateral (U_{ref})	Vertical (U_{ref})
1	-0.4	0	0
2	-0.4	0	0.4
3	-0.4	0.4	0
4	-0.4	-0.4	0
5	-0.4	0.4	0.4
6	-0.4	-0.4	0.4
7	0.4	0	0
8	0.4	0	0.4
9	0.4	0.4	0
10	0.4	-0.4	0
11	0.4	0.4	0.4
12	0.4	-0.4	0.4

Table 2.3 Adopted wing kinematics of modeled bumblebee for training data set. The row numbers are corresponding to those in Table 2.2.

#	wing kinematics						
1	120Hz 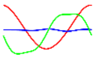	150Hz 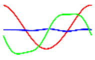	136Hz 	136Hz 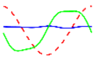	136Hz 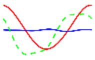	136Hz 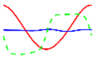	
2	120Hz 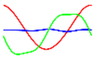	150Hz 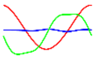	136Hz 	136Hz 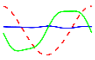	136Hz 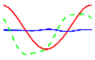	136Hz 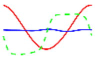	136Hz 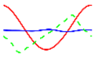
3	120Hz 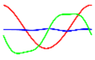	150Hz 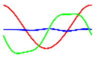	136Hz 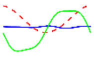	136Hz 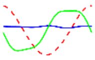	136Hz 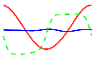		
4	120Hz 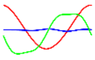	150Hz 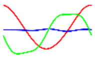	136Hz 	136Hz 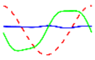	136Hz 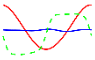		
5	120Hz 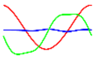	150Hz 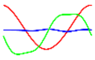	136Hz 	136Hz 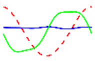	136Hz 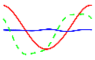	136Hz 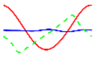	
6	120Hz 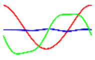	150Hz 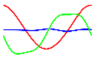	136Hz 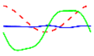	136Hz 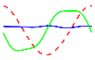	136Hz 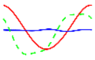	136Hz 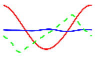	
7	120Hz 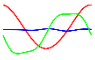	150Hz 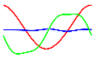	136Hz 	136Hz 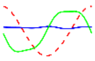	136Hz 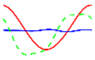	136Hz 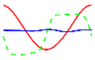	
8	120Hz 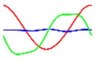	150Hz 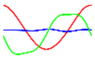	136Hz 	136Hz 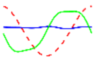	136Hz 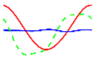	136Hz 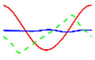	136Hz 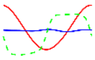
9	120Hz 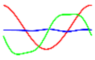	150Hz 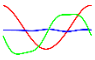	136Hz 	136Hz 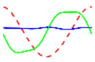	136Hz 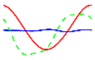	136Hz 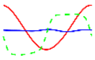	
10	120Hz 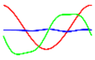	150Hz 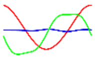	136Hz 	136Hz 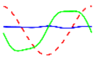	136Hz 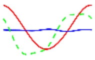	136Hz 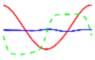	
11	120Hz 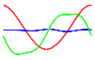	150Hz 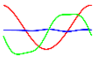	136Hz 	136Hz 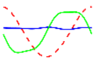	136Hz 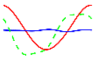	136Hz 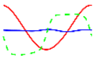	
12	120Hz 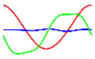	150Hz 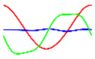	136Hz 	136Hz 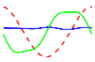	136Hz 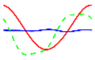	136Hz 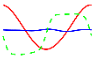	

Table 2.4 Adopted flight velocities and wing kinematics of modeled bumblebee for test data set.

#	Forward/backward (U_{ref})	Lateral (U_{ref})	Vertical (U_{ref})	frequency (Hz)	wing kinematics
1	0.252	-0.286	0.282	147	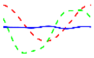
2	0.325	-0.062	0.012	123	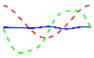
3	-0.298	0.332	0.11	147	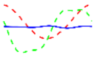
4	0.33	0.233	0.018	138	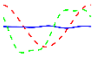
5	0.105	0.367	0.038	122	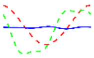
6	-0.177	-0.371	0.277	136	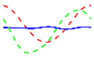
7	0.037	0.279	0.126	148	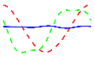
8	0.366	0.347	0.38	148	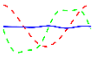
9	0.371	0.142	0.013	124	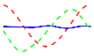
10	-0.273	0.206	0.175	149	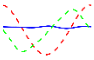
11	0.376	0.194	0.152	148	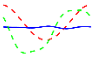
12	0.365	-0.086	0.306	134	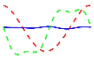
13	-0.011	0.124	0.318	144	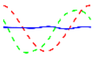
14	0.24	-0.263	0.074	124	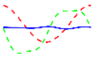
15	-0.321	0.124	0.329	128	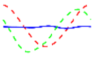

Table 2.5 Fitted coefficients of the simplified aerodynamic model for a moving body of Bumblebee.

$C_{bd,L}$	$C_{bd,D}(0)$	$C_{bd,D}\left(\frac{\pi}{2}\right)$	x_p	z_p
0.0701	0.0465	0.1604	-0.3118	-0.0081

Table 2.6 Trim states of a flying bumblebee with forward speed 1.005 m/s.

#	Body angle (deg.)	Stroke plane angle (deg.)	Frequency (Hz)	Flapping amplitude (deg.)	Feathering amplitude (deg.)
1	45	0	123	135	114
2	45	5	127	132	121
3	45	10	132	130	129
4	40	0	130	127	114
5	40	5	134	124	122
6	40	10	140	122	129
7	35	0	137	120	115
8	35	5	142	117	122
9	35	10	149	114	130
10	25	0	153	106	116
11	15	0	171	94	118

Chapter 3

3 Effects of wing hinge flexibility

3.1 Introduction

Flying insects display diverse but robust flapping flights while achieving complex maneuvering under various natural environments. Through integration of active muscle-driven rotational wing dynamics and passive reaction of various flexible structures including wings, exoskeletal elements, wing hinges, and musculoskeletal elements (Walker, Schwyn *et al.* 2014; Liu, Ravi *et al.* 2016; Liu 2020), they could take advantages of passive and active mechanisms (PAM), that actuate, coordinate and control flapping wings, and to robustly simplify the control of flapping flight while minimizing the high energetic cost by using elastic storage through elastic flight muscles and motors. Such PAM-based control strategy could offer morphological and mechanical intelligence in flapping flights without active sensory input and precise motor control. Although recent advances in insect flight biomechanics have addressed how flapping wings produce aerodynamic forces (Ellington, van den Berg *et al.* 1996; Liu and Kawachi 1998; Sane 2003; Liu 2009; Ishihara 2018) and achieve flight control (Bergou, Ristroph *et al.* 2010; Ristroph, Bergou *et al.* 2010; Ma, Chirarattananon *et al.* 2013; Beatus, Guckenheimer *et al.* 2015; Whitehead, Beatus *et al.* 2015; Yao and Yeo 2019), unraveling how the flapping-wing dynamics are created in a diverse but robust way and how the PAM strategies work remains untouched and a challenge (Liu, Ravi *et al.* 2016; Liu 2020). Here we develop a fluid-structure interaction (FSI) model that couples unsteady flapping aerodynamics and torsional-spring-based elastic wing-hinge dynamics in bumblebee hovering. We propose a PAM strategy of active-controlled stroke, passive-controlled wing pitch and deviation to determine how it dominates flapping-wing dynamics and correlates with optimal elastic storage.

3.2 Flexibility of the wing hinge in bumblebee

We select hovering flights of 4 individual bumblebees captured with high-speed cinematography (Kolomenskiy, Ravi *et al.* 2019). 8 sets of wing kinematics comprising four pairs of right and left wings (BB1R-4R, BB1L-4L) are expressed in Fourier series (Figure 3.1). Taking an average wing length of 15.2 mm of the 4 individuals, we calculate the wing mass based on scaling, which is proportional to the cube of wing length (Kolomenskiy, Ravi *et al.* 2019) and is 0.76 mg, corresponding to the moments of inertia: $I_{xx} = 4.1 \times 10^{-11} kgm^2$, $I_{yy} = 1.3 \times 10^{-12} kgm^2$, $I_{xy} = -2.0 \times 10^{-12} kgm^2$. While minor inter-individual discrepancies are observed in the three angles of wing motions, wing deviation (elevation angle) presents large variations at upstroke (Figure 3.2) while small at downstroke, indicating that the steering muscle may execute some active control on the upstroke wing motion while being switched off at downstroke allowing passive reaction owing to the elastic elements, as observed in blowflies (Balint and Dickinson 2001).

We then estimate the flexibility of the wing hinge by the simulating the interaction between the wing and body via the simulation-based framework presented in Chapter 2. We then develop a flapping-wing dynamic model by introducing an elastic wing hinge model, namely, Three-Torsional-Spring-Wing-Hinge Model (TTSWHM), which utilizes three torsional springs to mimic 3 DoFs (degree of freedom) wing motions.

Wing stroke in bumblebee is powered by asynchronous muscles characterized by a delayed stretch activation, which enables asynchronous muscles to output power over an entire stretch-hold-release-hold cycle (Josephson, Malamud *et al.* 2000; Deora, Gundiah *et al.* 2017). This is also observed here as shown in Figure 3.3*a*, of a rapid change in stroke torque (T_φ) at the extremum of positional angles, consistent with the delayed stress in figure 6C by Josephson, Malamud *et al.* (2000). An actively driven torsional spring is herein employed as,

$$T_\varphi = -K_\varphi(\varphi - \varphi_0) + sgn(\dot{\varphi})d \tag{3.1}$$

where K_φ ($= 3.28 \pm 0.13 \times 10^{-5} Nm$) denotes the flapping-spring stiffness, $\varphi_0 (= 16.8 \pm 4.6°)$ the offset positional angle, $d (= 1.89 \pm 0.22 \times 10^{-5} Nm)$ the power strength from delayed stretch activation fitted from measurements (Figure 3.3*a*), and *sgn*(·) the sign of variables, respectively. Stroke torques via positional angles are observed well fitted with the active-controlled wing stroke model.

Wing pitch is observed to have a specifical correlation between pitch torque (T_η) and feathering angle at $\eta < 45$ deg, featured with an elliptical curve and a negative major axis (Figure 3.3*b*), and thus is modeled with a passively driven torsional spring with damping effect (Bergou, Ristroph *et al.* 2010),

$$T_\eta = -k_\eta(\eta - \eta_0) - C_\eta \dot{\eta} \tag{3.2}$$

where $k_\eta (= 5.27 \pm 0.48 \times 10^{-6} Nm)$ denotes the feathering-spring stiffness, $\eta_0 (= 1.7 \pm 5.04°)$ the offset feathering angle, and $C_\eta (= 8.51 \pm 2.09 \times 10^{-10} Nms)$ the damping fitted from measurements (Figure 3.3*b*). Note that the pitch torque turns to reduce rapidly when feathering angle is greater than 45 deg. We infer that bumblebees turn to keep the feathering angle high enough while sustaining a low angle of attack, to avoid large horizontal drag and hence excessive power output at mid-stroke probably through reducing the pitch torque (Figure 3.3*b*).

Because wing deviation is a result of interplay between active steering muscle and elastic wing hinge (Walker, Schwyn *et al.* 2014), deviation torque vs elevation angle displays a much more complicated nature (Figure 3.3*c*). With consideration of the similarity with the flapping-wing dynamics in blowfly *Calliphora vicina* by Balint et al (Balint and Dickinson 2001), that the downstroke deviation is controlled in part via the mechanical summation of basalare activities and its spiking time is strongly correlated with the deviation to achieve desired wing trajectories by resisting against aerodynamic loads, we herein propose a minimal model to determine the passive elevation rotation-induced dynamics in bumblebee hovering. The deviation torque (T_θ) is modeled with a passively driven torsional spring-induced torque, along with damping effect and a time-varying torque accounting for the muscle spiking timing, such as:

$$T_\theta = -k_\theta \theta - c\dot{\theta} + T_b \tag{3.3}$$

where $k_\theta (= 1.16 \times 10^{-4} Nm)$ is the elevation-spring stiffness, c is the damping coefficient associated with the active steering, and T_b is the time varying torque. The dynamic model of elevation-rotation can then be obtained,

$$\begin{aligned} I\ddot{\theta} &= -k_\theta \theta - c_1 \dot{\theta} + T_b + T_a \qquad & t < \ t_s \, or \, t > t_p, \\ I\ddot{\theta} &= -k_\theta \theta - c_2 \dot{\theta} + T_b + T_a \qquad & t_s \le t \le t_p \end{aligned} \tag{3.4}$$

where two different damping coefficients ($c_1 = 1.33 \times 10^{-8} Nms$, $c_2 = -0.63 \times 10^{-8} Nms$) are introduced for two distinct stages in a stroke period with $t_s = 0.43T$, $t_p = 0.97T$. T_a is the aerodynamic torque while sum ($T_b + T_a$) of active steering torque and aerodynamic torque is approximated in a manner of piecewise constants (Figure 3.3*e*), equals to $1.05 \times 10^{-5} Nm$ at $t_s \le t \le t_p$, and $1.72 \times 10^{-5} Nm$ at $t < \ t_s \, or \, t > t_p$, respectively. Here a genetic algorithm (Hansen and Kern 2004) is employed to determine the parameters $[k_\theta, c_1, c_2, T_b + T_a, t_s, t_p]$ through data fitting. The minimal model (equation (3.4)) enables a reasonable modeling of elevation rotation (Figure 3.2) while the whole wing deviation torque estimated is well consistent with measurements (Figure 3.3*d*). Interestingly, it is seen that the elevation-spring stiffness k_θ is solely several dozen times of the feathering-spring stiffness, and itself cannot produce a passive elevation-rotation-induced torque large enough to resist the aerodynamic torque to sustain a small elevation amplitude (Qin, Cheng *et al.* 2014) (Figure 3.1*b*, Figure 3.3*c*). We infer that the integration of the passive wing hinge-driven control and the active steering control in concern with wing deviation in bumblebee hovering may enable somehow "*apparently stiff*" wing hinge to achieve the small elevation amplitude while high flapping performance. While this likely results in complexities between deviation torque and elevation angle, the underlying mechanism associated with the elevation-rotation control can be modeled reasonably through a torsional spring with a step-function offset position (Figure 3.3*d*). With a starting point of $-\mathrm{A}_0$ with $-\mathrm{x}_0$, x_0 as two candidate offset positions, the elevation rotation, through some adjustment of the switching timing of offset position, can approach an appropriate position in-between $-\mathrm{A}_0 - 4\mathrm{x}_0$ and $-\mathrm{A}_0 + 4\mathrm{x}_0$ in a wing stroke. This indicates that the wing deviation presents a cumulative behavior in a manner of cycle-to-cycle step (Balint and Dickinson 2001).

We further investigate the energetic cost owing to elastic storage that elastic wing hinge can store excessive inertial power at wing deceleration while recovering the energy at wing acceleration (Walker, Schwyn *et al.* 2014), by comparing the power consumption between flexible and rigid wing hinges in bumblebee hovering. The total mean power is calculated to be $0.0155 \pm 0.0026W$ for the rigid wing hinge model but is remarkedly reduced to $0.0135 \pm 0.0025W$ in the elastic wing hinge model defined with equations (3.1), (3.2), (3.3). Obviously, the elastic storage is achieved with the energetic cost improved remarkedly by 13% (Figure 3.4), well consistent with the measurements of an approximately 10% reduction in fruit fly hovering in terms of the energetic cost minimization (Dickinson and Lighton 1995).

3.3 Aerodynamics of passive feathering and elevation

We further explore how the elastic storage enables robustness of flapping-wing dynamics and aerodynamics in terms of elevation-spring stiffness, i.e., a quantitative effect of the "apparently stiff" wing hinge on the achievement of small elevation amplitude while high flapping performance (Dickinson and Lighton 1995). The torsional spring wing hinge model is hereby proposed with the elevation-rotation simply modelled with a single torsional spring with sufficiently large elevation-spring stiffness.

Natural frequency of a flapping dynamic system plays a crucial role in force production and energetic optimization, showing specific correlations with flapping frequency as reported in flexible wings (Kang, Aono *et al.* 2011) and wings with passive pitching (Spagnolie, Moret *et al.* 2010). We first examine natural frequencies of wing deviation and pitch in vacuum without aerodynamic drag, and in air with interaction between flapping dynamics and aerodynamics, to examine the correlations between dynamic characteristics and elevation-and feathering-spring stiffness (k_θ, k_η). Discrete Fast Fourier Transformation is applied to analyze the frequency spectrum of wing motions. The dominant frequencies of wing deviation in vacuum with various feathering-spring stiffnesses [blue circles] and in air with a feathering-spring stiffness (k_0) [red squares] (Figure 3.5*a*) are observed proportional to a square root of the elevation-spring stiffness, with a proportionality coefficient, $\frac{1}{2\pi\sqrt{I_{zz}}}$, where I_{zz} denotes the MoI of wing deviation. This indicates that the wing pitch hardly impacts wing deviation and hence the passive elevation-rotation is essentially of a robust flapping dynamics-based system. In contrast, the dominant frequencies of wing pitch (Figure 3.5*b*) display a significantly diverged feature: the dominant frequencies (red squares) in air are independent of both feathering-and elevation-spring stiffness, implying that the passive feathering-rotation is likely of a flapping aerodynamics-dominant system. Furthermore, the dominant frequencies (blue circles) in vacuum do not obey a consistent proportionality while showing dependency on elevation-spring stiffness (blue circles enclosed by dashed red curve in Figure 3.5*b*). We examine the dynamic characteristics of these blue circles in vacuum and find a linear relation of $f_\eta = f_\theta + 1$ (dashed blue line) in frequency spectrum (Figure 3.5*c*) between dominant frequency (wing pitch) and natural frequency (wing deviation).

We further beg a question: whether the passive wing deviation and pitch enable robustness of flapping aerodynamic performance. We investigate the elevation-spring stiffness dependency in terms of elevation and feathering amplitudes, vertical force and power efficiency, over a broad range of elevation-spring stiffness (Figure 3.6) at a specific feathering-spring stiffness (k_0) (Kolomenskiy, Ravi *et al.* 2019).

The elevation amplitude shows a trend decreasing with increasing elevation-spring stiffness but distinguished features in three domains (Figure 3.6*a*): a steep-drop in Domain I; a U-shape with two peaks at borders ($90k_0, 190k_0$) in domain II; and a gradual-damping in domain III. The frequency spectrum (Figure 3.6*e*) reveals specific relationship between natural and driving frequencies at $k_\theta = 90k_0$ or $k_\theta = 190k_0$, where the natural frequency equals the driving frequency of $3f_{flap}$ or $4f_{flap}$, and the resonance is observed to amplify the elevation amplitude. Over a broad range of elevation-spring stiffness ($k_\theta > 90k_0$), the elevation amplitude keeps a low level substantially dropping within the range of measurements (red region) (Figure 3.6*a*). Correspondingly, the feathering amplitude also displays variations in three domains (Figure 3.6*b*): a steep-drop in domain I; a U-shape with two peaks at borders ($90\mathrm{k}_0, 190\mathrm{k}_0$) in domain II; and slight variation in domain III. Note that at most of the elevation-spring stiffness ($k_\theta > 90k_0$), except those at $k_\theta = 90\mathrm{k}_0$ or $k_\theta = 190\mathrm{k}_0$ where the resonance occurs, the feathering amplitudes are generated robustly within a narrow range of measurements (red region).

Robustness of the flapping-wing dynamics in concern with passive wing pitch and deviation owing to elastic wing hinge enables robustness of flapping-wing aerodynamics.

Large aerodynamic forces (Figure 3.6*c*) are observed being produced at most of the elevation-spring stiffness over the three domains, which well match the measurements (red region). Particularly, the vertical force displays a remarkable increase with increasing elevation-spring stiffness in domain II. The vertical force peaks and exceeds the weight of bumblebee by approximately 10% at an elevation-spring stiffness adjacent to $190k_0$. Variations in domain II show an upside-down U-shape with a steep-drop at $90k_0, 190k_0$, indicating that the resonance frequency diminishes aerodynamic force production. Power efficiency defined as $e = \frac{vertical\,force}{power}$ is further depicted in Figure 3.6*d*. A high level of power efficiency is observed, which is well consistent with that of previous study (Engels, Kolomenskiy *et al.* 2016), and shows remarked robustness to the elevation-spring stiffness except at $90k_0, 190k_0$, corresponding to the vertical forces (Figure 3.6*c*). The computed power efficiencies are noticeably lower compared to the experimental results, which is likely because of the difference in the measured and simulation-based feathering angles (Figure 3.1), *i.e.*, during the period that the feathering angle sustains a low angle of attack at mid-stroke. This discrepancy however does not affect the consistent conclusion reached here. We further investigate the dependency of elevation-spring stiffness on energetic cost owing to elastic storage at various elevation-spring stiffnesses. We find that compared to that of a rigid wing hinge model, the power consumption can be improved by 19% at $k_\theta = 190k_0$ comparable with our previous result (13%) (Figure 3.4) with the fine elastic wing hinge model but solely 4% at much larger $k_\theta = 1000k_0$. Thus, the elastic storage in concern with elastic wing hinge enables minimization of the energetic cost while robustness of the flapping-wing dynamics.

The proposed three-torsional-spring model demonstrates that the PAM strategy broadly adopted by insects can achieve robust flapping-wing dynamics integrated by a dynamics-based passive elevation rotation and an aerodynamic-based passive feathering rotation. Our findings further point to the importance of two mechanical design principles applicable for flapping-wing micro air vehicles (FMAVs): extremely large elevation-spring stiffness while extremely small wing deviation can generate aerodynamic force enough to sustain flyers stay airborne (Liu, Ravi *et al.* 2016; Liu 2020); and adjustment of elevation-spring stiffness (e.g., in domain II) can achieve optimal aerodynamic performance. For example, an optimal design associated with vertical force production and power efficiency can be implemented at $k_\theta = 190k_0$ (Figure 3.6*c* and *d*) with the natural frequency ($f_\theta = \frac{1}{2\pi}\sqrt{k_\theta / I_{zz}}$) equivalent to a driving frequency of $4f_{flap}$, which leads to specifying the elevation-spring stiffness to be $k_\theta^* = 64\pi^2 f_{flap}^2 I_{zz}$.

References

Balint, C. N., Dickinson, M. H., The Correlation between Wing Kinematics and Steering Muscle Activity in the Blowfly Calliphora Vicina, Journal of Experimental Biology, Vol. 204, No. 24 (2001),pp. 4213.

Beatus, T., Guckenheimer, J. M., Cohen, I., Controlling Roll Perturbations in Fruit Flies, Journal of the Royal Society Interface, Vol. 12, No. 105 (2015),pp. 20150075.

Bergou, A. J., Ristroph, L., Guckenheimer, J., Cohen, I., Wang, Z. J., Fruit Flies Modulate Passive Wing Pitching to Generate in-Flight Turns, Physical Review Letters, Vol. 104, No. 14 (2010),pp. 148101.

Deora, T., Gundiah, N., Sane, S. P., Mechanics of the Thorax in Flies, Journal of Experimental Biology, Vol. 220, No. 8 (2017),pp. 1382.

Dickinson, M. H., Lighton, J. R., Muscle Efficiency and Elastic Storage in the Flight Motor of Drosophila, Science, Vol. 268, No. 5207 (1995),pp. 87-90.

Ellington, C. P., van den Berg, C., Willmott, A. P., Thomas, A. L. R., Leading-Edge Vortices in Insect Flight, Nature, Vol. 384, No. 6610 (1996),pp. 626-630.

Engels, T., Kolomenskiy, D., Schneider, K., Lehmann, F. O., Sesterhenn, J., Bumblebee Flight in Heavy Turbulence, Physical Review Letters, Vol. 116, No. 2 (2016),pp. 028103.

Hansen, N., Kern, S. Evaluating the Cma Evolution Strategy on Multimodal Test Functions, Berlin, Heidelberg, Springer Berlin Heidelberg, 2004

Ishihara, D., Role of Fluid-Structure Interaction in Generating the Characteristic Tip Path of a Flapping Flexible Wing, Physical Review E, Vol. 98, No. 3 (2018),pp. 032411.

Josephson, R. K., Malamud, J. G., Stokes, D. R., Asynchronous Muscle: A Primer, Journal of Experimental Biology, Vol. 203, No. 18 (2000),pp. 2713.

Kang, C. K., Aono, H., Cesnik, C. E. S., Shyy, W., Effects of Flexibility on the Aerodynamic Performance of Flapping Wings, Journal of Fluid Mechanics, Vol. 689, No. (2011),pp. 32-74.

Kolomenskiy, D., Ravi, S., Xu, R., Ueyama, K., Jakobi, T., Engels, T., Nakata, T., Sesterhenn, J., Schneider, K., Onishi, R., Liu, H., The Dynamics of Passive Feathering Rotation in Hovering Flight of Bumblebees, Journal of Fluids and Structures, Vol. 91, No. (2019),pp. 102628.

Liu, H., Integrated Modeling of Insect Flight: From Morphology, Kinematics to Aerodynamics, Journal of Computational Physics, Vol. 228, No. 2 (2009),pp. 439-459.

Liu, H., Simulation-Based Insect-Inspired Flight Systems, Current Opinion in Insect Science, Vol. 42, No. (2020),pp. 105-109.

Liu, H., Kawachi, K., A Numerical Study of Insect Flight, Journal of Computational Physics, Vol. 146, No. 1 (1998),pp. 124-156.

Liu, H., Ravi, S., Kolomenskiy, D., Tanaka, H., Biomechanics and Biomimetics in Insect-

Inspired Flight Systems, Philosophical Transactions of the Royal Society B: Biological Sciences, Vol. 371, No. 1704 (2016),pp. 20150390.

Ma, K. Y., Chirarattananon, P., Fuller, S. B., Wood, R. J., Controlled Flight of a Biologically Inspired, Insect-Scale Robot, Science, Vol. 340, No. 6132 (2013),pp. 603.

Qin, Y., Cheng, B., Deng, X. Trajectory Optimization of Flapping Wings Modeled as a Three Degree-of-Freedoms Oscillation System. 2014 IEEE/RSJ International Conference on Intelligent Robots and Systems, 2014

Ristroph, L., Bergou, A. J., Ristroph, G., Coumes, K., Berman, G. J., Guckenheimer, J., Wang, Z. J., Cohen, I., Discovering the Flight Autostabilizer of Fruit Flies by Inducing Aerial Stumbles, Proceedings of the National Academy of Sciences, Vol. 107, No. 11 (2010),pp. 4820.

Sane, S. P., The Aerodynamics of Insect Flight, Journal of Experimental Biology, Vol. 206, No. 23 (2003),pp. 4191.

Spagnolie, S. E., Moret, L., Shelley, M. J., Zhang, J., Surprising Behaviors in Flapping Locomotion with Passive Pitching, Physics of Fluids, Vol. 22, No. 4 (2010),pp. 041903.

Walker, S. M., Schwyn, D. A., Mokso, R., Wicklein, M., Müller, T., Doube, M., Stampanoni, M., Krapp, H. G., Taylor, G. K., In Vivo Time-Resolved Microtomography Reveals the Mechanics of the Blowfly Flight Motor, PLoS Biology, Vol. 12, No. 3 (2014),pp. e1001823.

Whitehead, S. C., Beatus, T., Canale, L., Cohen, I., Pitch Perfect: How Fruit Flies Control Their Body Pitch Angle, Journal of Experimental Biology, Vol. 218, No. 21 (2015),pp. 3508.

Yao, J., Yeo, K. S., A Simplified Dynamic Model for Controlled Insect Hovering Flight and Control Stability Analysis, Bioinspiration & Biomimetics, Vol. 14, No. 5 (2019),pp. 056005.

List of figures

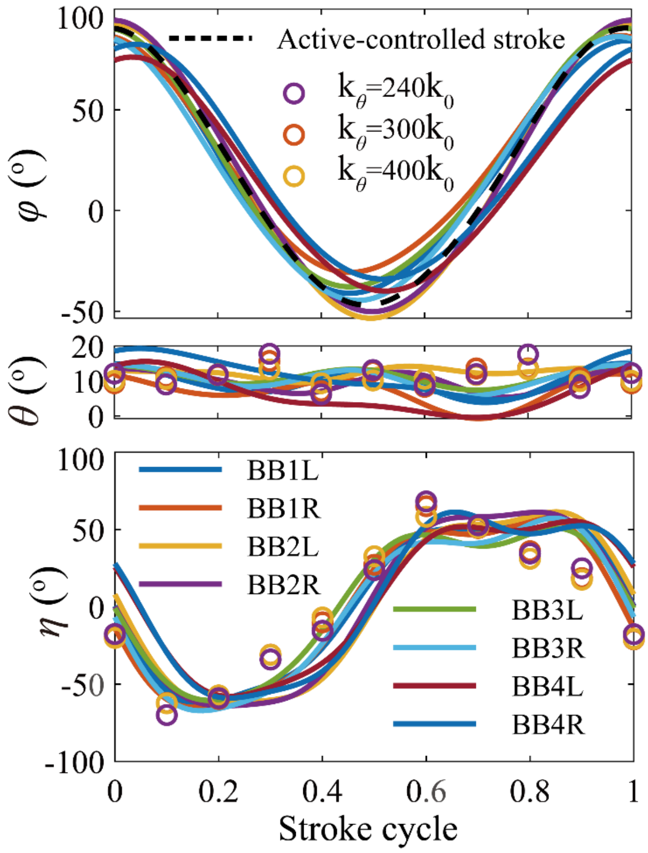

Figure 3.1 Wing kinematics of 4 individuals measured (solid lines) and elastic wing hinge model-based results (circles: at elevation-spring stiffnesses of 240, 300, 400 k_0, with feathering-spring stiffness, $k_0 = 2.61 \times 10^{-6} Nm$ (Kolomenskiy, Ravi *et al.* 2019)).

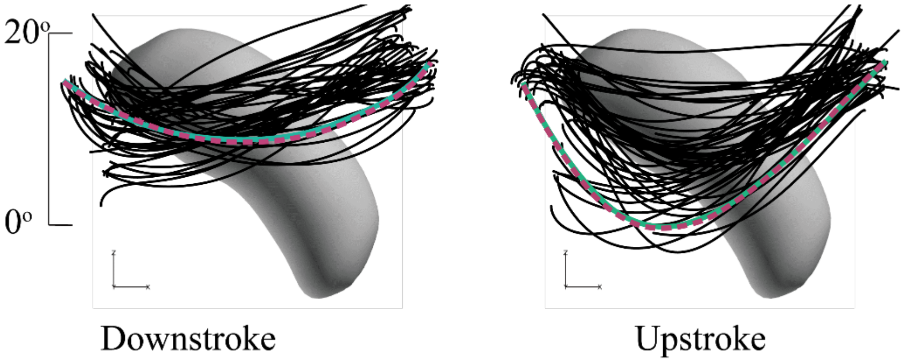

Figure 3.2 Wing deviations (elevation angle). Black lines: measurements; dark green lines: measurements (BB1R), dashed dark red lines: fitted with equation (4) (BB1R).

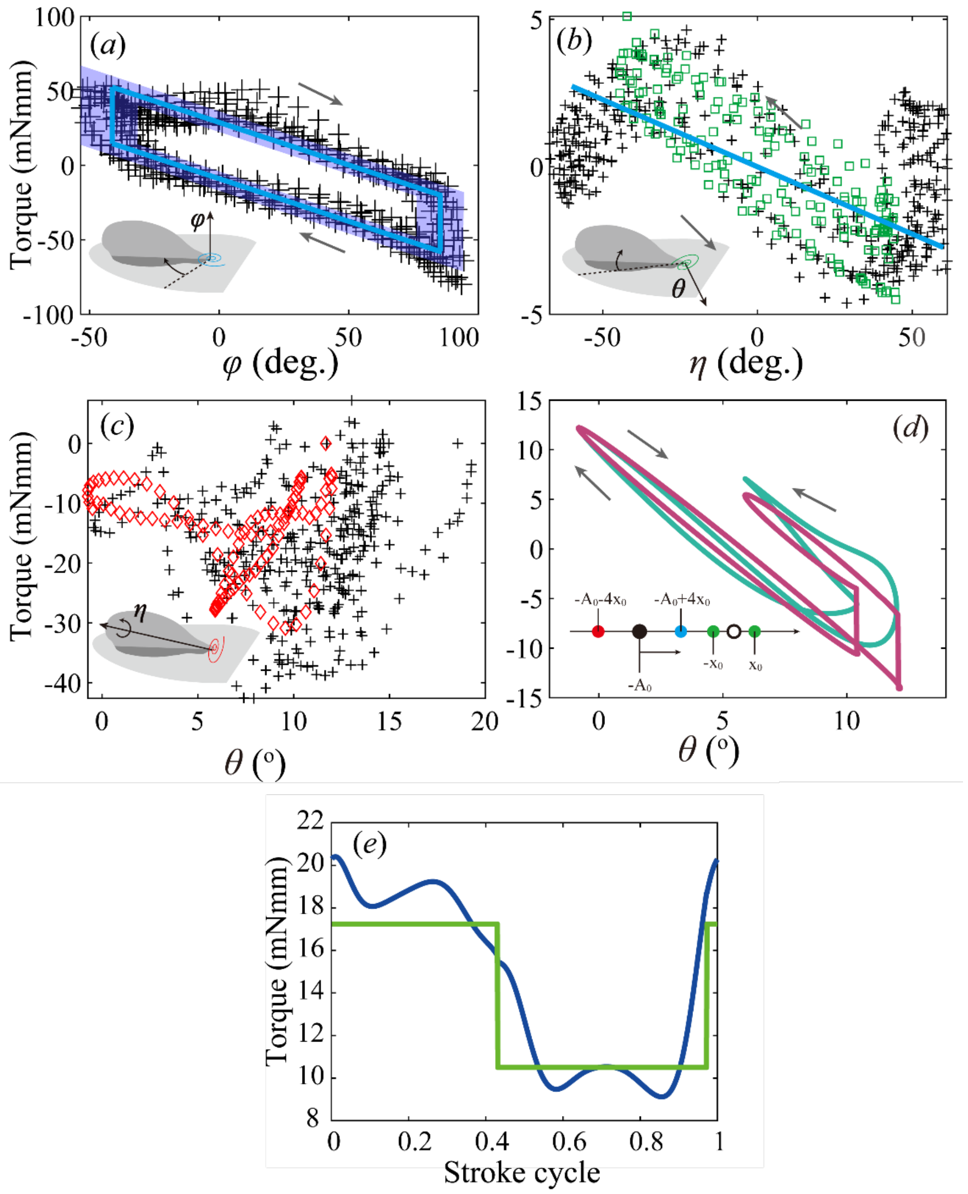

Figure 3.3 (*a*) Stroke torque (T_φ) vs positional angle (φ). Dark blue line: fitted with equation (3.1); shadowed region: standard deviation. (*b*) Pitch torque (T_η) vs feathering angle (η). Dark green square: fitted with equation (3.2) at η< 45 deg; dark blue line: fitted at k_0 without damping (Kolomenskiy, Ravi *et al.* 2019). (c) Deviation torque (T_θ) vs elevation angle (θ). Note that black crosses in (*a*), (*b*), (*c*) and Red diamonds in (*c*) respectively denote the torques based on flapping-wing aerodynamic simulations with wing kinematics prescribed from measurements of BB2R-4R & BB1L-4L and BB1R. (d) Whole wing deviation torque vs elevation angle (BB1R). Dark green line: measurement; dark red line: prediction with equation (3.4); Gray arrows: direction of time evolution. Inset: Cumulative characteristics of the elevation-spring with various offset positions. (*e*) Sum ($T_b + T_a$) of active control torque through wing hinge and aerodynamic torque. Blue line: measurement; green line: fitted with equation (3.4).

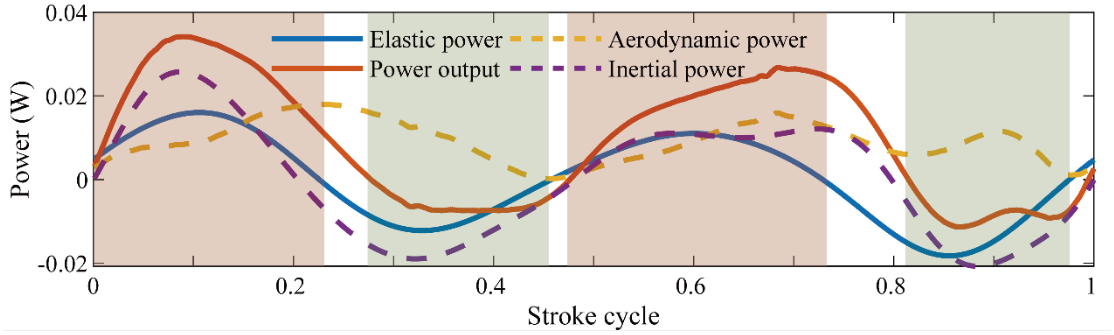

Figure 3.4 Elastic, aerodynamic and inertial powers in a wing stroke (BB1R). Pink region: energy recovery through elastic wing hinge to assist driving the wing at acceleration; green region: energy storage through elastic wing hinge to absorb excessive inertial power at deceleration.

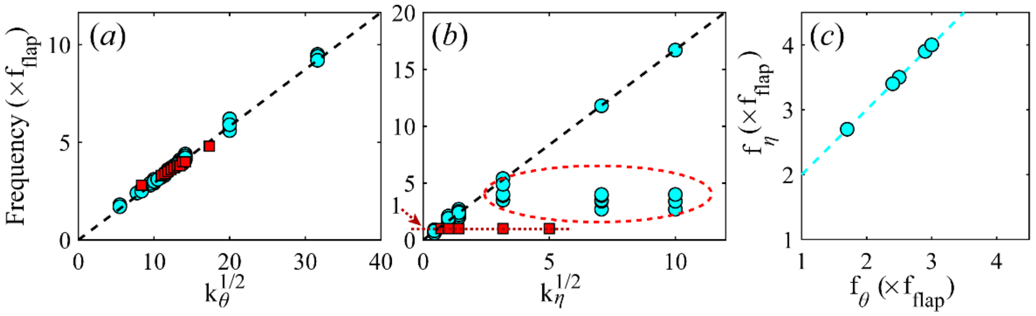

Figure 3.5 (a) Dominant frequency vs elevation-spring stiffness of wing deviation. Blue circles: in vacuum with various feathering-spring stiffnesses; dashed line: $f_\theta = \frac{1}{2\pi}\sqrt{k_\theta/I_{zz}}$, with I_{zz} as the MoI of wing deviation; red square: in air with feathering-spring stiffness of k_0. (b) Dominant frequency vs feathering-spring stiffness of wing pitch with various elevation-spring stiffnesses. Blue circle: in vacuum; dashed line: $f_\eta = \frac{1}{2\pi}\sqrt{k_\eta/I_{yy}}$, with I_{yy} as the MoI of wing pitch; red square: dominant frequency in air. (c) A linear relation ($f_\eta = f_\theta + 1$ (dashed blue line)) between dominant frequency (wing pitch) and natural frequency (wing deviation) of those (blue circles) enclosed by dashed red curve in (b).

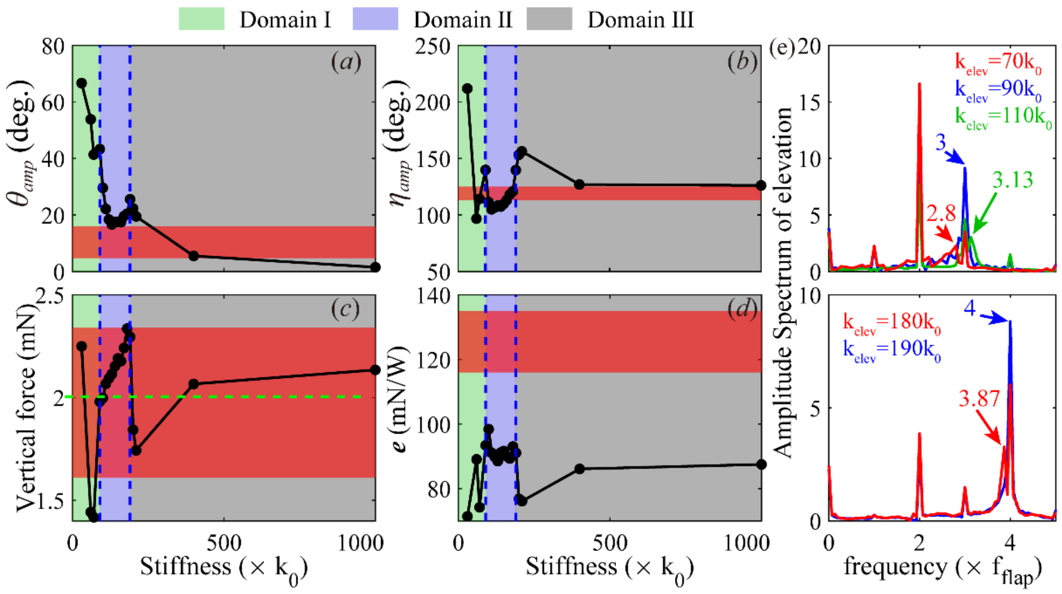

Figure 3.6 Elevation-spring stiffness (k_θ) dependency in terms of (*a*) wing elevation amplitude, (*b*) wing feathering amplitude, (*c*) mean vertical force, and (*d*) power efficiency. Domain I: $k_\theta \leq 90k_0$; domain II: $90k_0 \leq k_\theta \leq 190k_0$; domain III: $k_\theta \geq 190k_0$. Red region: a range covering all the measurements; dashed green line: a half weight of the bumblebee. (*e*) Amplitude spectrum of wing deviation in terms of natural frequency and driving frequency as integer multiples of flapping frequency $\left(f_{flap}, 2f_{flap}, 3f_{flap}, 4f_{flap} \dots\right)$ associated with elevation-spring stiffness.

Kolomenskiy, D., Ravi, S., Xu, R., Ueyama, K., Jakobi, T., Engels, T., Nakata, T., Sesterhenn, J., Schneider, K., Onishi, R., Liu, H., The Dynamics of Passive Feathering Rotation in Hovering Flight of Bumblebees, Journal of Fluids and Structures, Vol. 91, No. (2019),pp. 102628.

Chapter 4

4 Fast stabilization control

4.1 Introduction

Flapping wing insects normally fly at low Reynold number ($< 10^4$) (Shyy, Aono *et al.* 2013), in which the flows are unsteady and constantly changing. The unsteady external environment challenges the insects to maintain stable flight (Ortega-Jimenez, Greeter *et al.* 2013; Ravi, Kolomenskiy *et al.* 2016), let alone the maneuvers evading from predators or stimuli (Cheng, Deng *et al.* 2011; Muijres, Elzinga *et al.* 2014) and tracking interested targets (Matthews and Sponberg 2018; Zhang, Hedrick *et al.* 2019). Moreover, the small inertia renders the insects susceptible even to gentle unsteady currents, especially along the roll motion (Beatus, Guckenheimer *et al.* 2015). More importantly, prior work has found that flapping wing insects are dynamically unstable (Taylor and Thomas 2003; Sun and Xiong 2005; Sun, Wang *et al.* 2007; Xiong and Sun 2008) and will quickly lose the attitude without active feedback control. In addition, the insects only possess $10^5 \sim 10^6$ neurons of the brain, much less than small mammals (e.g. mouse: 7×10^7, humans: 10^{11}) (Kinoshita and Homberg 2017), which poses constraints to the development of efficient nervous system. Under such unfavourable conditions, it is surprising that the insects make it to fly with impressive stability and high maneuverability. The insects can correct the flight deviations within the time scale of only a few wing beats after disturbances (Ristroph, Bergou *et al.* 2010; Cheng, Deng *et al.* 2011; Beatus, Guckenheimer *et al.* 2015; Whitehead, Beatus *et al.* 2015), which outperforms any manmade air vehicles.

It is surprising that the flying insects predominantly adopt simple proportional-derivative (PD) control strategy as the active feedback control to stay stable against external disturbances (Ristroph, Bergou *et al.* 2010; Cheng, Deng *et al.* 2011; Beatus, Guckenheimer *et al.* 2015; Whitehead, Beatus *et al.* 2015), of which the derivative feedback is the rotational rate and the proportional feedback is the time integral of the derivative feedback. For a closed-loop system, the derivative gain and the proportional gain are the key parameters to determine the performance of a PD controller. Now, successful constructions of complete aerodynamic-dynamic models for flapping wing systems have allowed scientists to apply PD control on flying insects for stabilization control (Sun, Wang *et al.* 2007; Gao, Aono *et al.* 2009; Chang and Wang 2014; Bluman, Sridhar *et al.* 2018). Based on closed-loop simulation, it is demonstrated that the flight can be stabilized by the PD control with the time scale comparable with experimental measurements (Zhang and Liu 2018; Cai, Kolomenskiy *et al.* 2021). Intuitively, the insects have optimized these parameters after the long-time evolution and nature selection to achieve the stabilization control as fast as possible, however, which has been rarely studied yet.

The feedback delay and passive aerodynamic damping are the major factors that limit the stabilization. Feedback delay has disastrous implications for the stabilization performance (Elzinga, Dickson *et al.* 2012). Insects have evolved specialized mechanosensory structures to detect the body rotations such as the halteres of Diptera (Pringle and Gray 1948; Deora, Gundiah *et al.* 2017) and antennas of non-Dipteran insects including moths, butterflies and bees (Winston 1991; Sane, Dieudonné *et al.* 2007) to reduce the feedback delay, which, however, still exists in the active feedback control. Passive aerodynamic damping is an essential factor that characterize the dynamics of a flying insect, which is mainly generated by the morphology and kinematics of flapping wings. It has been reported that insects rely largely on the passive damping to stabilize the rotation (Hesselberg and Lehmann 2007; Hedrick, Cheng *et al.* 2009), which, however, is unable to correct the attitude deviation in open-loop dynamics. In closed-loop dynamics, the allowable reaction time is affected significantly by the aerodynamic damping (Ristroph, Ristroph *et al.* 2013). Therefore, the passive aerodynamic damping and time delay may affect the fastest rate achievable for an insect restoring to equilibrium after perturbation.

In this chapter, we aim to understand how insects achieve such fast stabilization with simple PD control with inevitable feedback delay and passive aerodynamic damping. A control-theoretic analysis method has been proposed by prior work (Cheng, Tobalske *et al.* 2016; Cai, Kolomenskiy *et al.* 2021) to identify the control parameters and consequently, the stabilization time. The closed-loop dynamics is transformed to complex domain from real-time domain by implementing Laplace transformation to obtain the transfer function and characteristic equation (Franklin, Powell *et al.* 2014). Root locus method is applied to illustrate the variation of poles, i.e. roots of the characteristic equation with the control parameters. Prior work believed fastest response is achieved once the closed-loop time constant is minimized (Cheng, Tobalske *et al.* 2016; Liu and Cheng 2017). However, we find that even faster stabilization is possible by introducing dynamic oscillatory mode (see Section 4.5.2). In addition, we find that small-sized fruit flies seem to achieve fast rotation stabilization by minimizing the restoring time (see Section 4.5.3), which can be generalized to other larger species of insects, even hummingbirds (see Section 4.5.4). We also give extensive discussions on such principle to minimize the restoring time with coupled dynamics of hawkmoth (see Section 4.6.2). Because the aerodynamic damping and time delay vary broadly among species (Figure 4.1), their effects on stabilization performance are also studied.

4.2 Flapping flight dynamics

Although time-resolved dynamical simulations, as proposed in Section 2.6, provide detailed motions of flying insects such as flapping-induced oscillations and effects of wing inertia (Yao and Yeo 2020; Cai, Kolomenskiy *et al.* 2021), simplified models are still necessary and practical to capture the main features of insect flight dynamics, of which linearized cycle-averaged dynamic models are most wildly implemented (Taylor and Thomas 2003; Sun, Wang *et al.* 2007; Cai, Kolomenskiy *et al.* 2021). Although the coupling between different axes of freedoms is inevitable, single-axis rotation dynamics is sufficient to assess fast rotation maneuver under the perturbations mainly in one direction (Ristroph, Bergou *et al.* 2010; Beatus, Guckenheimer *et al.* 2015). Under this condition, we take single-axis rotation dynamics of the insect as an example to illustrate the flight dynamics, which is governed by the following equation, simplified from the nonlinear dynamic equation proposed in Section 2.6, perturbed from hovering state (Bergou, Ristroph *et al.* 2010; Ristroph, Bergou *et al.* 2010)

$$I\ddot{\xi} = -c\dot{\xi} + \tau + \beta\Delta\Phi \tag{4.1}$$

where I is the inertia of the insect, c the aerodynamic effect due to the motion of the insect, which is usually a damping effect (Hedrick, Cheng *et al.* 2009), τ the effect from external perturbations such as magnet-induced torque which lasts a very short time (~5 ms) and is absent during the stabilization control (Ristroph, Bergou *et al.* 2010; Ristroph, Ristroph *et al.* 2013; Beatus, Guckenheimer *et al.* 2015). A deviation from hovering wing kinematics $\Delta\Phi$ can produce additional force and torque. For example, increasing stroke amplitude enhances the vertical force and offsetting the wing position produces a net pitching torque. β is the actuation coefficient correlating the changes of wing motion and aerodynamical consequences. ξ represents the state variable of the insect. It can be seen from equation (4.1) that the insect can control its flight by directly tuning the wing motions.

Flapping wing insects take advantage of proportional-derivative (PD) control strategy (Ristroph, Bergou *et al.* 2010; Cheng, Deng *et al.* 2011; Beatus, Guckenheimer *et al.* 2015) to stabilize the flight, i. e.,

$$\Delta\Phi(t) = -k_p\xi(t-\Delta t) - k_d\dot{\xi}(t-\Delta t) \tag{4.2}$$

where k_p and k_d are the proportional and derivative gains, respectively, Δt the time delay originating from sensing, signal transmission and information processing (Fayyazuddin and Dickinson 1996). The derivative feedback is directly sensed by the mechanosensory element, and the proportional feedback is the time integral of derivative feedback. Thus, the equation (4.1) takes the form

$$I\ddot{\xi}(t) = -c\dot{\xi}(t) + \tau - \beta k_p\left[\xi(t-\Delta t) + \frac{k_d}{k_p}\dot{\xi}(t-\Delta t)\right] \tag{4.3}$$

We define $\xi^+(t) \equiv \xi(t^+)$, $t^+ \equiv \frac{t}{T}$ to nondimensionalize equation (4.3). T is the stroke period. Let $c^+ \equiv \frac{cT}{I}$, $\tau^+ \equiv \frac{\tau T^2}{I}$, $k_p^+ \equiv \frac{\beta k_p T^2}{I}$, $\lambda^+ \equiv \frac{k_d}{Tk_p}$, thus

$$\ddot{\xi}^+(t^+) = -c^+\dot{\xi}^+(t^+) + \tau^+ - k_p^+\left[\xi^+(t^+ - \Delta t^+) + \lambda^+\dot{\xi}^+(t^+ - \Delta t^+)\right] \tag{4.4}$$

The proceeding equation depicts the closed-loop dynamics of flying insects. λ^+ is termed the controller time constant. The aerodynamic effect c^+ and time delay Δt^+ characterize the external dynamics and internal physiology of an insect which are determined (Figure 4.1), therefore, the stabilization control performance entirely relies on the control parameters k_p^+ and λ^+.

4.3 Closed-loop time constant

Previous work (Cheng, Tobalske *et al.* 2016; Liu and Cheng 2017; Cai, Kolomenskiy *et al.* 2021) applied Laplace transformation and root locus method to determine the fastest closed-loop time t_{CL}^+ by minimizing the real part of the poles of the characteristic equation, which represents the time spent to accelerate or decelerate to 63% peak velocity by following a step change in angular velocity (Liu and Cheng 2017), under the constraint that the real parts of all the poles are negative.

Here, we give a brief introduction to derive the closed-loop time. We first apply Laplace transformation to equation (4.4),

$$\Xi(s) = \frac{\dot{\xi}^+(0) + \left(s + c^+ + k_p^+\lambda^+e^{-\Delta t^+ s}\right)\xi^+(0) + \mathrm{T}}{s^2 + c^+s + k_p^+(1+\lambda^+s)e^{-\Delta t^+ s}} \tag{4.5}$$

where $\Xi(s) = \mathcal{L}[\xi^+(t^+)]$, $\mathrm{T} = \mathcal{L}[\tau]$ and $\mathcal{L}[\cdot]$ represents the Laplace transformation operator. The transfer function is

$$G(s) = \frac{1}{s^2 + c^+s + k_p^+(1+\lambda^+s)e^{-\Delta t^+ s}} \tag{4.6}$$

Hence, the dynamic response of the insect is characterized by the aerodynamic damping c^+, time delay Δt^+, the proportional gain k_p^+ and the controller time constant λ^+. Thus, one can obtain the characteristic equation

$$1 + k_p^+ \frac{(1 + \lambda^+ s)e^{-\Delta t^+ s}}{s^2 + c^+ s} = 0 \tag{4.7}$$

The second-order Padè approximation is applied to the term of time delay (Franklin, Powell *et al.* 2014)

$$e^{-\Delta t^+ s} \approx \frac{1 - \frac{\Delta t^+ s}{2} + \frac{(\Delta t^+ s)^2}{12}}{1 + \frac{\Delta t^+ s}{2} + \frac{(\Delta t^+ s)^2}{12}} \tag{4.8}$$

Thus, the characteristic equation is equivalent to a quartic equation with four roots. Given the λ^+, we can sweep k_p^+ from zero to infinity by implementing the root locus method to minimize the real parts of the poles, i. e. the roots of the characteristic equation. Root locus method is a graphical analysis that shows how the change of a parameter of a system affects the system's dynamic response. The method was first developed by Evans (1948) who gave rules for plotting the paths of the roots, a plot he called the Root Locus. We then can sweep λ^+ to obtain the minimal closed-loop time $t_{CL}^{+*}(c^+, \Delta t^+) = \min_{\lambda^+, k_p^+} 1/\left|R(p^d)\right|$, where p^d is the dominant pole (Cai, Kolomenskiy *et al.* 2021). Figure 4.2 illustrates the root locus with different controller time constants (Cai, Kolomenskiy *et al.* 2021).

It has been pointed out that when the control parameters are optimized, all the poles are real of which three are identical (Cai, Kolomenskiy *et al.* 2021), hence the characteristic equation (4.7) can be reformulated as with $\tilde{s} = s\Delta t^+$, $\tilde{k}_p^+ = k_p^+ \Delta t^{+2}$ $\tilde{k}_d^+ = k_d^+ \Delta t^+$

$$(\tilde{s} - \tilde{s}_1)(\tilde{s} - \tilde{s}_2)^3 = 0 \tag{4.9}$$

where $\tilde{s}_2$ is the dominant pole and $\tilde{s}_1$ is much smaller than $\tilde{s}_2$. By comparing the coefficients of equations (4.7) and (4.9) with method of undetermined coefficients (Descartes 1637), one can obtain following equation set

$$\begin{gathered} 6 + \tilde{k}_d^{+*} + c^+ \Delta t^+ = \tilde{s}_1 + 3\tilde{s}_2 \\ 12 + \tilde{k}_p^{+*} - 6\tilde{k}_d^{+*} + 6c^+ \Delta t^+ = 3\tilde{s}_2^2 + 3\tilde{s}_1 \tilde{s}_2 \\ -6\tilde{k}_p^{+*} + 12\tilde{k}_d^{+*} + 12c^+ \Delta t^+ = -3\tilde{s}_2^2 \tilde{s}_1 - \tilde{s}_2^3 \\ 12\tilde{k}_p^+ = \tilde{s}_1 \tilde{s}_2^3 \end{gathered} \tag{4.10}$$

Then $\tilde{k}_p^{+*}$, $\tilde{k}_d^{+*}$, $\tilde{s}_1$ and $\tilde{s}_2$ can be solved as functions of $c^+ \Delta t^+$ and $t_{CL}^{+*} = \frac{\Delta t^+}{-\tilde{s}_1}$.

4.4 Restoring process under perturbations

The closed-loop time measures the restoring rate of the rotational velocity (Cheng, Tobalske *et al.* 2016; Liu and Cheng 2017), however, sometimes it is more important to stabilize the attitude. For example, a deviation of roll angle produces a net lateral force and induces undesired side slide when the insects hope to stay hovering. The restoring process can be divided into three stages: (i) passive-dominant stabilization without active control due to the time delay with an initial velocity deviation aroused by a short perturbation while the attitude deviation grows; (ii) active control eliminates the velocity deviation and the attitude deviation peaks; and (iii) active control to eliminate the attitude deviation. For simplicity, the dynamics of the insect is considered with the initial condition $\dot{\xi}^+(0) = 1, \xi^+(0) = 0$ and $\mathrm{T} = 0$, (4.5) is simplified to

$$\Xi(s) = \frac{1 + \frac{\tilde{s}}{2} + \frac{\tilde{s}^2}{12}}{(\tilde{s}^2 + c^+\Delta t^+\tilde{s})\left(1 + \frac{\tilde{s}}{2} + \frac{\tilde{s}^2}{12}\right) + \left(\tilde{k}_p^+ + \tilde{k}_d^+\tilde{s}\right)\left(1 - \frac{\tilde{s}}{2} + \frac{\tilde{s}^2}{12}\right)} \tag{4.11}$$

Given the control parameters, aerodynamic damping, time delay and the poles different from each other, equation (4.11) can be decomposed to

$$\Xi(s) = \frac{q_1}{\tilde{s} - s_1} + \frac{q_2}{\tilde{s} - s_2} + \frac{q_3}{\tilde{s} - s_3} + \frac{q_4}{\tilde{s} - s_4} \tag{4.12}$$

where q_1, q_2, q_3, q_4, s_1, s_2, s_3 and s_4 can be obtained by comparing the coefficients of (4.11) and (4.12) (Descartes 1637). Therefore, by applying inverse Laplace transformation to (4.12), the time evolution for equation (4.4) can be solved, as

$$\xi^+ = q_1 e^{s_1 t^+} + q_2 e^{s_2 t^+} + q_3 e^{s_3 t^+} + q_4 e^{s_4 t^+} \tag{4.13}$$

On the other hand, if three poles are identical, as shown in equation (4.9), then (4.11) can be decomposed to

$$\Xi(s) = \frac{q_1}{\tilde{s} - s_1} + \frac{q_2}{(\tilde{s} - s_2)^3} + \frac{q_3}{(\tilde{s} - s_2)^2} + \frac{q_4}{\tilde{s} - s_2} \tag{4.14}$$

Where s_1 and s_2 can be identified by equation (4.10) and q_1, q_2, q_3, q_4 can be obtained by comparing the coefficients of the numerators of (4.14) and (4.11) (Descartes 1637). By applying inverse Laplace transformation to (4.14), the time evolution for equation (4.4) can be solved, as

$$\xi^+ = q_1 e^{s_1 t^+} + \left(q_2 \frac{t^{+2}}{2} + q_3 t^+ + q_4\right) e^{s_2 t^+} \tag{4.15}$$

Equation (4.15) represents the restoring process with minimized closed-loop time constant and is conventionally treated as the fastest stabilization (Cheng, Tobalske *et al.* 2016; Liu and Cheng 2017).

4.5 Results

4.5.1 Effects of aerodynamic damping

Beatus *et al* studied the response of fruit flies *Drosophila melanogaster* to the roll perturbation (Beatus, Guckenheimer *et al.* 2015), of which the dynamics is

$$\ddot{\rho} = -c\dot{\rho} - \beta\left[k_p\rho(t-\Delta t) + k_d\dot{\rho}(t-\Delta t)\right] + \tau \qquad (4.16)$$

The experimentally fitted coefficients of the control model are $\beta = 2 \times 10^4 s^{-2}$, $k_p^m = 0.7$, $k_d^m = 6 \times 10^{-3} s$, $\Delta t = 4.4 \times 10^{-3} s$. ρ represents the roll motion. τ is the external torque to induce roll perturbation which is generated by the interaction of the magnet glued to the fruit flies and the applied magnetic pulse which lasts about 5 ms (Beatus, Guckenheimer *et al.* 2015), the stroke cycle $T = 4.6 \times 10^{-3} s$.The nondimensionalized dynamic equation is

$$\ddot{\rho}^+(t^+) = -c^+\dot{\rho}^+(t^+) + \tau^+ - k_p^+[\rho^+(t^+ - \Delta t^+) + \lambda^+\dot{\rho}^+(t^+ - \Delta t^+)] \qquad (4.17)$$

The dimensionless coefficients are summarized in Table 4.1. Beatus *et al* (Beatus, Guckenheimer *et al.* 2015) found that the aerodynamic damping c is insignificant for stabilizing rotation rate, however, here we argued that the aerodynamic damping c is of vital importance for the stabilization process. We solved the dynamic equation (4.16) (or (4.17)) with varied magnitude of the external torque and set the aerodynamic damping to be 0. The value of external torque only affects the level of roll deviation and the time evolutions of roll motion are oscillatory decays for any case (Figure 4.3*a*), which is essentially different from the experimental measurement (Figure 4.3*b*, Figure 1 in (Beatus, Guckenheimer *et al.* 2015)). On the contrary, if the aerodynamic damping is taken into account, the time evolution of roll motion solved from equation (4.16) (or (4.17)) can be well consistent with the experimental results, of which $c^+ = 0.46$, $\tau^+ = 0.93$. This implies that the aerodynamic effect (also called flapping counter-torque (FCT) (Hedrick, Cheng *et al.* 2009)) is important in flight stabilization and the insects are smart enough to select the appropriate control parameters to counteract the effects of aerodynamic damping.

4.5.2 Oscillatory mode can accelerate stabilization

Ristroph, L. *et al* studied the response of fruit flies *Drosophila melanogaster* to the yaw perturbation (Ristroph, Bergou *et al.* 2010). The dimensionless aerodynamic damping coefficient c^+, time delay Δt^+ and experimentally fitted control parameters k_p^{+m}, λ^{+m} are summarized in Table 4.1. We optimize the control parameters k_p^{+CL}, λ^{+CL} following the principle that minimizing the closed-loop time constant (see Table 4.1). As shown in Figure

4.4a, the time course of yaw with k_p^{+m}, λ^{+m} well reproduces the experimental measurement and restores faster than that with k_p^{+CL}, λ^{+CL}. The main discrepancy between the time courses with k_p^{+m}, λ^{+m} and k_p^{+CL}, λ^{+CL} mainly occurs in stage (iii), i.e. after yaw deviation peaks. This indicates that the closed-loop time constant is significant only for short term at the beginning of a stabilization and works poorly for long-term prediction.

We then increase the optimized proportional gain k_p^{+*} from 0.116 to 0.166 (Figure 4.4a) and consequently, the closed-loop time constant increases. It is surprising that the stabilization accelerates and approximates to experimental results, though the accelerated stabilization induces a notable overshoot and is still not comparable with the experimental data. From the root locus of measured control parameters (Figure 4.4b), we find that there are three poles with equal real part and two of them are conjugate with imaginary parts, implying that the dynamics is oscillatory. To understand how such oscillatory mode accelerates the stabilization, we work out the analytical expression of the time evolution of yaw based on the measured control parameters from the equation (4.13),

$$\psi^+ = 0.2e^{-2.4t^+} + 2.3(1 + \sin(0.5t^+ - 1))e^{-0.35t^+} \tag{4.18}$$

The first term $0.2e^{-2.4t^+}$ represents fast decay, which damps out quickly and can be neglected (Figure 4.5). The second term represents oscillatory decay. After about 10 wing beats, yaw angle is near zero, indicating the stabilization is almost completed (Figure 4.5). It should be noted that the oscillatory feature of (4.18) can induce a very minor overshoot, about 2% of the maximal yaw deviation (inset in Figure 4.5), which is thought not to affect the stable state. On the other hand, the time evolution of yaw with minimal closed-loop time constant is

$$\psi^+ = -0.12e^{-1.8t^+} + (0.31t^{+2} + 0.84t^+ + 0.12)e^{-0.5t^+} \tag{4.19}$$

The first term $-0.1e^{-1.8t^+}$ also represents fast decay and can be neglected. Although the exponential decay coefficient of (4.19) (-0.5) is smaller than that of (4.18) (-0.35), indicating fast decay of (4.19), the magnitude of the exponential term of (4.19) is formulated by the polynomial function which slows down the decay. After about 10 wing beats, the yaw has not been stabilized with a deviation of 0.2 (Figure 4.5).

Therefore, to achieve fast stabilization, insects do not choose to minimize the closed-loop time constant. Instead, oscillatory mode is introduced to accelerate stabilization.

4.5.3 Restoring time

Because the closed-loop time constant is not suited to assess the time spent for stabilization control, we thereby turn to the restoring time t_{RT}^+ instead, the time spent by the insects to restore to equilibrium. Here, the restoring time defined by the time when the deviation restores to the 5% of maximal deviation and never exceeds this value later on

(Elzinga, Dickson *et al.* 2012). As pointed out in section 4.5.2, there are three poles have the same real part (Figure 4.4*b*) for the characteristic equation of experimentally measured control parameters and two of them have conjugated imaginary parts which induces oscillatory mode to the dynamic flapping system. We then sweeping the control parameters k_p^+ and λ^+ to minimize the restoring time t_{RT}^+ under the constraints that three poles of the characteristic equation have the same real part, of which the resultant control parameters are termed k_p^{+RT} and λ^{+RT} and summarized in Table 4.1.

It can be seen that the control parameters k_p^{+RT} and λ^{+RT} can reproduce the stabilization flight of fruit fly well consistent with the experimental results, while k_p^{+CL} and λ^{+CL} only capture the rise stages ((i) and (ii)) and cause much slower correction of attitude deviation (Figure 4.6*a*, *b*). In addition, for both k_p^{+RT}, λ^{+RT} and k_p^{+CL}, λ^{+CL}, the rise stages are similar and close to experimental results. At stage (i), the controller has not been activated, so the stabilization is totally passive. Therefore, it can be inferred that the rise stage is insensitive to control parameters, which, again, confirms that closed-loop time constant is not an appropriate index to judge the performance of a controller because it mainly serves at rise stage.

To demonstrate the rationality of restoring time as a metric of stabilization, we show the closed-loop time constant versus restoring time by sweeping the control parameters. As shown in Figure 4.6*c* and *d*, there exist control parameters resulting in minimal closed-loop time constant (k_p^{+CL} and λ^{+CL}) and control parameters resulting in minimal restoring time. The (t_{CL}^+, t_{RT}^+) resulted from experimentally fitted control parameters (k_p^{+m}, λ^{+m}) lies within the regime with the minimal restoring time, suggesting that the fruit fly prefers to minimize the restoring time rather than closed-loop time constant. In addition, (t_{CL}^+, t_{RT}^+) resulted from (k_p^{+RT}, λ^{+RT}) also lies within the same regime, validating the effectiveness of the method that minimize the restoring time under the condition that three poles of the characteristic equation have the same real number.

4.5.4 Generalization to other species

We demonstrated that the fruit fly possesses such a highly developed control system (well integrating the motorsensory system, central nerves system and musculoskeletal system) to minimize the restoring time which takes the aerodynamic effect into account with an inevitable time delay. Here, we farther test the principle minimizing the restoring time to other species with different size. The honeybee *apis mellifera* and magnificent hummingbird *eugenes fulgens* are taken as two examples, because their respond times to perturbations are available from prior literature (Ristroph, Ristroph *et al.* 2013; Vance, Faruque *et al.* 2013;

Cheng, Tobalske *et al.* 2016; Liu and Cheng 2017) (Figure 4.7). The dynamic coefficients and control parameters are summarized in Table 4.1. Although not insects, hummingbirds behave similar to insects (Cheng, Tobalske *et al.* 2016) and are treated as the upper limits of flying insects.

As illustrated in Figure 4.7*a*, although the closed-loop time constant of honeybee is not available, its restoring time is nearly the minimal restoring time, indicating that the honeybee also follows the principle that minimizing the restoring time in flight stabilization. For magnificent hummingbird, the measured restoring time (~5) is notably larger than the minimal restoring time (~4), but much smaller than the restoring time corresponding to the minimized closed-loop time constant (Figure 4.7*b*). Therefore, the magnificent hummingbird may also attempt to minimize the restoring time.

4.6 Discussions

4.6.1 Effects of aerodynamic damping and time delay

Up to now, we have studied four different stabilization maneuvers of three different species, among which the aerodynamic damping and time delay vary broadly. Here, to gain a general impression, we study how the aerodynamic damping and time delay influence the stabilization performance of flying insects.

We first check whether there exists some relationship between the minimized restoring time t_{RT}^{+} and minimized closed-loop time constant t_{CL}^{+}. From Figure 4.8*a*, for a flapping system, its minimal restoring time is well linearly correlated with its minimal closed-loop time constant (green dots and line) with proportionality 3.5. In addition, the restoring time of a flapping system achieving minimal closed-loop time constant is also linearly correlated with the minimal closed-loop time constant (red dots and line) with proportionality 7.3. Therefore, compared with the principle to minimize closed-loop time constant, the flight stabilization can be largely accelerated twice as fast when minimizing the restoring time.

Because of the linearity between minimized restoring time and minimized closed-loop time constant, the effects of aerodynamic damping and time delay on them are the same. As time delay increases and aerodynamic damping decreases, the closed-loop time constant increases (Figure 4.8*b*), confirming that time delay have disastrous implications for flight stabilization (Elzinga, Dickson *et al.* 2012) while aerodynamic damping facilitates flight stabilization (Hedrick, Cheng *et al.* 2009). Aerodynamic damping can be treated as a derivative feedback without time delay (see equation (4.3) and (4.4)), explaining the reason why aerodynamic damping facilitates flight stabilization. In addition, the minimal closed-loop time constant becomes insensitive to aerodynamic damping as time delay approaches zero (Figure 4.8*b*).

Once the closed-loop time constant is minimized, the poles of the characteristic equation (4.7) are all real of which three are identical (Cai, Kolomenskiy *et al.* 2021). To acquire quantitative understanding of the effects of aerodynamic damping and time delay, we then solve the equation set (4.10) to directly obtain the minimal closed-loop time constant, see Section 4.3. With arbitrary aerodynamic damping, the inverse of minimal closed-loop time constant tends to be linearly correlated with the inverse of time delay Δt^+ when it approaches zero (Figure 4.8*c*), with slope 0.59. More generally, the inverse of minimal closed-loop time constant t_{CL}^{+*} is linearly correlated with the inverse of time delay Δt^+, for constant $c^+\Delta t^+$ (Figure 4.8*c*). From Figure 4.8*c*, we find that the minimal closed-loop time constant has an upper limit $t_{CL}^{+*} \leq 1.7\Delta t^+$. Thereby, the minimal restoring time has an upper limit $t_{RT}^{+*} \leq 6\Delta t^+$ at aerodynamic damping equals zero. Such estimation is based on no biological limitations, which may not hold for some species of insects or hummingbird. The proportional gain and derivative gain with minimal restoring time is higher than those with minimal closed-loop time constant for fruit fly, honeybee and hummingbird (Table 4.1), suggesting that more dramatic wing motion adjustment is required for faster stabilization, which may lead to biological limitations. For example, the stabilization performance of magnificent hummingbirds may be limited by its muscle power capacity (Liu and Cheng 2017) and are unable to reach the minimal restoring time (Figure 4.7*b*). Fruit flies are demonstrated to be able to achieve the fastest stabilization (Figure 4.6), indicating that they are not constraints by biological limitations.

4.6.2 Multi-degree stabilization

So far, the flight stabilization is mainly focused on single degree of freedom. The dynamic equation (4.1) can be applied to depict many dynamic responses of flying insects, such as the stabilization on the body attitude which are largely perturbed in one direction (Hedrick, Cheng *et al.* 2009; Bergou, Ristroph *et al.* 2010; Ristroph, Bergou *et al.* 2010; Beatus, Guckenheimer *et al.* 2015) and decoupled multi-degree-of-freedom dynamics (Cai, Kolomenskiy *et al.* 2021). However, the six degrees of freedoms of flying insects (yaw, pitch, roll, fore/aft, lateral, vertical) inevitably couple with each other, of which the dynamic equations could be different from equation (4.1) or (4.3) (Cheng, Deng *et al.* 2011; Ristroph, Ristroph *et al.* 2013). For instance, variation in pitch can essentially alter the direction of aerodynamic force which not only affect the dynamics of attitude but also affect the translational dynamics (Windsor, Bomphrey *et al.* 2014).

Now, we move farther to study the control on free longitudinal flight of hawkmoths (Cheng, Deng *et al.* 2011) to study whether the restoring time is also minimized under coupled dynamics. The pitch motion is always coupled with the forward/afterward motion (Ristroph, Ristroph *et al.* 2013), as depicted by the following equations

$$\ddot{x}(t) = -\frac{k_{\dot{x}}}{m}\dot{x}(t) + g\sin(\theta(t) - \theta_0) \tag{4.20}$$

$$\ddot{\theta}(t) = -\frac{k_p}{I}(\theta(t - \Delta t_\theta) - \theta_0) - \frac{k_d}{I}\dot{\theta}(t - \Delta t_{\dot{\theta}}) - \frac{M_\theta}{I}\dot{\theta}(t) - \frac{k_x^\theta}{I}\dot{x}(t) \tag{4.21}$$

where $I = 267 \times 10^{-9} kgm^2$, $m = 1.42 \times 10^{-3} kg$, $M_\theta = 1329 \times 10^{-9} mNs$, $k_x^\theta = 69 \times 10^{-6} Ns$, Δt_θ and $\Delta t_{\dot{\theta}}$ are the time delays corresponding to pitch angle and pitch angular velocity. The stroke cycle $T = 0.0345s$. It should be noted that there is a time delay in the term $\sin\theta(t)$ in the original literature (Cheng, Deng *et al.* 2011) which is not physical, so the time delay in this term is removed in this study. The hawkmoth relies mainly on aerodynamic damping effect to slow down the body translation while active pitch control is indispensable (Cheng, Deng *et al.* 2011), therefore, it is presumed that there is no direct feedback from body translation and $k_{\dot{x}}$ represents the aerodynamic damping effect which is set to be $7.2 \times 10^{-3} Nsm^{-1}$. Although no direct active control on translational motion, the control parameters k_p and k_d can indirectly affect translational motion through the coupling term $g\sin(\theta(t) - \theta_0)$.

Bo Cheng *et al* (Cheng, Deng *et al.* 2011) studied the evading behavior of hawkmoths encountering visual stimuli in the front, which consists two successive stages: (1) a fast pitch up and backward maneuver and (2) a relatively slow restoring to hovering. Because this stabilization is an evading maneuver, the hawkmoth may prefer to control translational motion prior to pitch motion so as to move away from the stimuli. This point of view can be supported by the fact that the hawkmoths choose to adjust the mean rotational angle rather than the mean positional angle during the evading behavior (Cheng, Deng *et al.* 2011). Change of mean positional angle produces a pitch moment only, while change of mean rotational angle produces a pitch moment as well as a translational force which can be applied to control translational motion. Therefore, here the restoring time is defined as the time when the translational velocity restores to the 5% of maximal deviation of translational velocity and never exceeds this value later on.

For simplicity, $\sin(\theta(t) - \theta_0)$ is approximated by $\theta(t) - \theta_0$. By applying Laplace transformation to dynamic equations (19) and (20), one can obtain the transfer functions

$$G_x(s) = \frac{1}{ms^2 + k_{\dot{x}}s}\frac{1}{Is^2 + M_\theta s + \frac{mgk_x^\theta}{ms + k_{\dot{x}}} + \left(k_p e^{-\Delta t_\theta s} + k_d s e^{-\Delta t_{\dot{\theta}} s}\right)} \tag{4.22}$$

$$G_\theta(s) = \frac{1}{Is^2 + M_\theta s + \frac{mgk_x^\theta}{ms + k_{\dot{x}}} + \left(k_p e^{-\Delta t_\theta s} + k_d s e^{-\Delta t_{\dot{\theta}} s}\right)} \tag{4.23}$$

where $G_x(s)$ is the transfer function about translational motion x and $G_\theta(s)$ the pitch motion θ. Different from the single-degree-of-freedom transfer functions, there are coupling terms $\frac{1}{Is^2+M_\theta s+\frac{mgk_x^\theta}{ms+k_{\dot{x}}}+\left(k_p e^{-\Delta t_\theta s}+k_d s e^{-\Delta t_{\dot{\theta}} s}\right)}$ in equation (4.22) and $\frac{mgk_x^\theta}{ms+k_{\dot{x}}}$ in equation (4.23). Interestingly, the characteristic equations of the preceding equations are the same

$$1 + k_p \frac{e^{-\Delta t_\theta s} + \frac{k_d}{k_p} s e^{-\Delta t_{\dot{\theta}} s}}{Is^2 + M_\theta s + \frac{mgk_x^\theta}{ms + k_{\dot{x}}}} = 0 \tag{4.24}$$

This indicates that well selected control parameters k_p and k_d should guarantee the convergence of both pitch and translational motions. Compared with single-degree-of-freedom characteristic equations, there is an extra coupling term $\frac{mgk_x^\theta}{ms+k_{\dot{x}}}$ in equation (4.24).

The antennas of moths function similar to the halteres of the fruit flies (Sane, Dieudonné *et al.* 2007), which suggests a low time delay (Hedrick and Daniel 2006). Bo Cheng *et al* (Cheng, Deng *et al.* 2011) swept the time delay and identified the control parameters by fitting from measured motions of hawkmoth. Here, we choose the time delay $\Delta t_\theta = T$ and $\Delta t_{\dot{\theta}} = 0.25T$. The control parameters from experimental fitting, with minimal closed-loop time constant and minimal restoring time are summarized in Table 4.1. The experimentally restoring time (5.7) is remarkably close to the minimal restoring time (5.4) and the corresponding closed-loop time constant is much larger than the minimal closed-loop time constant (Figure 4.9), suggesting that the hawkmoth with longitudinal motion also follows the principle to minimize the restoring time.

The pitch and translation motion are simultaneously controlled through one PD controller, so when the translation is controlled ideally with minimal restoring time, the control performance of pitch can be poor (Figure 4.10), of which there is a significant overshoot. To achieve good control performance of pitch as well, another PD controller with feedback of pitch may be necessary, so that both the translation and pitch motion are directly sensed and more freedoms of wing motion can be actively adjusted (Cai, Kolomenskiy *et al.* 2021).

4.6.3 The role of aerodynamic damping

There exist different (even contradictory) opinions on the role the aerodynamic damping plays in the flight stabilization of insects. Hedrick et al (Hedrick, Cheng *et al.* 2009) compared two hypotheses: a passive model with the turning torque proportional to rotation rate and an active model with constant turning torque and found that the exponential decay observed by experimental measurements is well consistent with the prediction of passive model, suggesting that the flight stabilization is entirely mediated by the passive damping. However, Beatus *et al* (Beatus, Guckenheimer *et al.* 2015) found that the recovery roll manoeuvre with passive damping solely is much slower than the experimental data, indicating the necessity of active mediation. Elzinga *et al* (Elzinga, Dickson *et al.* 2012) pointed out that the exponential decay could also be induced by proportional active feedback, a similar role of passive damping by introducing a feedback proportional to the rotation rate (see equation (4.3)). Here is the question: what is the role of aerodynamic damping in flight stabilization under active control? As is evident from Section 4.5.1, the insects evolve the control system by taking the aerodynamic damping into account. From the point of view from our analytical framework, the aerodynamic damping is a proportional feedback of rotation rate without time delay. Because the time delay have disastrous implications for flight performance (Elzinga, Dickson *et al.* 2012), aerodynamic damping can facilitate the stabilization (Figure 4.8*b*, *c*) and hence improve the controllability.

4.6.4 Compare P, D and PD control

Up to now, the control strategy discussed is the proportional-derivative (PD) control, which is universally adopted by flying insects (Ristroph, Bergou *et al.* 2010; Cheng, Deng *et al.* 2011; Beatus, Guckenheimer *et al.* 2015; Whitehead, Beatus *et al.* 2015). For completeness, we further extend our discussion on proportional-only (P) control and derivative-only (D) control. Because flying insects are unlikely to sensor their body accelerations (Leeuwen and Dickinson 1999), we exclude the discussion on the feedback of acceleration. The D controller does not sensor neither the position nor the attitude (roll, pitch and yaw) of the insect, so the insects will not restore to the equilibrium (or desired) position and attitude. Because change in position and yaw does not alter the state of the insect, D control can be applied to these directions of motions to stabilize the velocities (Elzinga, Dickson *et al.* 2012; Cheng, Tobalske *et al.* 2016). On the other hand, although P controller detect the position or attitude only, it guarantees zero velocity when reaching equilibrium. Capable of controlling both the state and its time derivative, P control and PD control are compared here. The transfer function of P control for single degree of freedom is

$$G_P(s) = \frac{1}{s^2 + c^+ s + k_p^+ e^{-\Delta t^+ s}} \tag{4.25}$$

The corresponding characteristic equation is

$$1 + k_p^+ \frac{e^{-\Delta t^+ s}}{s^2 + c^+ s} = 0 \tag{4.26}$$

Because the minimal restoring time and closed-loop time constant are positively correlated, here we use closed-loop time constant to compare the control performances of P control and PD control. Using the root locus method under the principle minimizing the closed-loop time constant, the proportional gains k_p^+ of P control are much smaller than that of PD control (Figure 4.11*a*, *b*), which indicates that the P control is not robust to proportional gain and easily diverge. The closed-loop time constant of P control are much larger than that of PD control (Figure 4.8*b* and Figure 4.11*c*). The unrobustness and long characteristic restoring time of P control indicate that PD control is preferable to the flying insects.

References

Beatus, T., Guckenheimer, J. M., Cohen, I., Controlling Roll Perturbations in Fruit Flies, Journal of the Royal Society Interface, Vol. 12, No. 105 (2015),pp. 20150075.

Bergou, A. J., Ristroph, L., Guckenheimer, J., Cohen, I., Wang, Z. J., Fruit Flies Modulate Passive Wing Pitching to Generate in-Flight Turns, Physical Review Letters, Vol. 104, No. 14 (2010),pp. 148101.

Bluman, J. E., Sridhar, M. K., Kang, C.-k., Chordwise Wing Flexibility May Passively Stabilize Hovering Insects, Journal of the Royal Society Interface, Vol. 15, No. 147 (2018),pp. 20180409.

Cai, X., Kolomenskiy, D., Nakata, T., Liu, H., A Cfd Data-Driven Aerodynamic Model for Fast and Precise Prediction of Flapping Aerodynamics in Various Flight Velocities, Journal of Fluid Mechanics, Vol. 915, No. (2021),pp. A114.

Chang, S., Wang, Z. J., Predicting Fruit Fly's Sensing Rate with Insect Flight Simulations, Proceedings of the National Academy of Sciences, Vol. 111, No. 31 (2014),pp. 11246.

Cheng, B., Deng, X., Hedrick, T. L., The Mechanics and Control of Pitching Manoeuvres in a Freely Flying Hawkmoth (*Manduca Sexta*), Journal of Experimental Biology, Vol. 214, No. 24 (2011),pp. 4092.

Cheng, B., Tobalske, B. W., Powers, D. R., Hedrick, T. L., Wang, Y., Wethington, S. M., Chiu, G. T. C., Deng, X., Flight Mechanics and Control of Escape Manoeuvres in Hummingbirds. Ii. Aerodynamic Force Production, Flight Control and Performance Limitations, The Journal of Experimental Biology, Vol. 219, No. 22 (2016),pp. 3532.

Cheng, B., Tobalske, B. W., Powers, D. R., Hedrick, T. L., Wethington, S. M., Chiu, G. T. C., Deng, X., Flight Mechanics and Control of Escape Manoeuvres in Hummingbirds. I. Flight Kinematics, The Journal of Experimental Biology, Vol. 219, No. 22 (2016),pp. 3518.

Deora, T., Gundiah, N., Sane, S. P., Mechanics of the Thorax in Flies, Journal of Experimental Biology, Vol. 220, No. 8 (2017),pp. 1382.

Descartes, R., Discours De La Methode Pour Bien Conduire Sa Raison, & Chercher La Verité Dans Les Sciences. Plus La Dioptriqve. Les Meteores. Et La Geometrie. Qui Sont Des Essais De Cete Methode (1637)

Elzinga, M. J., Dickson, W. B., Dickinson, M. H., The Influence of Sensory Delay on the Yaw Dynamics of a Flapping Insect, Journal of the Royal Society Interface, Vol. 9, No. 72 (2012),pp. 1685-1696.

Evans, W. R., Graphical Analysis of Control Systems, Transactions of the American Institute of Electrical Engineers, Vol. 67, No. 1 (1948),pp. 547-551.

Fayyazuddin, A., Dickinson, M. H., Haltere Afferents Provide Direct, Electrotonic Input to a Steering Motor Neuron in the Blowfly, *Calliphora*, Journal of Neuroscience, Vol. 16, No. 16 (1996),pp. 5225.

Franklin, G. F., Powell, J. D., Emami-Naeini, A., Feedback Control of Dynamic Systems, Prentice Hall Press (2014)

Gao, N., Aono, H., Liu, H., A Numerical Analysis of Dynamic Flight Stability of Hawkmoth Hovering, Journal of Biomechanical Science and Engineering, Vol. 4, No. 1 (2009),pp. 105-116.

Hedrick, T. L., Cheng, B., Deng, X., Wingbeat Time and the Scaling of Passive Rotational Damping in Flapping Flight, Science, Vol. 324, No. 5924 (2009),pp. 252.

Hedrick, T. L., Daniel, T. L., Flight Control in the Hawkmoth *Manduca Sexta*: The Inverse Problem of Hovering, The Journal of Experimental Biology, Vol. 209, No. 16 (2006),pp. 3114.

Hesselberg, T., Lehmann, F.-O., Turning Behaviour Depends on Frictional Damping in the Fruit Fly Drosophila, Journal of Experimental Biology, Vol. 210, No. 24 (2007),pp. 4319-4334.

Kinoshita, M., Homberg, U., Insect Brains: Minute Structures Controlling Complex Behaviors, Brain Evolution by Design: From Neural Origin to Cognitive Architecture. S. Shigeno, Y. Murakami, T. Nomura. Tokyo, Springer Japan**:** 123-151 (2017)

Leeuwen, J. L. v., Dickinson, M. H., Haltere–Mediated Equilibrium Reflexes of the Fruit Fly, Drosophila Melanogaster, Philosophical Transactions of the Royal Society of London. Series B: Biological Sciences, Vol. 354, No. 1385 (1999),pp. 903-916.

Liu, P., Cheng, B., Limitations of Rotational Manoeuvrability in Insects and Hummingbirds: Evaluating the Effects of Neuro-Biomechanical Delays and Muscle Mechanical Power, Journal of the Royal Society Interface, Vol. 14, No. 132 (2017),pp. 20170068.

Matthews, M., Sponberg, S., Hawkmoth Flight in the Unsteady Wakes of Flowers, The Journal of Experimental Biology, Vol. 221, No. 22 (2018),pp. jeb179259.

Muijres, F. T., Elzinga, M. J., Melis, J. M., Dickinson, M. H., Flies Evade Looming Targets by Executing Rapid Visually Directed Banked Turns, Science, Vol. 344, No. 6180 (2014),pp. 172.

Ortega-Jimenez, V. M., Greeter, J. S. M., Mittal, R., Hedrick, T. L., Hawkmoth Flight

Stability in Turbulent Vortex Streets, The Journal of Experimental Biology, Vol. 216, No. 24 (2013),pp. 4567.

Pringle, J. W. S., Gray, J., The Gyroscopic Mechanism of the Halteres of Diptera, Philosophical Transactions of the Royal Society of London. Series B, Biological Sciences, Vol. 233, No. 602 (1948),pp. 347-384.

Ravi, S., Kolomenskiy, D., Engels, T., Schneider, K., Wang, C., Sesterhenn, J., Liu, H., Bumblebees Minimize Control Challenges by Combining Active and Passive Modes in Unsteady Winds, Scientific Reports, Vol. 6, No. 1 (2016),pp. 1-10.

Ristroph, L., Bergou, A. J., Ristroph, G., Coumes, K., Berman, G. J., Guckenheimer, J., Wang, Z. J., Cohen, I., Discovering the Flight Autostabilizer of Fruit Flies by Inducing Aerial Stumbles, Proceedings of the National Academy of Sciences, Vol. 107, No. 11 (2010),pp. 4820.

Ristroph, L., Ristroph, G., Morozova, S., Bergou, A. J., Chang, S., Guckenheimer, J., Wang, Z. J., Cohen, I., Active and Passive Stabilization of Body Pitch in Insect Flight, Journal of the Royal Society Interface, Vol. 10, No. 85 (2013),pp. 20130237.

Sane, S. P., Dieudonné, A., Willis, M. A., Daniel, T. L., Antennal Mechanosensors Mediate Flight Control in Moths, Science, Vol. 315, No. 5813 (2007),pp. 863.

Shyy, W., Aono, H., Kang, C.-k., Liu, H., An Introduction to Flapping Wing Aerodynamics, Cambridge, Cambridge University Press (2013)

Sun, M., Wang, J., Xiong, Y., Dynamic Flight Stability of Hovering Insects, Acta Mechanica Sinica, Vol. 23, No. 3 (2007),pp. 231-246.

Sun, M., Xiong, Y., Dynamic Flight Stability of a Hovering Bumblebee, The Journal of Experimental Biology, Vol. 208, No. 3 (2005),pp. 447.

Taylor, G. K., Thomas, A. L., Dynamic Flight Stability in the Desert Locust Schistocerca Gregaria, Journal of Experimental Biology, Vol. 206, No. 16 (2003),pp. 2803-2829.

Vance, J. T., Faruque, I., Humbert, J. S., Kinematic Strategies for Mitigating Gust Perturbations in Insects, Bioinspiration & Biomimetics, Vol. 8, No. 1 (2013),pp. 016004.

Whitehead, S. C., Beatus, T., Canale, L., Cohen, I., Pitch Perfect: How Fruit Flies Control Their Body Pitch Angle, Journal of Experimental Biology, Vol. 218, No. 21 (2015),pp. 3508.

Windsor, S. P., Bomphrey, R. J., Taylor, G. K., Vision-Based Flight Control in the Hawkmoth Hyles Lineata, Journal of the Royal Society Interface, Vol. 11, No. 91 (2014),pp. 20130921.

Winston, M. L., The Biology of the Honey Bee, harvard university press (1991)

Xiong, Y., Sun, M., Dynamic Flight Stability of a Bumblebee in Forward Flight, Acta Mechanica Sinica, Vol. 24, No. 1 (2008),pp. 25-36.

Yao, J., Yeo, K. S., Forward Flight and Sideslip Manoeuvre of a Model Hawkmoth, Journal of Fluid Mechanics, Vol. 896, No. (2020),pp. A22.

Zhang, C., Hedrick, T. L., Mittal, R., An Integrated Study of the Aeromechanics of Hovering Flight in Perturbed Flows, AIAA Journal, Vol. 57, No. 9 (2019),pp. 3753-3764.

Zhang, X., Liu, H., A Three-Axis Pd Control Model for Bumblebee Hovering Stabilization, Journal of Bionic Engineering, Vol. 15, No. 3 (2018),pp. 494-504.

List of figures

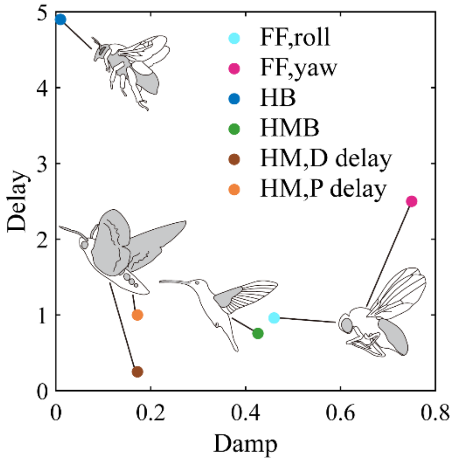

Figure 4.1 Dimensionless aerodynamic damping versus time delay for fruit fly (FF), honeybee (HB), hummingbird (HMB) and hawkmoth (HM).

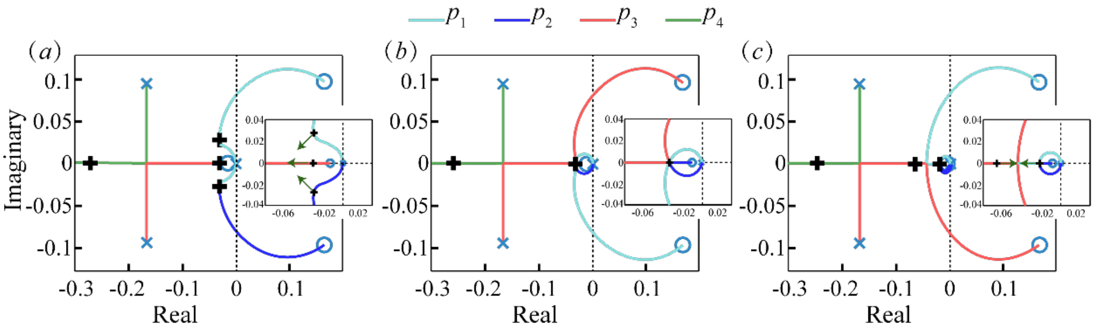

Figure 4.2 Root locus. (*a*) small controller time constant. The arrows in the inset indicate the variation of poles with increasing controller time constant, (*b*) optimal controller time constant, (*c*) large controller time constant. The arrows in the inset indicate the variation of poles with decreasing controller time constant. × and *o* indicate the proportional gain equals 0 and $+\infty$, respectively.

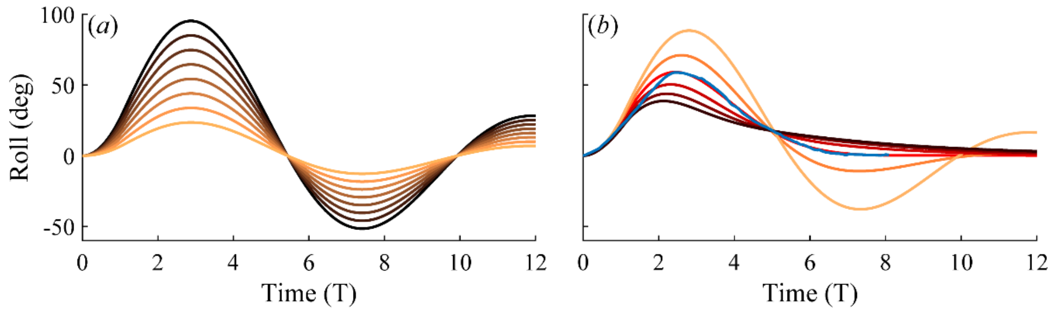

Figure 4.3 Roll motion of fruit fly. (*a*) Solution to equation (4.16) (or (4.17)) without aerodynamic damping. The curves are colored in relation to the magnitude of the external torque (from τ^{+} =0.33 to 0.93, or τ = $1.6 \times 10^4 s^{-2}$ nN to $4.4 \times 10^4 s^{-2}$) with higher external torque corresponding to darker colors. (*b*) blue curve: experimentally measured roll motion of fruit fly responding to perturbations, adopted from (Beatus, Guckenheimer *et al.* 2015). Other curves are the solutions to equation (4.16) or (4.17) with external torque τ^{+}=0.93 (τ=12.7 nN) and are colored in relation to the magnitude of aerodynamic damping (from c^{+} =0.06 to 1.06, or c =$13s^{-1}$ to $230s^{-1}$).

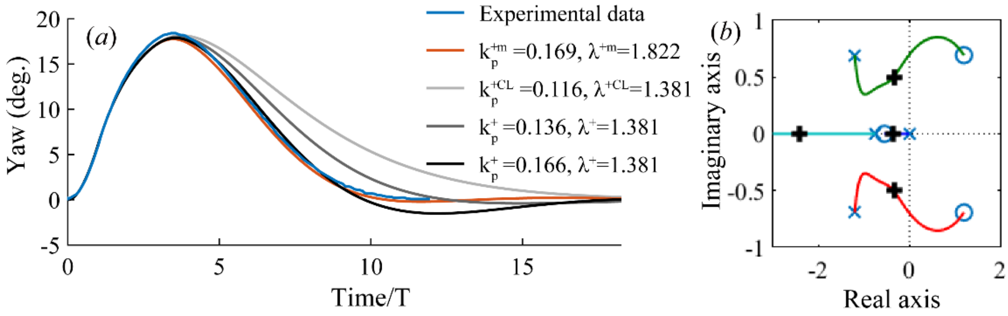

Figure 4.4 (*a*) Restoring time evolution of yaw of fruit fly with different control parameters. (*b*) Root locus with measured control parameter λ^{+m}. Black pluses represent the poles corresponding to the measured proportional gain k_p^{+m}. × and *o* indicate the proportional gain equals to 0 and $+\infty$, respectively.

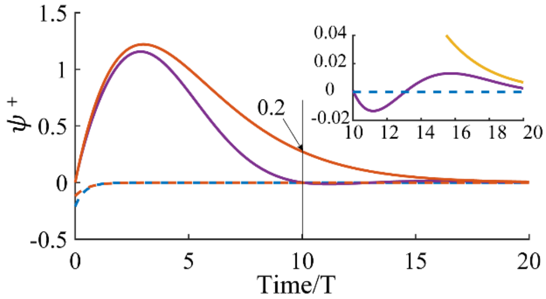

Figure 4.5 Time evolution of yaw of fruit fly with initial velocity $\dot{\psi}^+ = 1$. Equation (4.18): purple; equation (4.19): orange; dashed lines represent fast decay, respectively. Vertical black line indicates the time when the yaw is zero of equation (4.18).

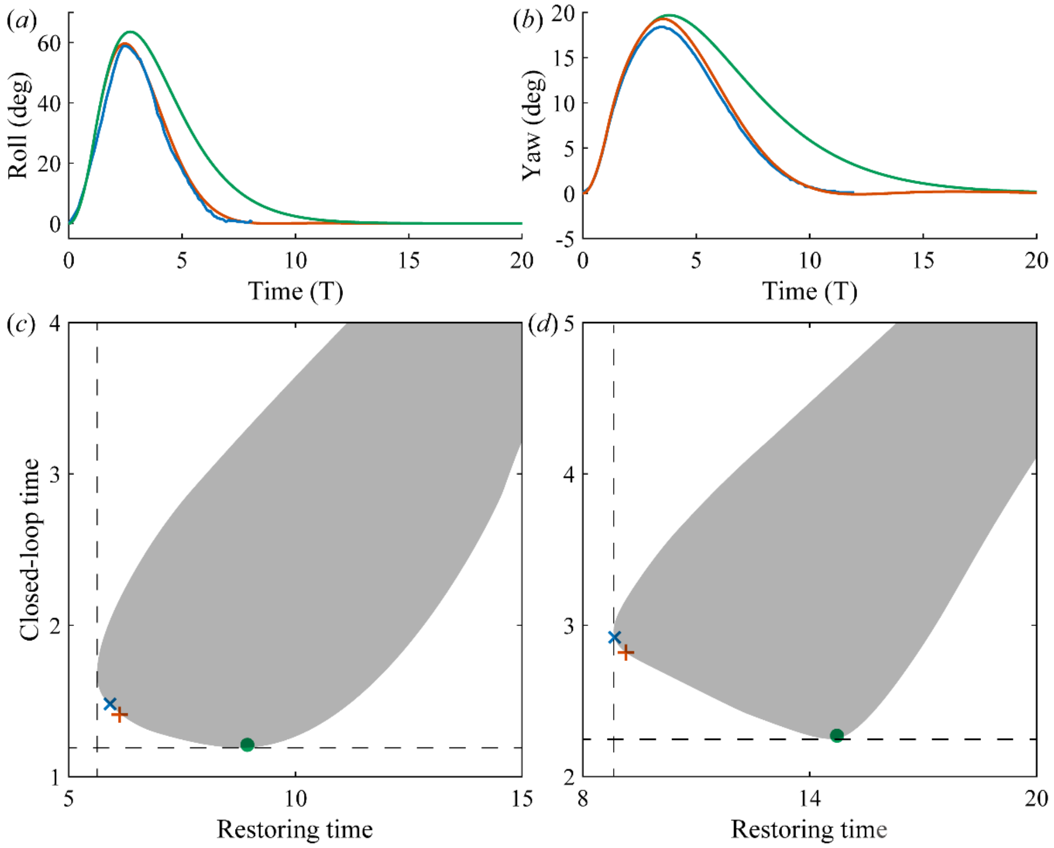

Figure 4.6 Time evolution of (*a*) roll and (*b*) yaw during stabilization of fruit fly. Blue line: experimental data; red line: solution to equation (3) with control parameters k_p^{+RT} and λ^{+RT} by minimizing restoring time; green line: solution to equation (4.4) with control parameters k_p^{+CL} and λ^{+CL} by minimizing closed-loop time constant. Closed-loop time constant versus restoring time of (*c*) roll and (*d*) yaw of fruit fly. Blue cross: experimentally fitted control parameters; red plus: control parameters k_p^{+RT} and λ^{+RT}; green circle: control parameters k_p^{+CL} and λ^{+CL}. Shadow regime: achievable closed-loop time constant and restoring time by sweeping control parameters. Horizontal dashed black line: minimal closed-loop time constant achievable; vertical dashed black line: minimal restoring time constant achievable.

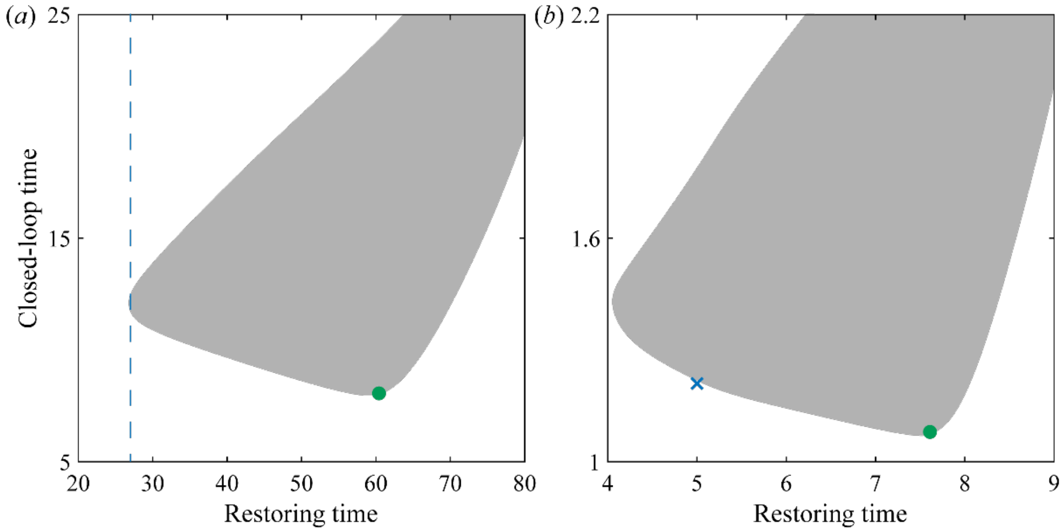

Figure 4.7 Closed-loop time constant versus restoring time of (*a*) honeybee and (*b*) magnificent hummingbird. Blue cross: experimentally fitted control parameters; green circle: control parameters k_p^{+CL} and λ^{+CL}. Shadow regime: achievable closed-loop time constant and restoring time by sweeping control parameters. Vertical dashed blue line in (*a*) indicates the measured restoring time of honeybee.

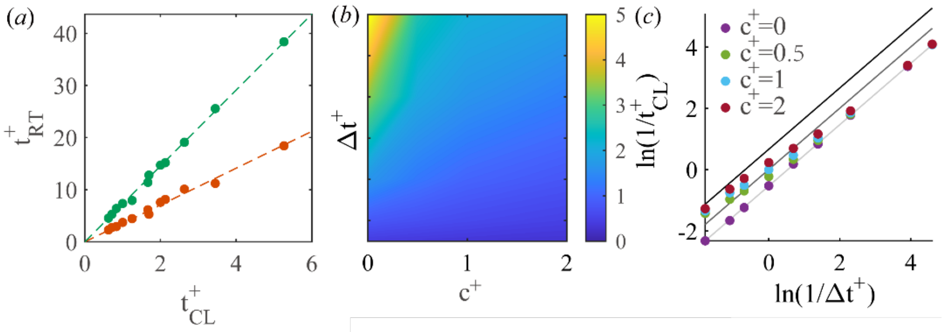

Figure 4.8 (*a*) Correlations between the restoring time and the minimal closed-loop time constant. Red dots: minimal restoring time; green dots: restoring time of a flapping system with minimized closed-loop time constant. Red and green dashed lines show the linear fitting with slopes 3.532 (R=0.99) and 7.279 (R=1.00), respectively. (*b*) Contour plots of minimal closed-loop time constant t_{CL}^{+*} as function of aerodynamic damping and time delay. (*c*) Correlation between minimal closed-loop time constant and time delay. The lines are colored in relation to the magnitude of $c^+\Delta t^+$ with higher $c^+\Delta t^+$ corresponding to darker colors with proportionality 1. For $c^+\Delta t^+ = 0$, the intercept is -0.53.

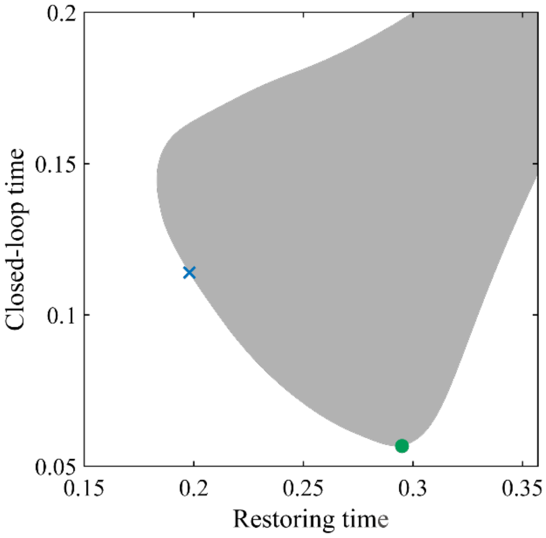

Figure 4.9 Closed-loop time constant versus restoring time of hawkmoth. Blue cross: experimentally fitted control parameters; green circle: control parameters k_p^{+CL} and λ^{+CL} resulting minimal closed-loop time constant. Shadow regime: achievable closed-loop time constant and restoring time by sweep control parameters.

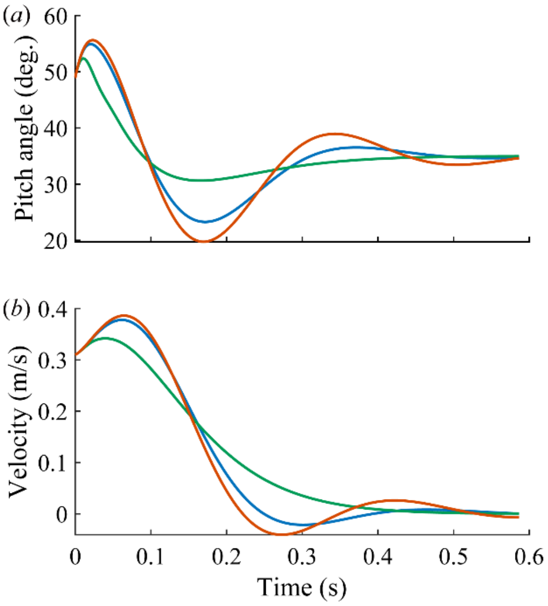

Figure 4.10 Time evolution of (*a*) pitch angle and (*b*) translational velocity in hawkmoth. Solutions to equations (4.20) and (4.21) with control parameters fitted from experiments, with minimal restoring time and minimal closed-loop time constant, which are illustrated by blue, red and green lines, respectively. The initial pitch angle and angular velocity are 49 degrees and 658 deg/s and the initial translational velocity is 0.31 m/s.

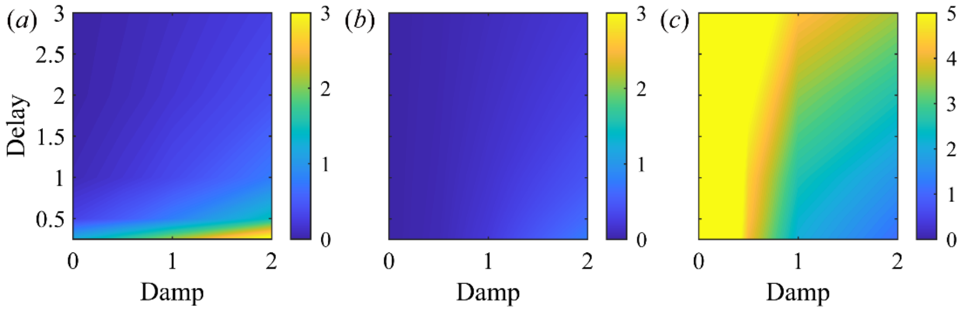

Figure 4.11 (*a*) Contour plot of optimized proportional gain of PD control as functions of aerodynamic effect and time delay. (*b*) Contour plot of optimized proportional gain and (*c*) closed-loop time constant of P control as functions of aerodynamic effect and time delay.

Beatus, T., Guckenheimer, J. M., Cohen, I., Controlling Roll Perturbations in Fruit Flies, Journal of the Royal Society Interface, Vol. 12, No. 105 (2015),pp. 20150075.

List of tables

Table 4.1 Dynamic coefficients and control parameters of different species.

		c^+	Δt^+	k_p^{+m}	λ^{+m}	k_p^{+CL}	λ^{+CL}	k_p^{+RT}	λ^{+RT}
Fruit fly	roll	0.46	0.96	0.2964	1.863	0.2028	2.03	0.286	1.85
	yaw	0.75	2.5	0.169	1.822	0.116	1.381	0.165	1.8
Honeybee		0.0098	4.9	-	-	0.00366	25	-	-
Hummingbird		0.426	0.756	-	-	0.267	2.01	0.4	1.6
Hawkmoth		0.172*	0.251**	0.561	2.231	0.907	2.637	0.56	1.886

* The aerodynamic damping for hawkmoth is for pitch motion.

** The time delay for hawkmoth differs in proportional feedback (1) and derivative feedback (0.25).

Chapter 5

5 Bioinspired PD controller

5.1 Introduction

Flapping-wing insects achieve excellent flight control and maneuverability by continuously adjusting their wing kinematics under various unsteady environments. The unsteady external environment challenges the insects to maintain stable flight (Ravi, Kolomenskiy *et al.* 2016), let alone the maneuvers evading from predators or stimuli (Muijres, Elzinga *et al.* 2014) and tracking interested targets (Matthews and Sponberg 2018; Zhang, Hedrick *et al.* 2019). Moreover, the small body inertia renders the insects susceptible even to gentle unsteady currents. While it has been pointed out that flapping wing insects are dynamically unstable (Taylor and Thomas 2003; Sun and Xiong 2005; Sun, Wang *et al.* 2007; Xiong and Sun 2008), under the unfavourable conditions, insects enable achievements of high flight stability and maneuverability.

It is reported that insects are capable of correcting the flight deviations under disturbances within a very few wing beats (Ristroph, Bergou *et al.* 2010; Cheng, Deng *et al.* 2011; Beatus, Guckenheimer *et al.* 2015; Whitehead, Beatus *et al.* 2015), which outperforms any manmade air vehicles. Both vision-based and mechanical sensory systems are utilized in flight stabilization: the visual system like compound eyes or ocelli can sense the position and attitude; the highly specialized organs such as the halteres (Deora, Gundiah *et al.* 2017) and the antennas (Sane, Dieudonné *et al.* 2007) normally serve as vibrating structure gyroscopes capable of sensing body rotations, of which the sensory neurons are directly wired to the motor neurons (Fayyazuddin and Dickinson 1996), guaranteeing extremely low latency and fast control. Conventional studies (Ristroph, Bergou *et al.* 2010; Cheng, Deng *et al.* 2011; Beatus, Guckenheimer *et al.* 2015; Whitehead, Beatus *et al.* 2015) suggest the wide adaptation of proportional-derivative (PD) control among flying insects, where a proportional feedback is made for attitudes (roll, pitch and yaw) and positions (forward/backward, lateral and vertical) of insect body while a derivative feedback is for the time derivatives of their attitudes and positions. The flight control system of flying insects is observed to be inherently intermittent as recently pointed out by Xu et al (Xu, Nakata *et al.* 2020), however, a continuous PD controller can reasonably capture the behaviors in responds to perturbations (Ristroph, Bergou *et al.* 2010; Beatus, Guckenheimer *et al.* 2015; Whitehead, Beatus *et al.* 2015) and the PD control strategy has been reported to work well for the flapping-wing flight control in insects (Yao and Yeo 2020; Cai, Kolomenskiy *et al.* 2021).

Thus, flight stabilization can be achieved with some PD controller through adjusting the control parameters including both proportional and derivative gains so as to avoid the overdamped process or large overshoot oscillation and achieving a trimmed flight. Observation of the flight stabilization in insects indicates that PD flight strategies successfully developed can not only overcome the inherent dynamical instability but also achieve rapid stabilization through optimizing the control parameters. Determination of the correlations between wing kinematics and production of aerodynamic forces and torques (Hedrick and Daniel 2006; Yao and Yeo 2019) enables the development of insect-inspired flight controllers (Fei, Tu *et al.* 2019; Yao and Yeo 2019; Zhang, Hedrick *et al.* 2019). Zhang et al. (Zhang, Hedrick *et al.* 2019) performed a CFD-based modeling to determine the feasible control parameters through a fitting methodology. Yao and Yeo (Yao and Yeo 2019) applied a simplified aerodynamic model to derive the control parameters. However, how the control parameters are adjusted while optimized to achieve a flight control capable of fastest restoring remains yet poorly studied. To work out the optimized control parameters in a fast while precise way, we (Cai, Kolomenskiy *et al.* 2021) have recently successfully developed a novel method for the control parameter optimization by combing Laplace transformation and root locus method, which is established on the basis of a simplified flight dynamic model informed by high-fidelity CFD simulation, and thus guarantee the direct implementation of the control parameters to a CFD-based flight environment. This methodology provides a versatile and efficient tool to achieve fast and precise aerodynamical prediction for flying insects in various flight behaviors.

5.2 Longitudinal stabilization control for hovering bumblebee

5.2.1 Construction of longitudinal PD controller

Earlier studies of the correlation between the wing kinematics and production of aerodynamic forces and torques (Hedrick and Daniel 2006; Dickinson and Muijres 2016) have enabled the development of insect-inspired flight controllers (Fei, Tu *et al.* 2019; Yao and Yeo 2019; Zhang, Hedrick *et al.* 2019). Zhang, Hedrick *et al.* (2019) performed costly CFD simulations to find appropriate control parameters by trial and error. Yao and Yeo (2019) used a simplified aerodynamic model to derive the control parameters. However, when applied in CFD simulations, the parameters needed further adjustment.

Let us evaluate the predictive capability of CDAM from the standpoint of controller design. CDAM can reasonably predict the aerodynamic loads on the flying bumblebee with a variety of velocities and wing kinematics which makes it suitable for control purposes. We derive a proportional-derivative (PD) controller that effectively enforces longitudinal stability of the hovering bumblebee model. This methodology is applicable in forward flight. Here we apply it on the control to recover from a perturbed state (with slight forward, upward velocity and nose down pitch velocity) to hovering. The control model accounts for the sensorimotor latency. The control parameters are optimized by solving a dynamical system that encapsulates stability derivatives evaluated using CDAM. This significantly reduces the computation time compared with the trial-and-error method using CFD simulation. In addition, the optimized controller can be directly applied in CFD simulations because CDAM is consistent with the CFD by construction.

The flight dynamics of insects is governed by rather tedious differential equations (Sun, Wang *et al.* 2007; Wu, Zhang *et al.* 2009; Chang and Wang 2014; Bluman, Sridhar *et al.* 2018), if the time-accurate dynamics of flapping wings is included, see Section 2.6 and Appendix. However, bumblebees are heavy enough and their flapping frequency is large enough so that the fluctuation of inertial forces and torques during one period of wing beat does not influence the body dynamics on the time scale of about 10 wing beats representative of the recovery time of bumblebees after perturbation by strong wind gusts (Jakobi, Kolomenskiy *et al.* 2018). In this section, all the quantities are expressed in nondimensional form. Length, velocity, time, force, torque, mass, moment of inertia are nondimensionalized by c_m, U_{ref}, U_{ref}/c_m, $\rho c_m^2 U_{ref}^2$, $\rho c_m^3 U_{ref}^2$, ρc_m^3, ρc_m^5, respectively. We therefore simplify the dynamic equations (2.37) and (2.38) through cycle averaging the motion and neglecting the wing inertia of the bumblebee as a solid body,

$$m_t \, {}_g\dot{\bar{\boldsymbol{v}}} = {}_g\overline{\boldsymbol{F}}_{aero} + m_t \, {}_g\boldsymbol{g} \tag{5.1}$$

$$ {}_bI \, {}_b\dot{\bar{\boldsymbol{\omega}}} = {}_b\overline{\boldsymbol{M}}_{aero} \tag{5.2}$$

where ${}_g\dot{\bar{\boldsymbol{v}}}$ is the center of mass velocity in the ground frame of reference and ${}_b\dot{\bar{\boldsymbol{\omega}}}$ is the angular velocity of the body in its reference frame, dots denote time derivatives, m_t is the total mass of the bumblebee and ${}_bI$ is its moment of inertia. For the purpose of longitudinal control with small perturbation near hovering, the preceding equations further simplify as

$$\begin{pmatrix} {}_g\ddot{x} \\ {}_g\ddot{z} \\ \ddot{\chi} \end{pmatrix} = \begin{pmatrix} {}_g\tilde{F}_x \\ {}_g\tilde{F}_z - g \\ {}_b\widetilde{M}_y \end{pmatrix} \tag{5.3}$$

where ${}_g\tilde{F}_x = {}_g\bar{F}_{aero,x}/m_t$, ${}_g\tilde{F}_z = {}_g\bar{F}_{aero,z}/m_t$ and ${}_b\widetilde{M}_y = {}_b\bar{M}_{aero,y}/{}_bI_{yy}$ are the cycle averaged aerodynamic forces divided by the mass and the aerodynamic torque divided by the moment of inertia, respectively. As discussed in Sections 2, the cycle-averaged aerodynamic forces and torques can be accurately predicted by CDAM and they depend on the motion of the flying bumblebee and its wing kinematics. The wing motion should be controlled to maintain the hovering state. Here, we choose to vary the positional angle amplitude $\Delta\Phi$, the mean positional angle $\Delta\bar{\varphi}$ and the mean feathering angle $\Delta\bar{\eta}$ as control inputs, see Figure 5.1. Hence the quantities ${}_g\tilde{F}_x$, ${}_g\tilde{F}_z$ and ${}_b\widetilde{M}_y$ are treated as functions of 6 state variables,

$$\begin{aligned} {}_g\tilde{F}_x &= {}_g\tilde{F}_x({}_g\dot{x}, {}_g\dot{z}, \dot{\chi}, \Delta\Phi, \Delta\bar{\varphi}, \Delta\bar{\eta}) \\ {}_g\tilde{F}_z &= {}_g\tilde{F}_z({}_g\dot{x}, {}_g\dot{z}, \dot{\chi}, \Delta\Phi, \Delta\bar{\varphi}, \Delta\bar{\eta}) \\ {}_b\widetilde{M}_y &= {}_b\widetilde{M}_y({}_g\dot{x}, {}_g\dot{z}, \dot{\chi}, \Delta\Phi, \Delta\bar{\varphi}, \Delta\bar{\eta}) \end{aligned} \tag{5.4}$$

In hovering, $({}_g\tilde{F}_x, {}_g\tilde{F}_z, {}_b\widetilde{M}_y) = (0, g, 0)$. Considering small perturbation approximation around hovering, equation (5.4) can be approximated by the first order of its Taylor series expansion which, after substitution into equation (5.3), yields the governing dynamic equation near hovering,

$$\begin{pmatrix} {}_g\ddot{x} \\ {}_g\ddot{z} \\ \ddot{\chi} \end{pmatrix} = D \begin{pmatrix} {}_g\dot{x} \\ {}_g\dot{z} \\ \dot{\chi} \end{pmatrix} + W \begin{pmatrix} \Delta\Phi \\ \Delta\bar{\varphi} \\ \Delta\bar{\eta} \end{pmatrix} \tag{5.5}$$

where D is the passive aerodynamic damping matrix and W is the effect matrix describing the effect of wing kinematics on the acceleration of the bumblebee,

$$D = \left.\begin{pmatrix} \frac{\partial\, {}_g\tilde{F}_x}{\partial\, {}_g\dot{x}} & \frac{\partial\, {}_g\tilde{F}_x}{\partial\, {}_g\dot{z}} & \frac{\partial\, {}_g\tilde{F}_x}{\partial\dot{\chi}} \\ \frac{\partial\, {}_g\tilde{F}_z}{\partial\, {}_g\dot{x}} & \frac{\partial\, {}_g\tilde{F}_z}{\partial\, {}_g\dot{z}} & \frac{\partial\, {}_g\tilde{F}_z}{\partial\dot{\chi}} \\ \frac{\partial\, {}_b\widetilde{M}_y}{\partial\, {}_g\dot{x}} & \frac{\partial\, {}_b\widetilde{M}_y}{\partial\, {}_g\dot{z}} & \frac{\partial\, {}_b\widetilde{M}_y}{\partial\dot{\chi}} \end{pmatrix}\right|_0, \quad W = \left.\begin{pmatrix} \frac{\partial\, {}_g\tilde{F}_x}{\partial\Delta\Phi} & \frac{\partial\, {}_g\tilde{F}_x}{\partial\Delta\bar{\varphi}} & \frac{\partial\, {}_g\tilde{F}_x}{\partial\Delta\bar{\eta}} \\ \frac{\partial\, {}_g\tilde{F}_z}{\partial\Delta\Phi} & \frac{\partial\, {}_g\tilde{F}_z}{\partial\Delta\bar{\varphi}} & \frac{\partial\, {}_g\tilde{F}_z}{\partial\Delta\bar{\eta}} \\ \frac{\partial\, {}_b\widetilde{M}_y}{\partial\Delta\Phi} & \frac{\partial\, {}_b\widetilde{M}_y}{\partial\Delta\bar{\varphi}} & \frac{\partial\, {}_b\widetilde{M}_y}{\partial\Delta\bar{\eta}} \end{pmatrix}\right|_0 \tag{5.6}$$

Hedrick, Cheng *et al.* (2009) in a study of the rotational damping of a hummingbird emphasized the importance of flapping counter torque (FCT). More generally, the damping effects exist in all the six directions (forward/backward, vertical, lateral, yaw, pitch and roll) which are the diagonal elements of the damping matrix. In addition, the off-diagonal elements in D can be large as the motions in all directions are coupled. Cheng, Fry *et al.* (2010) studied fast turning maneuvers of fruit fly and pointed out that the passive aerodynamic damping due to FCT can account for a large part of the deceleration during saccades. Values of D and W can be directly obtained using CDAM with a finite difference method, for example, $\frac{\partial\ {}_g\tilde{F}_x}{\partial\ {}_g\dot{x}} \approx \frac{{}_g\tilde{F}_x(\delta\ {}_g\dot{x},0,0,0,0,0) - {}_g\tilde{F}_x(0,0,0,0,0,0)}{\delta\ {}_g\dot{x}}$, with a sufficiently small $\delta\ {}_g\dot{x}$.

For hovering of bumblebee with the wing kinematics as shown in Figure 2.2, D and W are expressed as follows

$$D = \begin{pmatrix} -4.47 & 2.28 & -5.99 \\ -0.15 & -9.37 & -0.69 \\ -10.7 & 3.62 & -31.2 \end{pmatrix} \times 10^{-4}, \qquad W = \begin{pmatrix} 0.29 & -0.45 & 6.55 \\ 7.71 & 0.00 & -1.24 \\ 1.66 & -7.36 & 9.84 \end{pmatrix} \times 10^{-4} \quad (5.7)$$

It can be seen from D that the pitch velocity has a significant effect on the forward/backward acceleration and, reversely, the forward/backward velocity also has an effect on the pitch acceleration. According to equation (5.5), the motion can be controlled by tuning the wing kinematics $\Delta\Phi$, , $\Delta\bar{\varphi}$ and $\Delta\bar{\eta}$. Inspection of the matrix W reveals that the forward/backward motion is mainly controlled by the mean feathering angle, vertical motion is mainly controlled by the amplitude of the positional angle, and the body pitching motion is sensitive to both the mean positional angle and the mean feathering angle. With an objective of implementing a practical control strategy that would enable our bumblebee model to maintain hovering, we first introduce a transformation matrix P which helps to decouple the dynamical system by diagonalizing the damping matrix

$$PDP^{-1} = \Lambda = \begin{pmatrix} \lambda_1 & 0 & 0 \\ 0 & \lambda_2 & 0 \\ 0 & 0 & \lambda_3 \end{pmatrix} \quad (5.8)$$

where

$$\lambda_1 = -3.2 \times 10^{-3}, \qquad \lambda_2 = -2.2 \times 10^{-4}, \qquad \lambda_3 = -9.1 \times 10^{-4} \quad (5.9)$$

and

$$P = \begin{pmatrix} -0.21 & -0.93 & 0.15 \\ 0.00 & 0.01 & -0.95 \\ -0.98 & 0.36 & -0.28 \end{pmatrix} \quad (5.10)$$

With a change of variables $(\xi_1, \xi_2, \xi_3)' = P\big({}_gx,\ {}_gz, \chi\big)'$, equation (5.5) takes the form

$$\begin{pmatrix} \ddot{\xi}_1 \\ \ddot{\xi}_2 \\ \ddot{\xi}_3 \end{pmatrix} = \begin{pmatrix} \lambda_1\dot{\xi}_1 \\ \lambda_2\dot{\xi}_2 \\ \lambda_3\dot{\xi}_3 \end{pmatrix} + \begin{pmatrix} \Delta p_1 \\ \Delta p_2 \\ \Delta p_3 \end{pmatrix} \quad (5.11)$$

where

$$\begin{pmatrix} \Delta p_1 \\ \Delta p_2 \\ \Delta p_3 \end{pmatrix} = PW \begin{pmatrix} \Delta\Phi \\ \Delta\bar{\varphi} \\ \Delta\bar{\eta} \end{pmatrix} \quad (5.12)$$

If, in addition, for any i ($i = 1,2,3$), Δp_i is set to be a function of ξ_i only, then the system is transformed from a MIMO (multi-input-multi-output) system into 3 SISO (single-input-single-output) systems.

It has been shown that insects exert control with a certain time delay (Dyhr, Morgansen *et al.* 2013). Here we set the time delay to be the period of one stroke cycle. The following PD feedback controller is adopted,

$$\Delta p_i(t) = -k_i\left[\xi_i(t-T) + \tau_i\dot{\xi}_i(t-T)\right] \quad i = 1,2,3 \tag{5.13}$$

After substituting (5.13) into (5.11), we obtain

$$\ddot{\xi}_i = \lambda_i\dot{\xi}_i - k_i\left[\xi_i(t-T) + \tau_i\dot{\xi}_i(t-T)\right] \quad i = 1,2,3 \tag{5.14}$$

The next step is to find the optimal control parameters k_i and τ_i that would guarantee the fast return to the equilibrium state. Following Section 4.3, we optimize the control parameters k_i and τ_i to minimize the closed-loop time constant, see Table 5.1 and the corresponding poles are summarized in Table 5.2. Combining (5.11) and (5.12) and using the definition of ξ_i, we obtain an explicit expression for the control strategy,

$$\begin{pmatrix}\Delta\Phi\\ \Delta\bar{\varphi}\\ \Delta\bar{\eta}\end{pmatrix} = -W^{-1}P^{-1}\begin{pmatrix}k_1 & 0 & 0\\ 0 & k_2 & 0\\ 0 & 0 & k_3\end{pmatrix}\left[P\begin{pmatrix}g^x\\ g^z\\ \chi\end{pmatrix} + \begin{pmatrix}\tau_1 & 0 & 0\\ 0 & \tau_2 & 0\\ 0 & 0 & \tau_3\end{pmatrix}P\begin{pmatrix}g^{\dot{x}}\\ g^{\dot{z}}\\ \dot{\chi}\end{pmatrix}\right] \tag{5.15}$$

5.2.2 Implementation of PD controller

Although the bumblebee processes various types muscles that function differently to each other (Lindsay, Sustar *et al.* 2017), they are normally activated once in one stroke cycle, so the PD controller is actually time-discrete, while the designed PD controller is time-continuous by construction. To this extent, there will be a gap between the desired wing kinematics for next stroke cycle and the current stroke cycle (Figure 5.2) by explicitly implementing the proposed PD controller, which is unrealistic. Here, we employ a smooth step function to create a transition of wing kinematics between the two successive stroke cycles with a transition time of $0.1T$, $s(x) = 6x^5 - 15x^4 + 10x^3$. This smooth step function ensures the continuity of the second derivative of the wing kinematics (Ebert, Musgrave *et al.* 2003). Hence, the wing kinematics during the transition period can be given as $f_{tran}(t) = \left(1 - s\left(\frac{t-nT}{0.1T}\right)\right)f_{cur}(t) + s\left(\frac{t-nT}{0.1T}\right)f_{des}(t)$, where $f_{cur}(t)$ is the current wing kinematics, $f_{des}(t)$ is the desired wing kinematics for next stroke cycle and f_{tran} is the transition wing kinematics.

5.2.3 Validation on the longitudinal PD controller

To evaluate the performance of the PD control strategy derived using CDAM, we integrate it into the CFD environment and compare the results with those in the CDAM environment with the governing time-accurate dynamic model proposed in Section 2.6 embedded. We first conduct system identification (Fei, Tu *et al.* 2019) to fine-tune the hovering wing kinematics for CDAM and for CFD. For the default hovering wing motion shown in Figure 2.2, CDAM and CFD produce slightly different values for the forces and torques. For that reason, free flight simulation with the default wing kinematics would slightly deviate from hovering in CDAM environment. To eliminate this deviation, the system identification is conducted by adding small offsets to the wing kinematics, i.e. positional amplitude offset ($\delta\Phi$), mean positional angle offset ($\delta\bar{\varphi}$) and mean feathering angle offset ($\delta\bar{\eta}$). The method to obtain the $\delta\Phi$, $\delta\bar{\varphi}$ and $\delta\bar{\eta}$ is the one adopted in 2.5.2 to find the trim state. The results are $\delta\Phi = -0.02$, $\delta\bar{\varphi} = 1.71$ degree, and $\delta\bar{\eta} = -0.6$ degree. Then, we apply the control strategy (5.15) in both CDAM and CFD environments, with the same values of control parameters. The bumblebee is set in an initial state with nose up motion: $\dot{\chi}(0) = 285.52$ degree/s, ${}_g\dot{x}(0) = 6.1$ mm/s, ${}_g\dot{z}(0) = 4.5$ mm/s, $\chi(0) = 45$ degrees, ${}_gx(0) = 0$ mm and ${}_gz(0) = 0$ mm. In the control process in the CFD environment, the bumblebee is fixed to flap its wings for three stroke cycles to make the surrounding flow fully developed. Then the bumblebee is released to perform free flying for one stroke cycle before applying active feedback PD control. In the control process in CDAM, the bumblebee is immediately released to perform free flying for one stroke cycle before activating the controls.

Figure 5.3 shows the time evolution of the position and pitch angle of the bumblebee during the recovery transition. It can be seen that the PD control strategy is successful in both the CDAM and the CFD environments. The maximal values of the forward/backward position deviation and pitch angle are similar in both environments. For the vertical position, the fluctuation amplitude in CFD is larger. Note that, in the position control, the deviation during the whole control process is smaller than the mean chord length (4.1 mm). At the same time, deviation of pitch angle is as large as 5 degrees.

It is difficult to know the exact time delay of one species. For instance, it is in the range of 2.6~6.7 ms for fruit flies' roll control (Beatus, Guckenheimer *et al.* 2015), 5~7.5 ms for blow flies (Hengstenberg, Sandeman *et al.* 1986). Here, we study the effect of time delay on the control parameters k, τ and thereby the closed-loop time constant. Figure 5.4a shows that both proportional gain and derivative gain decrease with increment of time delay. From Figure 5.4b, The closed-loop time constant rises with the increment of time delay linearly.

The consistency of the trends in the two environments demonstrate the effectiveness of the PD control strategy with the parameters determined using CDAM. This leads us to a twofold conclusion. Firstly, CDAM provides an effective tool for designing controllers that can then be used in more costly, but more predictive, CFD simulations. Secondly, to some extent, CDAM can successfully replace the CFD simulation to reduce the computation time. Other more complex control strategies like fuzzy control and reinforcement learning-based control can be designed with the aid of CDAM, which may be a promising perspective for the future work.

5.3 Full six-degree-of-freedom stabilization control for hovering bumblebee

5.3.1 Construction of 6 DoF PD controller

It is worth noting that the disturbances in nature can induces the deviations along all the six degree of freedoms (rotation and translation). However, up to now, the PD-based algorithms have been only applied to examine specific single degree of freedom (DoF) and/or 3 DoF flight control associated with insect flights (Zhang and Liu 2018; Cai, Kolomenskiy *et al.* 2021), a full 6 DoF flight control strategy remains yet poorly studied. In addition, biological evidence (Fayyazuddin and Dickinson 1996; Ristroph, Bergou *et al.* 2010; Beatus, Guckenheimer *et al.* 2015; Whitehead, Beatus *et al.* 2015) reveals the implementation of PD control strategy to attitudes control, while whether such strategy is applicable to 3 DOF position control remains unclear. In this study, we make an extension to study the control of flight stabilization in bumblebee by further proposing a full 6 DoF control strategy. Based on the observation that (Windsor, Bomphrey *et al.* 2014) that the forward/backward and lateral motions are highly correlated with pitch and roll angle, respectively, here we propose a hierarchical 6 DoF PD controller accounting for time latency, of which the vertical, yaw, pitch and roll motion are simultaneously controlled by tuning the wing motion while the forward/backward and lateral motions are controlled by control the pitch and roll motion.

As shown in Figure 5.5*a* and *b*, pitch down/up can tilt the force forward/backward and roll can tilt the force sideward. In addition, experiments of flight behaviors of hawkmoth predict that roll angle feedback is needed to stabilize the lateral dynamics, and that a combination of pitch angle and pitch rate feedback is most effective in stabilizing the longitudinal dynamics (Windsor, Bomphrey *et al.* 2014), therefore in this study, we control the forward/backward position and lateral position by adjusting the pitch and roll angles. Except the forward/backward and lateral freedoms, the remaining 4 degrees of freedom point to the vertical position, yaw angle, pitch angle and roll angle, respectively, which are controlled by tuning the wing kinematics. Here, we choose the positional angle amplitude ($\varPhi$), the mean positional angle ($\bar{\varphi}$), the difference of positional angle between right and left wings ($\varPhi_{RL}$), and the difference of mean feathering angle between right and left wings ($\bar{\eta}_{RL}$) as the tunable wing kinematics (Figure 5.5*c~f*). It should be noted that for the hovering state, the pith angle is $\frac{\pi}{4}$, thus the angular velocities and the body angle are coupled

$$\begin{pmatrix} {}_b\omega_x \\ {}_b\omega_y \\ {}_b\omega_z \end{pmatrix} = \begin{pmatrix} \dot{\rho} - \dfrac{\dot{\psi}}{\sqrt{2}} \\ \dot{\chi} \\ \dfrac{\dot{\psi}}{\sqrt{2}} \end{pmatrix} \tag{5.16}$$

Therefore, for small perturbations at hovering or very low flight velocities, equations (5.1) and (5.2) can be linearized as,

$$\begin{pmatrix} {}_g\ddot{x} \\ {}_g\ddot{y} \\ {}_g\ddot{z} \\ \ddot{\rho} - \dfrac{\ddot{\psi}}{\sqrt{2}} \\ \ddot{\chi} \\ \dfrac{\ddot{\psi}}{\sqrt{2}} \end{pmatrix} = \begin{pmatrix} {}_g\tilde{F}_x \\ {}_g\tilde{F}_y \\ {}_g\tilde{F}_z - g \\ {}_b\widetilde{M}_x \\ {}_b\widetilde{M}_y \\ {}_b\widetilde{M}_z \end{pmatrix} \tag{5.17}$$

The aerodynamic forces and torques are functions of the body motion (${}_g\dot{x}$, ${}_g\dot{y}$, ${}_gz$, $\dot{\rho} - \frac{\dot{\psi}}{\sqrt{2}}$, $\dot{\chi}$, $\frac{\dot{\psi}}{\sqrt{2}}$), the variation of wing kinematics ($\Delta\varPhi$, $\overline{\Delta\varphi}$, $\Delta\varPhi_{RL}$, $\Delta\bar{\eta}_{RL}$) and the variation of body attitude ($\Delta\chi$,$\Delta\rho$). Because the pitch angle is selected to control the forward/backward position, we assume that the forward/backward force is mainly affected by the forward/backward velocity and pitch angle, thus the dynamics of forward/backward motion can be simplified as

$${}_g\ddot{x} = {}_g\tilde{F}_x\left({}_g\dot{x}, \Delta\chi\right) \tag{5.18}$$

The roll angle is selected to control the lateral position, and thus we assume that the lateral force is mostly affected by the lateral velocity and roll angle, resulting in the body dynamics of lateral motion as,

$${}_g\ddot{y} = {}_g\tilde{F}_y\left({}_g\dot{y}, \Delta\rho\right) \tag{5.19}$$

We utilize the variation of wing kinematics ($\Delta\varPhi$, $\Delta\varphi_m$, $\Delta\varPhi_{RL}$, $\Delta\eta_{m,RL}$) to control the vertical position, yaw angle, pitch angle and roll angle, while ignoring the effects of the degrees of freedom due to forward/backward and lateral position, and thus the dynamics of vertical, yaw, pitch and roll motions can be simplified as

$$\begin{pmatrix} {}_{g}\ddot{z} \\ \ddot{\rho}-\frac{\ddot{\psi}}{\sqrt{2}} \\ \ddot{\chi} \\ \frac{\ddot{\psi}}{\sqrt{2}} \end{pmatrix} = \begin{pmatrix} {}_{g}\tilde{F}_{z}\left({}_{g}\dot{z},\dot{\rho}-\frac{\dot{\psi}}{\sqrt{2}},\dot{\chi},\frac{\dot{\psi}}{\sqrt{2}},\Delta\Phi,\Delta\bar{\varphi},\Delta\Phi_{RL},\Delta\bar{\eta}_{RL}\right) \\ {}_{b}\widetilde{M}_{x}\left({}_{g}\dot{z},\dot{\rho}-\frac{\dot{\psi}}{\sqrt{2}},\dot{\chi},\frac{\dot{\psi}}{\sqrt{2}},\Delta\Phi,\Delta\bar{\varphi},\Delta\Phi_{RL},\Delta\bar{\eta}_{RL}\right) \\ {}_{b}\widetilde{M}_{y}\left({}_{g}\dot{z},\dot{\rho}-\frac{\dot{\psi}}{\sqrt{2}},\dot{\chi},\frac{\dot{\psi}}{\sqrt{2}},\Delta\Phi,\Delta\bar{\varphi},\Delta\Phi_{RL},\Delta\bar{\eta}_{RL}\right) \\ {}_{b}\widetilde{M}_{z}\left({}_{g}\dot{z},\dot{\rho}-\frac{\dot{\psi}}{\sqrt{2}},\dot{\chi},\frac{\dot{\psi}}{\sqrt{2}},\Delta\Phi,\Delta\bar{\varphi},\Delta\Phi_{RL},\Delta\bar{\eta}_{RL}\right) \end{pmatrix} \tag{5.20}$$

For small perturbations, the aerodynamic forces and torques can be further approximated by the first order of Taylor expansions such as:

$${}_{g}\ddot{x} = \frac{\partial\, {}_{g}\tilde{F}_{x}}{\partial\, {}_{g}\dot{x}}\, {}_{g}\dot{x} + \frac{\partial\, {}_{g}\tilde{F}_{x}}{\partial\Delta\chi}\Delta\chi \tag{5.21}$$

$${}_{g}\ddot{y} = \frac{\partial\, {}_{g}\tilde{F}_{y}}{\partial\, {}_{g}\dot{y}}\, {}_{g}\dot{y} + \frac{\partial\, {}_{g}\tilde{F}_{y}}{\partial\Delta\rho}\Delta\rho \tag{5.22}$$

$$\begin{pmatrix} {}_{g}\ddot{z} \\ \ddot{\rho}-\frac{\ddot{\psi}}{\sqrt{2}} \\ \ddot{\chi} \\ \frac{\ddot{\psi}}{\sqrt{2}} \end{pmatrix} = \begin{pmatrix} \frac{\partial\, {}_{g}\tilde{F}_z}{\partial\, {}_{g}\dot{z}} & \frac{\partial\, {}_{g}\tilde{F}_z}{\partial\left(\dot{\rho}-\frac{\dot{\psi}}{\sqrt{2}}\right)} & \frac{\partial\, {}_{g}\tilde{F}_z}{\partial\, \dot{\chi}} & \frac{\partial\, {}_{g}\tilde{F}_z}{\partial \frac{\dot{\psi}}{\sqrt{2}}} \\ \frac{\partial\, {}_{b}\tilde{M}_x}{\partial\, {}_{g}\dot{z}} & \frac{\partial\, {}_{b}\tilde{M}_x}{\partial\left(\dot{\rho}-\frac{\dot{\psi}}{\sqrt{2}}\right)} & \frac{\partial\, {}_{b}\tilde{M}_x}{\partial\, \dot{\chi}} & \frac{\partial\, {}_{b}\tilde{M}_x}{\partial \frac{\dot{\psi}}{\sqrt{2}}} \\ \frac{\partial\, {}_{b}\tilde{M}_y}{\partial\, {}_{g}\dot{z}} & \frac{\partial\, {}_{b}\tilde{M}_y}{\partial\left(\dot{\rho}-\frac{\dot{\psi}}{\sqrt{2}}\right)} & \frac{\partial\, {}_{b}\tilde{M}_y}{\partial\, \dot{\chi}} & \frac{\partial\, {}_{b}\tilde{M}_y}{\partial \frac{\dot{\psi}}{\sqrt{2}}} \\ \frac{\partial\, {}_{b}\tilde{M}_z}{\partial\, {}_{g}\dot{z}} & \frac{\partial\, {}_{b}\tilde{M}_z}{\partial\left(\dot{\rho}-\frac{\dot{\psi}}{\sqrt{2}}\right)} & \frac{\partial\, {}_{b}\tilde{M}_z}{\partial\, \dot{\chi}} & \frac{\partial\, {}_{b}\tilde{M}_z}{\partial \frac{\dot{\psi}}{\sqrt{2}}} \end{pmatrix} \begin{pmatrix} {}_{g}\dot{z} \\ \dot{\rho}-\frac{\dot{\psi}}{\sqrt{2}} \\ \dot{\chi} \\ \frac{\dot{\psi}}{\sqrt{2}} \end{pmatrix}$$

$$+ \begin{pmatrix} \frac{\partial\, {}_{g}\tilde{F}_z}{\partial \Delta\Phi} & \frac{\partial\, {}_{g}\tilde{F}_z}{\partial \Delta\bar{\varphi}} & \frac{\partial\, {}_{g}\tilde{F}_z}{\partial \Delta\Phi_{RL}} & \frac{\partial\, {}_{g}\tilde{F}_z}{\partial \Delta\bar{\eta}_{RL}} \\ \frac{\partial\, {}_{b}\tilde{M}_x}{\partial \Delta\Phi} & \frac{\partial\, {}_{b}\tilde{M}_x}{\partial \Delta\bar{\varphi}} & \frac{\partial\, {}_{b}\tilde{M}_x}{\partial \Delta\Phi_{RL}} & \frac{\partial\, {}_{b}\tilde{M}_x}{\partial \Delta\bar{\eta}_{RL}} \\ \frac{\partial\, {}_{b}\tilde{M}_y}{\partial \Delta\Phi} & \frac{\partial\, {}_{b}\tilde{M}_y}{\partial \Delta\bar{\varphi}} & \frac{\partial\, {}_{b}\tilde{M}_y}{\partial \Delta\Phi_{RL}} & \frac{\partial\, {}_{b}\tilde{M}_y}{\partial \Delta\bar{\eta}_{RL}} \\ \frac{\partial\, {}_{b}\tilde{M}_z}{\partial \Delta\Phi} & \frac{\partial\, {}_{b}\tilde{M}_z}{\partial \Delta\bar{\varphi}} & \frac{\partial\, {}_{b}\tilde{M}_z}{\partial \Delta\Phi_{RL}} & \frac{\partial\, {}_{b}\tilde{M}_z}{\partial \Delta\bar{\eta}_{RL}} \end{pmatrix} \begin{pmatrix} \Delta\Phi \\ \Delta\bar{\varphi} \\ \Delta\Phi_{RL} \\ \Delta\bar{\eta}_{RL} \end{pmatrix}$$

$$\equiv D \begin{pmatrix} {}_{g}\dot{z} \\ \dot{\rho}-\frac{\dot{\psi}}{\sqrt{2}} \\ \dot{\chi} \\ \frac{\dot{\psi}}{\sqrt{2}} \end{pmatrix} + W \begin{pmatrix} \Delta\Phi \\ \Delta\bar{\varphi} \\ \Delta\Phi_{RL} \\ \Delta\bar{\eta}_{RL} \end{pmatrix} \tag{5.23}$$

These coefficients can be directly obtained by using the CDAM method with a finite difference method, for instance, $\frac{\partial\, {}_{g}\tilde{F}_z}{\partial\, {}_{g}\dot{z}} \approx \frac{{}_{g}\tilde{F}_z(\delta\, {}_{g}\dot{z},0,0,0,0,0,0,0) - {}_{g}\tilde{F}_z(0,0,0,0,0,0,0,0)}{\delta\, {}_{g}\dot{z}}$, with a sufficiently small $\delta\, {}_{g}\dot{z}$, such as

$$\frac{\partial\, {}_{g}\tilde{F}_x}{\partial\, {}_{g}\dot{x}} = 22.8 \times 10^{-4}, \qquad \frac{\partial\, {}_{g}\tilde{F}_x}{\partial \Delta\chi} = -4.48 \times 10^{-4}$$

$$\frac{\partial\, {}_{g}\tilde{F}_y}{\partial\, {}_{g}\dot{y}} = -16.1 \times 10^{-4}, \qquad \frac{\partial\, {}_{g}\tilde{F}_y}{\partial \Delta\rho} = -5.08 \times 10^{-4}$$

$$D=\begin{pmatrix}-2.39 & 1.43 & -0.688 & 1.56\\ 0 & -249 & 0 & -38\\ 3.62 & 0.803 & -31.2 & 0.428\\ 0 & -32.0 & 0 & -80.7\end{pmatrix}\times 10^{-4},$$

$$W=\begin{pmatrix}7.74 & 0 & 0.0916 & -0.243\\ 0 & 0 & 17.5 & 31.3\\ 1.66 & -7.36 & 0.0655 & -0.0495\\ 0 & 0 & 4.29 & -6.76\end{pmatrix}\times 10^{-4}$$

We then focus on the controller design on vertical position and three body angles (yaw, pitch and roll) assuming a time delay of one stroke cycle of the bumblebee. Following the analytical framework in Section 5.2.1 (Cai, Kolomenskiy *et al.* 2021), we first decouple the dynamic system (5.23) by introducing a transformation matrix P which diagonalizes D

$$PDP^{-1}=\Lambda=\begin{pmatrix}\lambda_1 & 0 & 0 & 0\\ 0 & \lambda_2 & 0 & 0\\ 0 & 0 & \lambda_3 & 0\\ 0 & 0 & 0 & \lambda_4\end{pmatrix} \tag{5.24}$$

where

$$\lambda_1=-2.47\times 10^{-3},\qquad \lambda_2=-3.11\times 10^{-3},\qquad \lambda_3=-2.56\times 10^{-2},$$
$$\lambda_4=-7.38\times 10^{-3}$$

and

$$P=\begin{pmatrix}1.01 & 0 & -0.02 & 0.02\\ 0.13 & 0 & -1.00 & 0\\ 0 & 0.98 & 0 & 0.21\\ 0 & 0.18 & 0 & -0.98\end{pmatrix}$$

With a change of variables $(\xi_1,\xi_2,\xi_3,\xi_4)'=P\left({}_gz,\rho-\frac{\psi}{\sqrt{2}},\chi,\frac{\psi}{\sqrt{2}}\right)'$, equation (5.23) takes the form

$$\begin{pmatrix}\ddot{\xi}_1\\ \ddot{\xi}_2\\ \ddot{\xi}_3\\ \ddot{\xi}_4\end{pmatrix}=\begin{pmatrix}\lambda_1\dot{\xi}_1\\ \lambda_2\dot{\xi}_2\\ \lambda_3\dot{\xi}_3\\ \lambda_4\dot{\xi}_4\end{pmatrix}+\begin{pmatrix}\Delta p_1\\ \Delta p_2\\ \Delta p_3\\ \Delta p_4\end{pmatrix} \tag{5.25}$$

where

$$\begin{pmatrix}\Delta p_1\\ \Delta p_2\\ \Delta p_3\\ \Delta p_4\end{pmatrix}=PW\begin{pmatrix}\Delta\Phi\\ \Delta\bar{\varphi}\\ \Delta\Phi_{RL}\\ \Delta\bar{\eta}_{RL}\end{pmatrix} \tag{5.26}$$

Δp_i $(i=1,2,3,4)$ is set to be the function of ξ_i only, then the system is transformed from a MIMO (multi-input-multi-output) system into 4 SISO (single-input-single-output) systems. The PD controller with a time delay of one stroke cycle is then adopted,

$$\Delta p_i = -k_i\left[\xi_i(t-T) + \tau_i\dot{\xi}_i(t-T)\right] \tag{5.27}$$

After substituting (5.27) into (5.25), we obtain

$$\ddot{\xi}_i = \lambda_i\dot{\xi}_i - k_i\left[\xi_i(t-T) + \tau_i\dot{\xi}_i(t-T)\right] \tag{5.28}$$

By applying the Laplace transformation and root locus method under the principle maximizing the negative poles to achieve fast control (Cai, Kolomenskiy *et al.* 2021), we obtain the optimal control parameters k_i and τ_i, see Table 5.3.

For small perturbation, the proportional feedback can be directly obtained by integrating equation (5.16) over time. Combining (5.26), (5.27), we can obtain the PD controller (direct controller) for vertical, yaw, pitch and roll motions, such as

$$\begin{pmatrix} \Delta\Phi \\ \Delta\bar{\varphi} \\ \Delta\Phi_{RL} \\ \Delta\bar{\eta}_{RL} \end{pmatrix} = -W^{-1}P^{-1}\begin{pmatrix} k_1 & 0 & 0 & 0 \\ 0 & k_2 & 0 & 0 \\ 0 & 0 & k_3 & 0 \\ 0 & 0 & 0 & k_4 \end{pmatrix} \cdot \left[P\begin{pmatrix} z \\ \rho - \frac{\psi}{\sqrt{2}} - \rho_y \\ \chi - \frac{\pi}{4} - \chi_x \\ \frac{\psi}{\sqrt{2}} \end{pmatrix} + \begin{pmatrix} \tau_1 & 0 & 0 & 0 \\ 0 & \tau_2 & 0 & 0 \\ 0 & 0 & \tau_3 & 0 \\ 0 & 0 & 0 & \tau_4 \end{pmatrix}\begin{pmatrix} \dot{z} \\ \dot{\rho} - \frac{\dot{\psi}}{\sqrt{2}} \\ \dot{\chi} \\ \frac{\dot{\psi}}{\sqrt{2}} \end{pmatrix} \right] \tag{5.29}$$

where ρ_y is the desired roll angle to control lateral position, and χ_x the desired pitch angle to control forward/backward position, respectively. Because it takes up to 4 stroke cycles to reach an approximately stable and desired body angles (yaw, pitch and roll), we thus take account for a latency of 2 stroke cycles of roll and pitch on controlling lateral position and forward/backward position, which (indirect controller) are given as,

$$a_x(t) = \frac{\partial F_x}{\partial v_x}v_x(t) + \frac{\partial F_x}{\partial \chi}\chi(t-2T), \tag{5.30}$$

$$a_y(t) = \frac{\partial F_y}{\partial v_y}v_y(t) + \frac{\partial F_y}{\partial \rho}\rho(t-2T) \tag{5.31}$$

Similarly, the PD controller for lateral and forward/backward motions can be obtained as

$$\begin{aligned} \chi_x &= -k_x(x + \tau_x\dot{x}) \\ \rho_y &= -k_y\left(y + \tau_y\dot{y}\right) \end{aligned} \tag{5.32}$$

The values of the control parameters are summarized in Table 5.3. In general, the hierarchical PD controller consists of a direct controller (equation (5.29)) and an indirect controller (equation (5.32)). The indirect controller determines the desired pitch and roll angles while the direct controller determines the desired wing kinematics. Figure 5.6 shows the closed-loop flight dynamic system of the bumblebee.

5.3.2 Stabilization control under small perturbations

Firstly, we examine the flight stabilization based on the proposed PD controller under small perturbations. Figure 5.7 illustrates the trimmed state of a hovering bumblebee up to 100 stroke cycles (~0.7s), which reaches a stable periodic state after several stroke cycles; even with an initial state deviating slightly from the hovering state, obviously the flight can be stabilized effectively by the PD controller. With the symmetric wing kinematics of left- and right wing (Figure 2.2), the reciprocation motion of flapping wings induces a slight body oscillation in the longitudinal motions involving forward- and backward-motion, vertical motion and pitch motion.

We then apply velocity perturbations to the hovering state along the three directions (*x, y, z*), which lead to some deviations associated with body attitudes in three body positions and three rotational angles (Figure 5.8 and Figure 5.9). The velocity disturbance is about 0.03 m/s (0.025 U_{ref}) and the angular velocity 5 rad/s. All the perturbation-induced deviations are successfully corrected by the PD controller. The longitudinal motions are observed to be highly coupled: the forward/backward perturbation can result in pitch-deviation while the vertical perturbation can induce forward/backward and pitch deviations. This is also observed in the sideways motions of lateral motion, yaw and roll motions, that the lateral perturbation leads to yaw and roll deviations. Particularly, the time evolutions of yaw and roll are almost synchronous (Figure 5.8*b*, Figure 5.9*a* and *c*), indicating some strong coupling between yaw and roll motions. On the other hand, the longitudinal motions and sideways motions are likely to be decoupled as also reported in previous studies (Yao and Yeo 2019; Yao and Yeo 2020) that deal with the flight control in terms of longitudinal and sideways control separately. This trend is also seen in the flight stabilization under small angular velocity perturbations (Figure 5.9). The variations of wing motion during the stabilization are relatively small compared to their amplitudes except for the stabilization under vertical perturbation. While the PD control strategy has been proposed and proven to be effective in modelling some single DoF control in concern with various insect flights (Cheng, Deng *et al.* 2011; Ristroph, Ristroph *et al.* 2013; Beatus, Guckenheimer *et al.* 2015; Whitehead, Beatus *et al.* 2015), our recent studies have further examined its capability in modeling 3 DoF body attitude control in terms of yaw, pitch, and roll (Zhang and Liu 2018) and longitudinal control (Cai, Kolomenskiy *et al.* 2021). In this study, our results demonstrate that the PD control strategy is also feasible in achieving a full 6 DoF body control in insect flights under small perturbations.

Furthermore, the 6 DoF PD controller-based flight stabilization shows a feature that the stabilization associated with the vertical motion and three body rotations of yaw, pitch and roll can be achieved very fast within 10 stroke cycles (0.07s), which is also observed in our previous study of 3DoF attitude control and longitudinal control (Zhang and Liu 2018; Cai, Kolomenskiy *et al.* 2021) and supported by the previous biological evidences of several different insect species (Ristroph, Bergou *et al.* 2010; Cheng, Deng *et al.* 2011; Ristroph, Ristroph *et al.* 2013; Beatus, Guckenheimer *et al.* 2015; Whitehead, Beatus *et al.* 2015). This implies that the fast-stabilization observed in the single and/or 3DoF PD controls can remain the same feature in the 6DoF PD-based control. On the contrary, the flight stabilization along forward/backward and lateral motions is comparatively much slower, showing slight overshoots and turning out to be stable up to more than 50 stroke cycles (Figure 5.8, Figure 5.9). This is mainly because the forward/backward and lateral motions are here controlled in terms of pitch- and roll-control, which lead to relatively some large time delays, i.e., latencies. The forward/backward motion however can be controlled directly by adjusting the wing motions to achieve a faster stabilization, with a longitudinal PD controller as proposed by Cai, Kolomenskiy *et al.* (2021). Since it is of the most importance for a flying insect to stabilize its body attitude in terms of yaw, pitch and roll rotations under any disturbances (Jakobi, Kolomenskiy *et al.* 2018), a relatively slower stabilization on body positions may not essentially dominate its flight stabilization. Moreover, the current 6 DoF PD controller that is proven to be effective in 6 DoF body control in insect flights requires merely 4 direct alternations of wing kinematics, which is of great potential to simplify the flight controller design and related actuator-based fabrication in flapping-wing MAVs. This will be investigated in our future work as an application in insect-inspired flapping MAVs.

5.3.3 Flight stabilization with large perturbations

For the 6 DoF PD controller designed for flight stabilization under small perturbations, we assumed that the fluctuations of the inertial and aerodynamic forces can be neglected with a time-averaged body dynamic model. Thus, the PD controller is time-continuous rather than discrete in terms of the time interval of a wing stroke and given the small perturbations the body dynamic model can be linearized. Albeit with the assumptions, the effectiveness of the 6 DoF PD controller on the small perturbation is validated in Section 5.3.2. In nature, however, any wind gusts even with rather slight disturbances can impact largely on the tiny insect body (Ravi, Crall *et al.* 2013; Beatus, Guckenheimer *et al.* 2015). Here we further examine the capability of the PD controller proposed on whether or not it still works even for large perturbations. We investigate the variation and response of three body positions and three rotational angles associated with flight stabilization in bumblebee, simply through amplifying the perturbations by 10 times. As illustrated in Figure 5.10 and Figure 5.11, time courses of the body positions and attitudes under large velocity and angular velocity perturbations indicate that the 6DoF PD controller proposed here still works well in dealing with the flight stabilization under large perturbations, i.e., even crucial wind gust-induced disturbances. Due to the morphological limits of the flapping wings, e.g. the two wings ca not penetrate each other and the amplitudes of positional angle should be positive, we set the constraints that the minimal and maximal positional angle amplitudes are 0.1 and 1.2 of the hovering one, the maximal deviation of mean positional angle is 20 degrees.

Interestingly, the highly coupled feature associated with the longitudinal motions is also observed here under large perturbations as that under small perturbations except for the vertical velocity perturbations. Under a large initial upward velocity perturbation (Figure 5.10*c*), a backward deviation is induced opposite to that under small perturbation, which can be explained by the pitch response of the bumblebee, which pitches up under large upward perturbation but pitches down under small perturbations. As illustrated in Figure 5.5*a*, a pitch up causes a backward motion while a pitch down a forward motion. In addition, because of the largely induced pitch deviation, the forward/backward deviation even turns out to be greater than the vertical deviation. This however never occurs in the case of small perturbations. Under large perturbations, the sideways motions can also affect the longitudinal motions, for instance, under a large angular perturbation along ${}_bz$, the pitch motion displays a remarked variation (Figure 5.11*a*). Compared to small perturbations, the dynamic response of hovering bumblebee under large perturbations behaves differently and the coupling among different degrees of freedoms shows much complicated while highly nonlinear feature. Nevertheless, the PD controller proposed is very likely to be capable of effectively stabilizing the complex flight as it does under small perturbations.

It should be noted that for extremely large perturbation such as turning several circles the angular displacement should be modified because an additional entire circle actually does not affect the flying state (Beatus, Guckenheimer *et al.* 2015). For insects, the proportional feedback is normally integrated from derivative feedback which could induce integral error for long-time flight and extremely large perturbations, so it is necessary to adopt the visual system to compensate such errors (Whitehead, Beatus *et al.* 2015).

In addition, although maintaining stable body attitudes in flight is the primary objective for insects to stay airborne, remaining still at a specific position is also an important mission such as for pollinating flowers (Matthews and Sponberg 2018). This can be achieved by introducing a time integral of body positions, and thus a PID controller is normally employed

(Fei, Tu *et al.* 2019; Yao and Yeo 2019; Yao and Yeo 2020). A complicated control strategy trained by deep reinforcement learning can be an alternative effective tool (Fei, Tu *et al.* 2019). However, whether the PD control strategy for body attitude control is applicable to the position control has been poorly studied (Ma, Chirarattananon *et al.* 2013). In insect flights, the attitude feedback can be detected by mechanosensory organs like halteres and antenna while visual systems are necessary to capture the body-position feedback. It is found that the sustained visual depolarization is transformed into a temporally structured train of action potentials synchronized to the haltere beating movements (Huston and Krapp 2009), indicating that the position feedback can be fused with attitude feedback to inform the PD control strategy. Such locomotion (flight mode and flight route) control such as following a moving target while locomoting to another location is essentially of great importance for point-point flight control in both bio-flyers and flying robots, and thus whether the 6DoF PD control strategy proposed here can be a feasible flight controller will be studied in our future research.

References

Beatus, T., Guckenheimer, J. M., Cohen, I., Controlling Roll Perturbations in Fruit Flies, Journal of the Royal Society Interface, Vol. 12, No. 105 (2015),pp. 20150075.

Bluman, J. E., Sridhar, M. K., Kang, C.-k., Chordwise Wing Flexibility May Passively Stabilize Hovering Insects, Journal of the Royal Society Interface, Vol. 15, No. 147 (2018),pp. 20180409.

Cai, X., Kolomenskiy, D., Nakata, T., Liu, H., A Cfd Data-Driven Aerodynamic Model for Fast and Precise Prediction of Flapping Aerodynamics in Various Flight Velocities, Journal of Fluid Mechanics, Vol. 915, No. (2021),pp. A114.

Chang, S., Wang, Z. J., Predicting Fruit Fly's Sensing Rate with Insect Flight Simulations, Proceedings of the National Academy of Sciences, Vol. 111, No. 31 (2014),pp. 11246.

Cheng, B., Deng, X., Hedrick, T. L., The Mechanics and Control of Pitching Manoeuvres in a Freely Flying Hawkmoth (*Manduca Sexta*), Journal of Experimental Biology, Vol. 214, No. 24 (2011),pp. 4092.

Cheng, B., Fry, S. N., Huang, Q., Deng, X., Aerodynamic Damping During Rapid Flight Maneuvers in the Fruit Fly Drosophila, Journal of Experimental Biology, Vol. 213, No. 4 (2010),pp. 602-612.

Deora, T., Gundiah, N., Sane, S. P., Mechanics of the Thorax in Flies, Journal of Experimental Biology, Vol. 220, No. 8 (2017),pp. 1382.

Dickinson, M. H., Muijres, F. T., The Aerodynamics and Control of Free Flight Manoeuvres in Drosophila, Philosophical Transactions of the Royal Society B: Biological Sciences, Vol. 371, No. 1704 (2016),pp. 20150388.

Dyhr, J. P., Morgansen, K. A., Daniel, T. L., Cowan, N. J., Flexible Strategies for Flight Control: An Active Role for the Abdomen, The Journal of Experimental Biology, Vol. 216, No. 9 (2013),pp. 1523.

Ebert, D. S., Musgrave, F. K., Peachey, D., Perlin, K., Hart, J. C., Worley, S., Texturing & Modeling: A Procedural Approach, Morgan Kaufmann (2003)

Fayyazuddin, A., Dickinson, M. H., Haltere Afferents Provide Direct, Electrotonic Input to a Steering Motor Neuron in the Blowfly, *Calliphora*, Journal of Neuroscience, Vol. 16, No. 16 (1996),pp. 5225.

Fei, F., Tu, Z., Yang, Y., Zhang, J., Deng, X. Flappy Hummingbird: An Open Source Dynamic Simulation of Flapping Wing Robots and Animals. 2019 International Conference on Robotics and Automation (ICRA), IEEE, 2019

Fei, F., Tu, Z., Zhang, J., Deng, X. Learning Extreme Hummingbird Maneuvers on Flapping Wing Robots. 2019 International Conference on Robotics and Automation (ICRA), 2019

Hedrick, T. L., Cheng, B., Deng, X., Wingbeat Time and the Scaling of Passive Rotational Damping in Flapping Flight, Science, Vol. 324, No. 5924 (2009),pp. 252.

Hedrick, T. L., Daniel, T. L., Flight Control in the Hawkmoth *Manduca Sexta*: The Inverse Problem of Hovering, The Journal of Experimental Biology, Vol. 209, No. 16 (2006),pp. 3114.

Hengstenberg, R., Sandeman, D. C., Hengstenberg, B., Horridge, G. A., Compensatory Head Roll in the Blowfly Calliphora During Flight, Proceedings of the Royal Society of London. Series B. Biological Sciences, Vol. 227, No. 1249 (1986),pp. 455-482.

Huston, S. J., Krapp, H. G., Nonlinear Integration of Visual and Haltere Inputs in Fly Neck Motor Neurons, The Journal of Neuroscience, Vol. 29, No. 42 (2009),pp. 13097.

Jakobi, T., Kolomenskiy, D., Ikeda, T., Watkins, S., Fisher, A., Liu, H., Ravi, S., Bees with Attitude: The Effects of Directed Gusts on Flight Trajectories, Biology Open, Vol. 7, No. 10 (2018),pp. bio034074.

Lindsay, T., Sustar, A., Dickinson, M., The Function and Organization of the Motor System Controlling Flight Maneuvers in Flies, Current Biology, Vol. 27, No. 3 (2017),pp. 345-358.

Ma, K. Y., Chirarattananon, P., Fuller, S. B., Wood, R. J., Controlled Flight of a Biologically Inspired, Insect-Scale Robot, Science, Vol. 340, No. 6132 (2013),pp. 603.

Matthews, M., Sponberg, S., Hawkmoth Flight in the Unsteady Wakes of Flowers, The Journal of Experimental Biology, Vol. 221, No. 22 (2018),pp. jeb179259.

Muijres, F. T., Elzinga, M. J., Melis, J. M., Dickinson, M. H., Flies Evade Looming Targets by Executing Rapid Visually Directed Banked Turns, Science, Vol. 344, No. 6180 (2014),pp. 172.

Ravi, S., Crall, J. D., Fisher, A., Combes, S. A., Rolling with the Flow: Bumblebees Flying in Unsteady Wakes, The Journal of Experimental Biology, Vol. 216, No. 22 (2013),pp. 4299.

Ravi, S., Kolomenskiy, D., Engels, T., Schneider, K., Wang, C., Sesterhenn, J., Liu, H., Bumblebees Minimize Control Challenges by Combining Active and Passive Modes in Unsteady Winds, Scientific Reports, Vol. 6, No. 1 (2016),pp. 1-10.

Ristroph, L., Bergou, A. J., Ristroph, G., Coumes, K., Berman, G. J., Guckenheimer, J., Wang, Z. J., Cohen, I., Discovering the Flight Autostabilizer of Fruit Flies by Inducing Aerial Stumbles, Proceedings of the National Academy of Sciences, Vol. 107, No. 11 (2010),pp. 4820.

Ristroph, L., Ristroph, G., Morozova, S., Bergou, A. J., Chang, S., Guckenheimer, J., Wang, Z. J., Cohen, I., Active and Passive Stabilization of Body Pitch in Insect Flight, Journal of the Royal Society Interface, Vol. 10, No. 85 (2013),pp. 20130237.

Sane, S. P., Dieudonné, A., Willis, M. A., Daniel, T. L., Antennal Mechanosensors Mediate Flight Control in Moths, Science, Vol. 315, No. 5813 (2007),pp. 863.

Sun, M., Wang, J., Xiong, Y., Dynamic Flight Stability of Hovering Insects, Acta Mechanica Sinica, Vol. 23, No. 3 (2007),pp. 231-246.

Sun, M., Xiong, Y., Dynamic Flight Stability of a Hovering Bumblebee, The Journal of Experimental Biology, Vol. 208, No. 3 (2005),pp. 447.

Taylor, G. K., Thomas, A. L., Dynamic Flight Stability in the Desert Locust Schistocerca Gregaria, Journal of Experimental Biology, Vol. 206, No. 16 (2003),pp. 2803-2829.

Whitehead, S. C., Beatus, T., Canale, L., Cohen, I., Pitch Perfect: How Fruit Flies Control Their Body Pitch Angle, Journal of Experimental Biology, Vol. 218, No. 21 (2015),pp. 3508.

Windsor, S. P., Bomphrey, R. J., Taylor, G. K., Vision-Based Flight Control in the Hawkmoth Hyles Lineata, Journal of the Royal Society Interface, Vol. 11, No. 91 (2014),pp. 20130921.

Wu, J. H., Zhang, Y. L., Sun, M., Hovering of Model Insects: Simulation by Coupling Equations of Motion with Navier–Stokes Equations, Journal of Experimental Biology, Vol. 212, No. 20 (2009),pp. 3313-3329.

Xiong, Y., Sun, M., Dynamic Flight Stability of a Bumblebee in Forward Flight, Acta Mechanica Sinica, Vol. 24, No. 1 (2008),pp. 25-36.

Xu, R., Nakata, T., Cai, X., Liu, H., Intermittent Control Strategy Can Enhance Stabilization Robustness in Bumblebee Hovering, Bioinspiration & Biomimetics, Vol. 16, No. 1 (2020),pp. 016013.

Yao, J., Yeo, K. S., A Simplified Dynamic Model for Controlled Insect Hovering Flight and Control Stability Analysis, Bioinspiration & Biomimetics, Vol. 14, No. 5 (2019),pp. 056005.

Yao, J., Yeo, K. S., Forward Flight and Sideslip Manoeuvre of a Model Hawkmoth, Journal of Fluid Mechanics, Vol. 896, No. (2020),pp. A22.

Zhang, C., Hedrick, T. L., Mittal, R., An Integrated Study of the Aeromechanics of Hovering Flight in Perturbed Flows, AIAA Journal, Vol. 57, No. 9 (2019),pp. 3753-3764.

Zhang, X., Liu, H., A Three-Axis Pd Control Model for Bumblebee Hovering Stabilization, Journal of Bionic Engineering, Vol. 15, No. 3 (2018),pp. 494-504.

List of figures

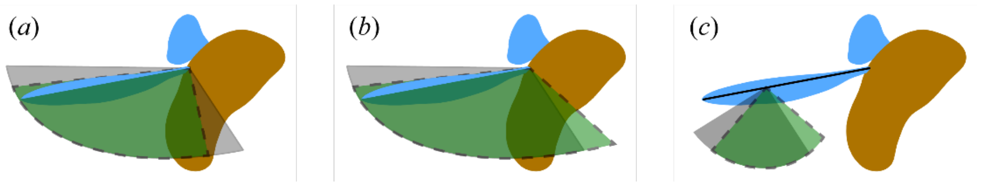

Figure 5.1 Variation of wing kinematics for longitudinal control: (*a*) positional angle amplitude $\Delta\Phi$, (*b*) mean positional angle $\Delta\bar{\varphi}$ and (*c*) mean feathering angle $\Delta\bar{\eta}$.

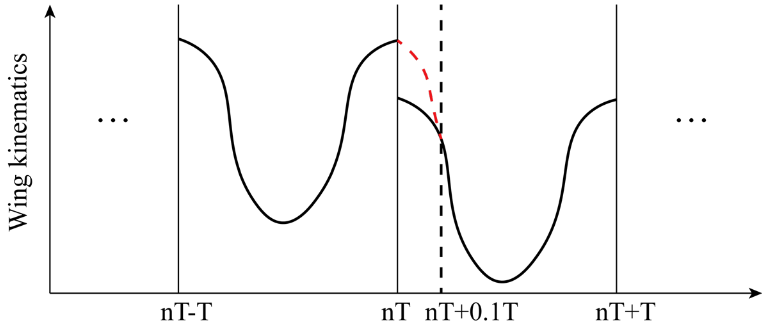

Figure 5.2 Smoothing wing kinematics between successive stroke cycles. Black curve: desired wing kinematics; red curve: smoothed transition.

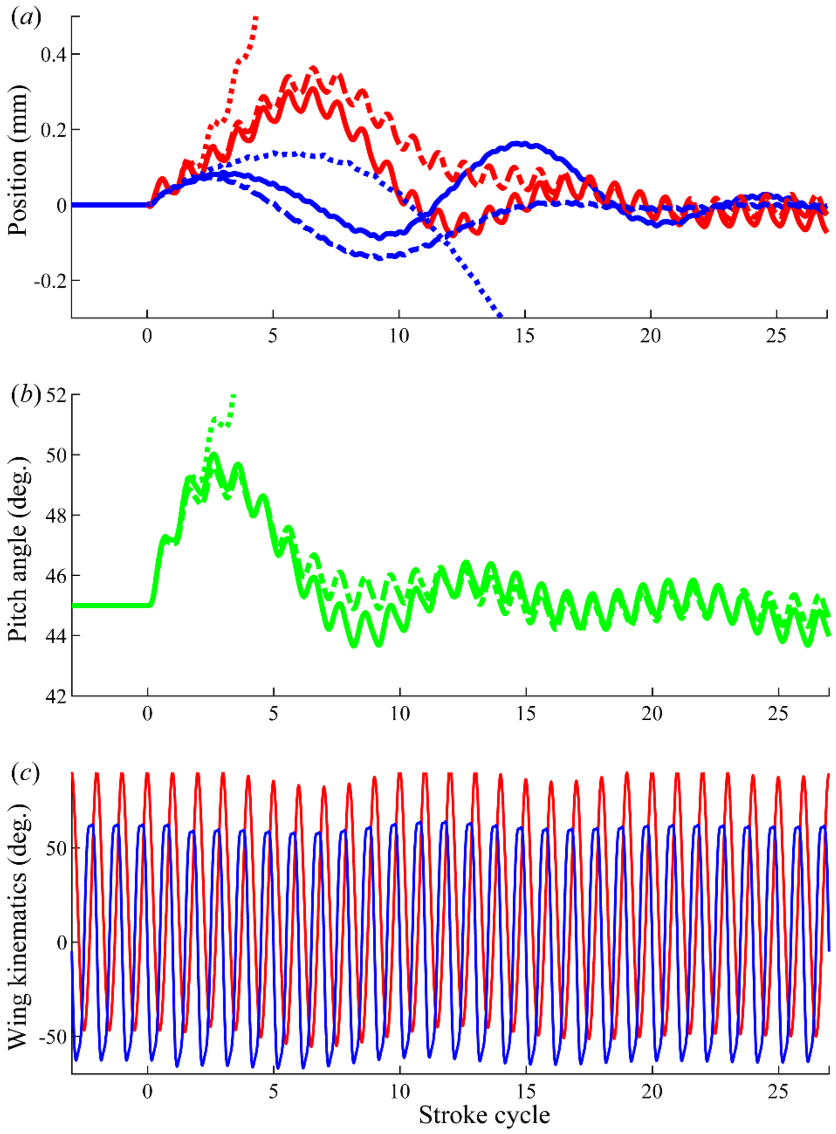

Figure 5.3 Longitudinal control process. (*a*) Position control and (*b*) pitch angle. Blue: Vertical position; Red: Forward/backward position; Green: Pitch angle. Solid line: Prediction by CFD; Dashed line: prediction by CDAM; Dotted line: Uncontrolled. (*c*) Variation of wing kinematics during control process. Red line: positional angle. Blue line: feathering angle.

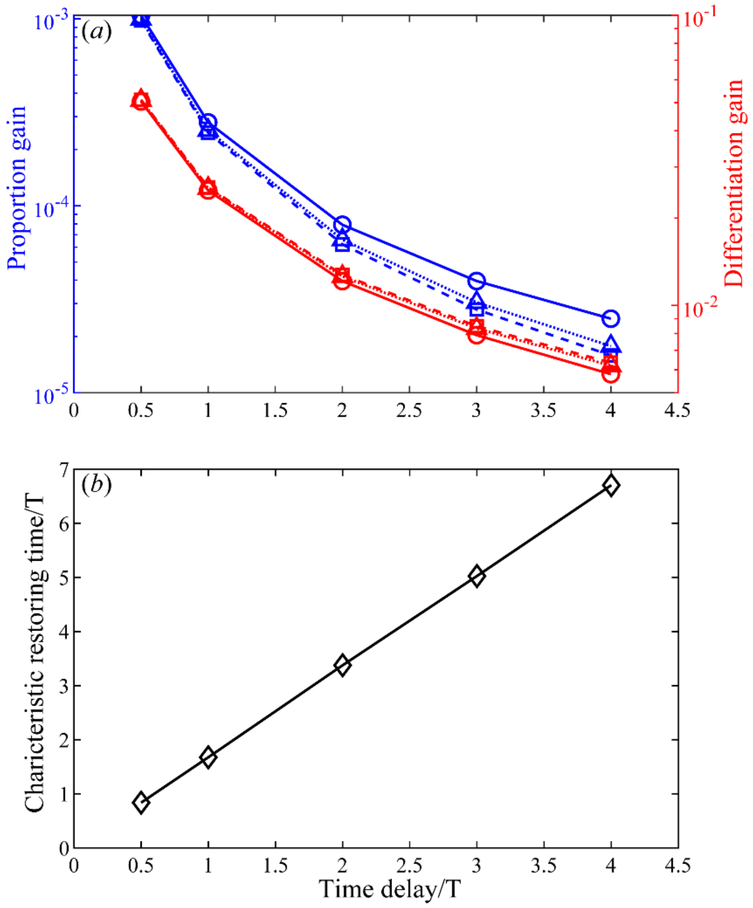

Figure 5.4 (*a*) Proportion gain k (blue) and derivative gain $k\tau$ (red) over time delay of longitudinal control. Solid line with circle: SISO system with damping effect λ_1. Dashed line with square: SISO system with damping effect λ_2. Dotted line with upper triangle: SISO system with damping effect λ_3. (*b*) closed-loop time constant over time delay of longitudinal control.

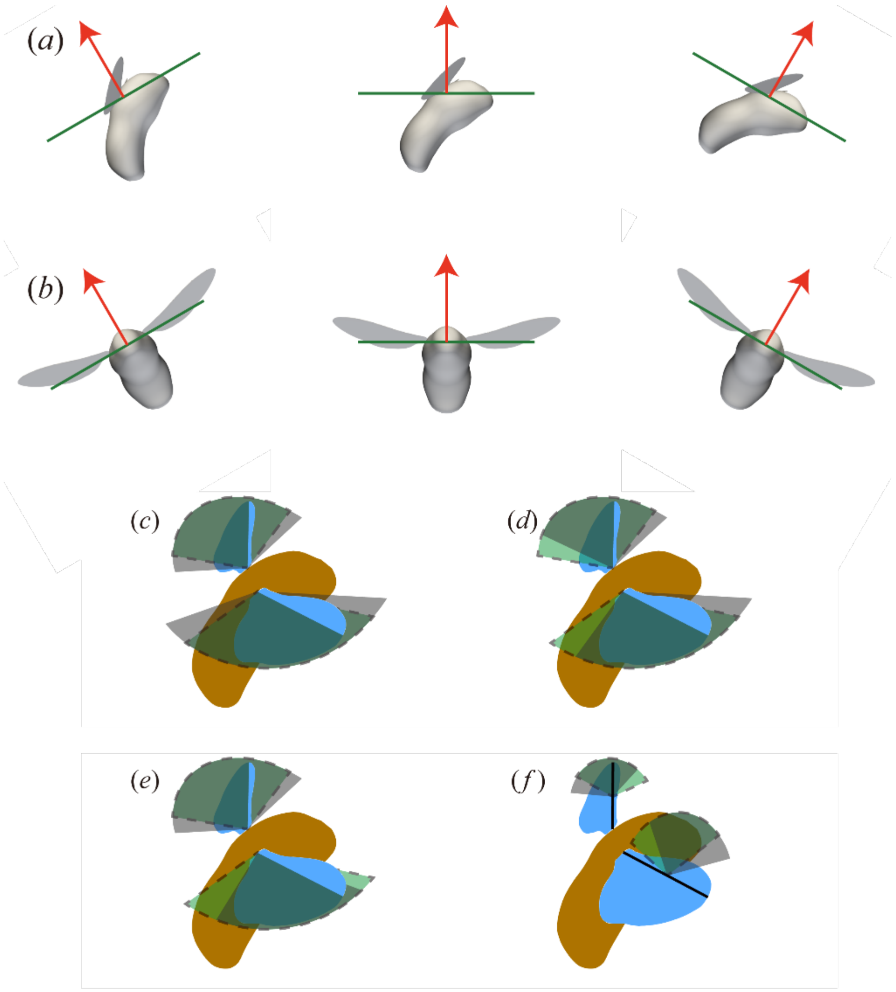

Figure 5.5 Effects of (*a*) pitch and (*b*) roll on the direction of force. Green line: the stroke plane; red arrow: aerodynamic force generated by the flapping wing. Variation of wing kinematics for 6 DoF control: (*c*) positional angle amplitude Φ, (*d*) mean positional angle $\bar{\varphi}$, (*e*) difference of positional angle amplitude between two wings Φ_{RL} and (*f*) difference of mean feathering angle between two wings $\bar{\eta}_{RL}$. Green region: hovering wing motions; gray region: variation of wing kinematics.

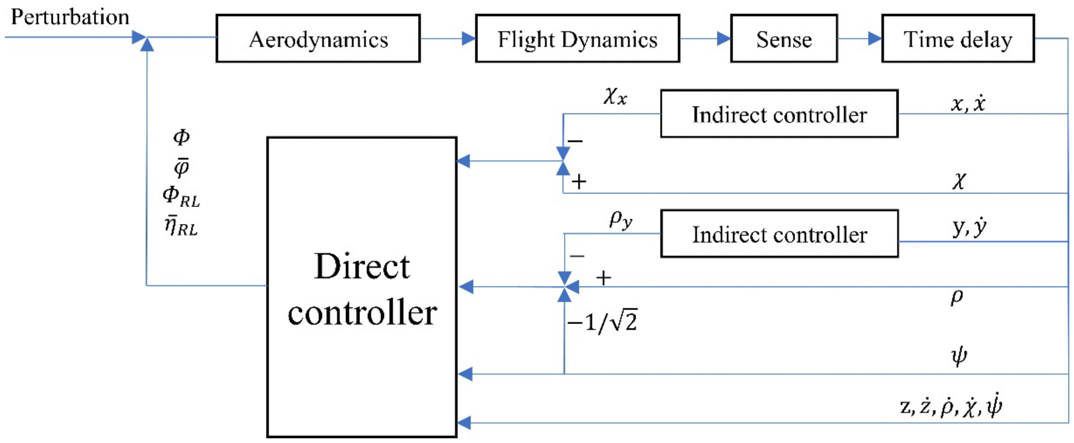

Figure 5.6 Schematic diagram of the closed-loop 6 DoF flight control system.

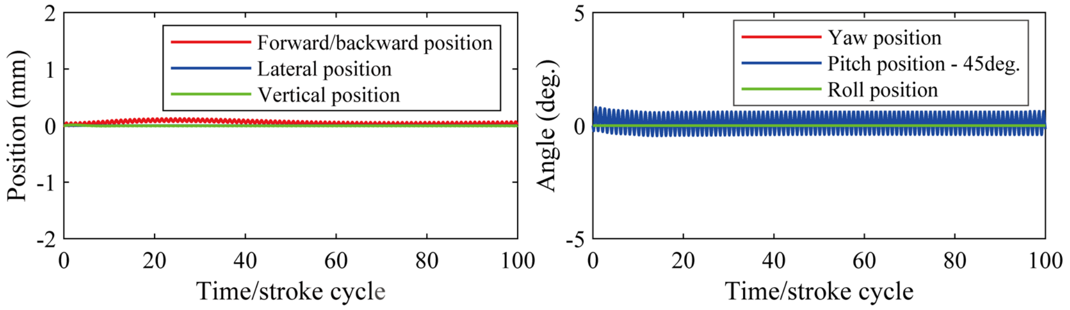

Figure 5.7 Trimmed state of a hovering bumblebee.

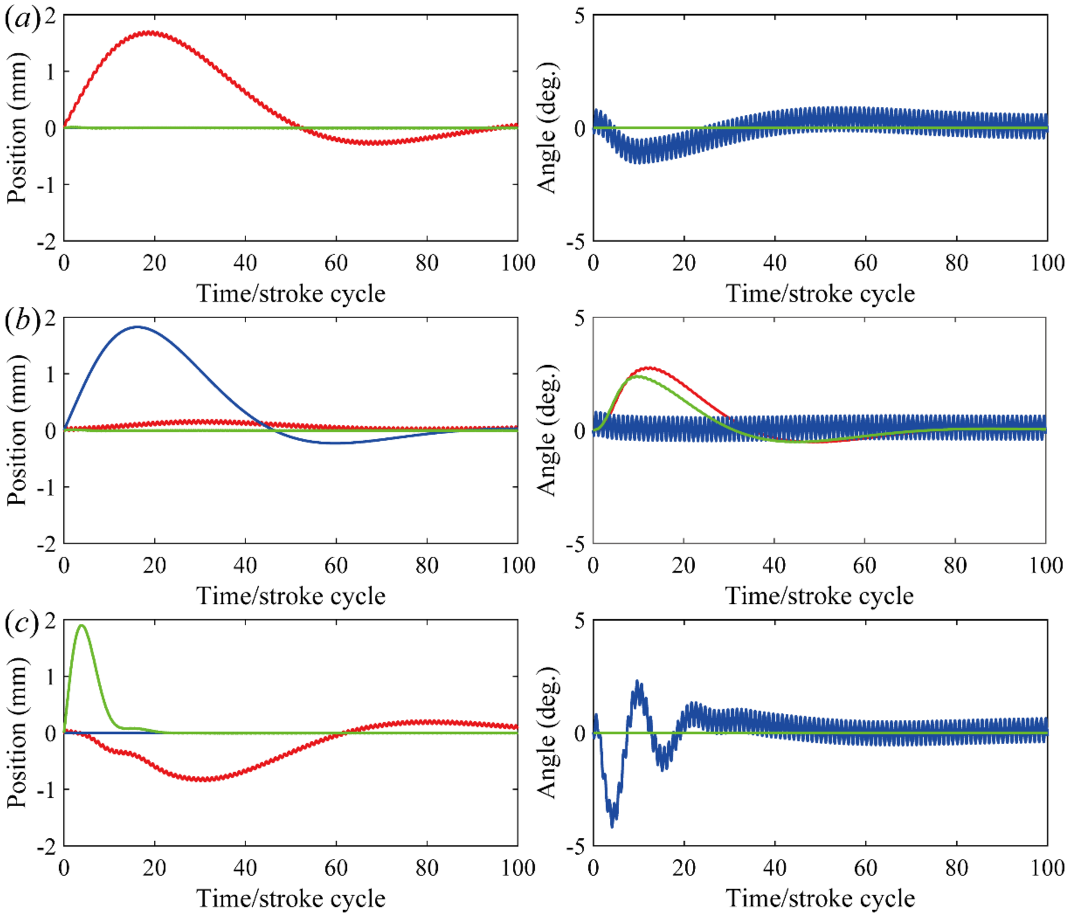

Figure 5.8 Stabilization control under small velocity perturbations. (*a*) forward perturbation; (*b*) lateral perturbation; (*c*) vertical perturbation. Refer to the legends in Figure 5.7 for the meanings of the colored curves.

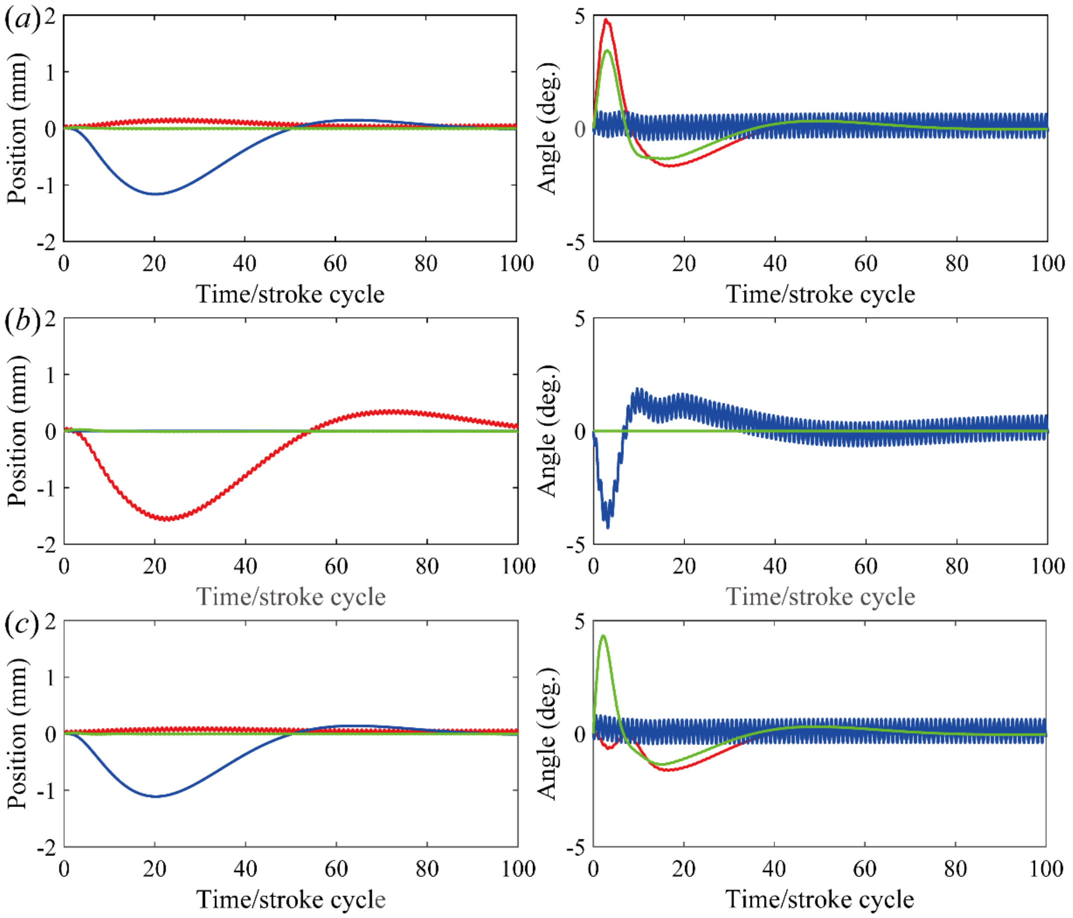

Figure 5.9 Stabilization control under small angular velocity perturbations. (a) perturbation along ${}_bz$; (b) perturbation along ${}_by$; (c) perturbation along ${}_bx$. Refer to the legends in Figure 5.7 for the meanings of the colored curves.

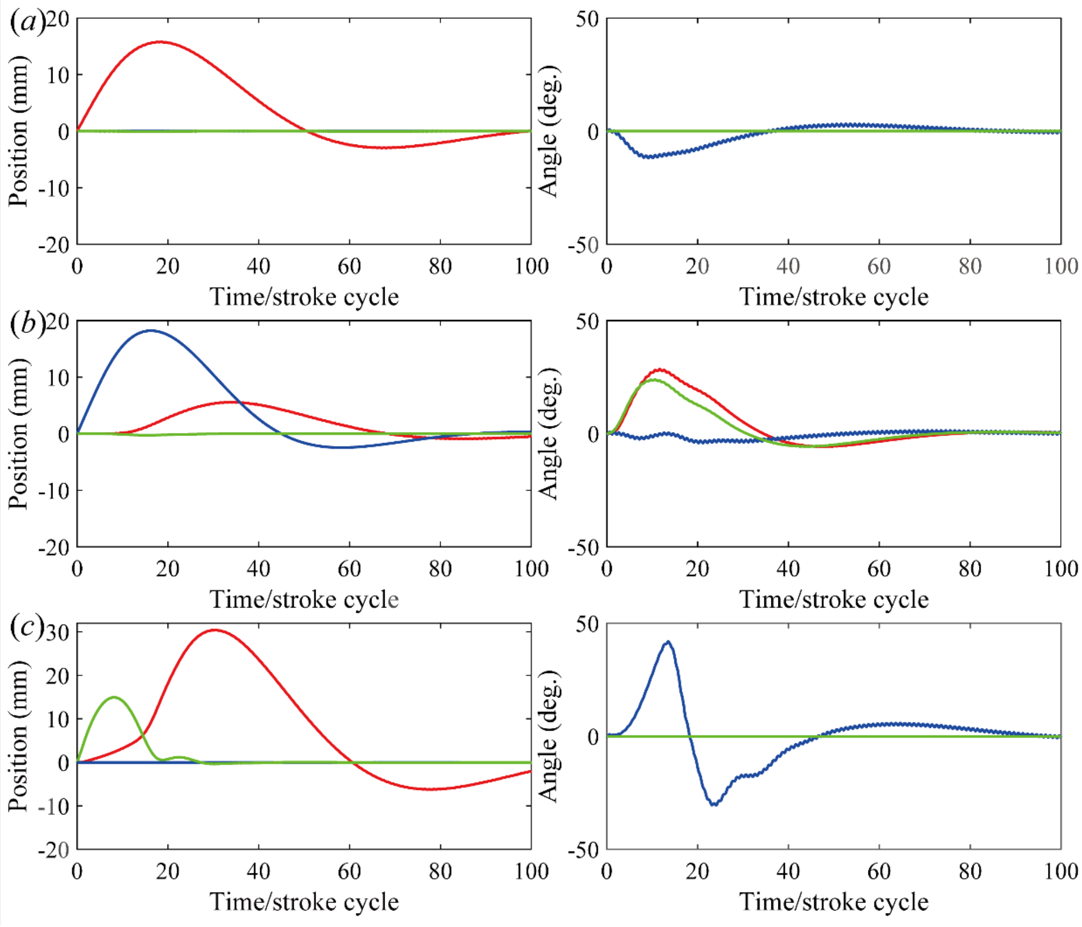

Figure 5.10 Stabilization control under large velocity perturbations. (*a*) forward perturbation; (*b*) lateral perturbation; (*c*) vertical perturbation. Refer to the legends in Figure 5.7 for the meanings of the colored curves.

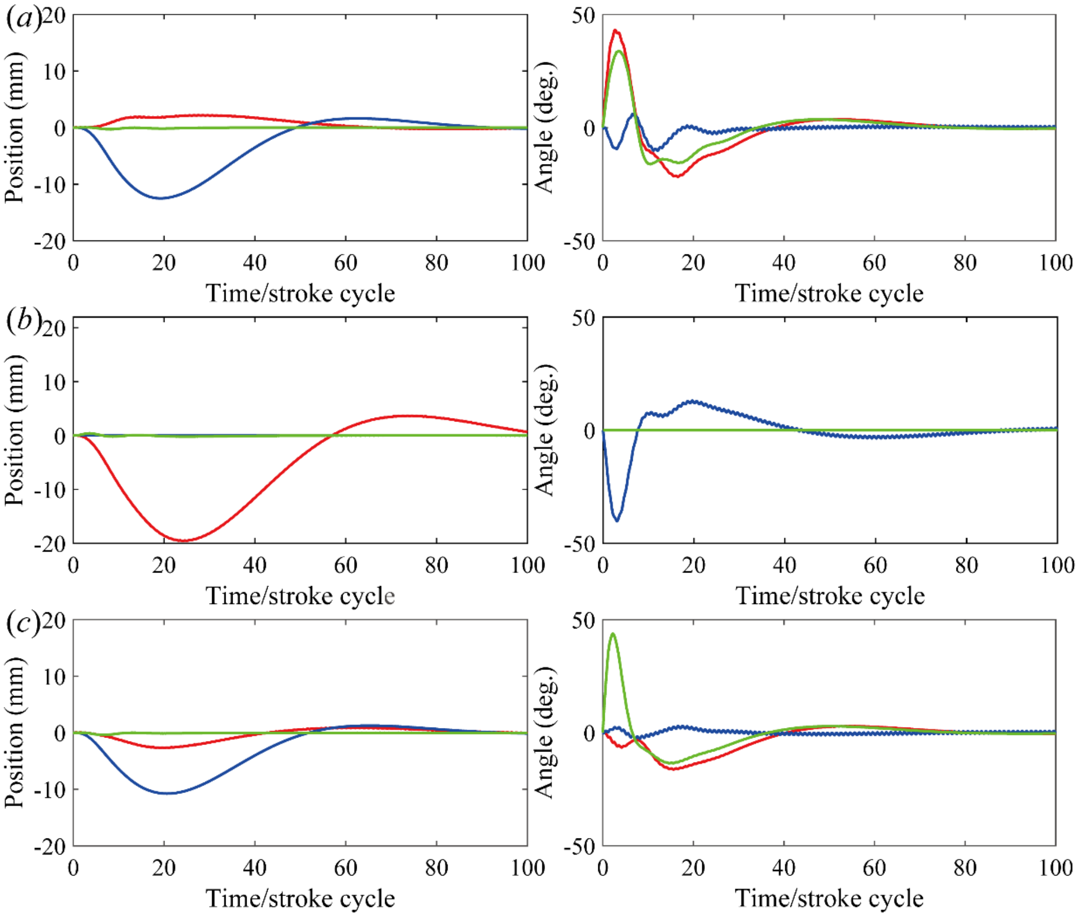

Figure 5.11 Stabilization control under large angular velocity perturbations. (*a*) perturbation along ${}_{b}z$; (*b*) perturbation along ${}_{b}y$; (*c*) perturbation along ${}_{b}x$. Refer to the legends in Figure 5.7 for the meanings of the colored curves.

List of tables

Table 5.1 Control parameters of PD control for longitudinal control.

k_1	τ_1	k_2	τ_2	k_3	τ_3
2.79×10^{-4}	89.24	2.46×10^{-4}	103.79	2.53×10^{-4}	100.13

Table 5.2 Poles corresponding to optimal control parameters for time delay of one stroke cycle for longitudinal control.

$p_{1,1}, p_{1,2}, p_{1,3}$	$p_{1,4}$	$p_{2,1}, p_{2,2}, p_{2,3}$	$p_{2,4}$	$p_{3,1}, p_{3,2}, p_{3,3}$	$p_{3,4}$
-0.034	-0.258	-0.033	-0.261	-0.033	-0.260

Table 5.3 Control parameters of the PD controller for 6 DoF control.

k_1	k_2	k_3	k_4	k_x	k_y
2.46×10^{-4}	2.78×10^{-4}	5.87×10^{-4}	3.29×10^{-4}	6.35×10^{-5}	6.37×10^{-5}
τ_1	τ_2	τ_3	τ_4	τ_x	τ_y
103.6	89.6	36.9	73.3	200	199

Chapter 6

6 Concluding remarks and future tasks

6.1 Conclusions

Simulation-based studies on the passive and active mechanisms underlying flying insects in terms of aerodynamic damping and structural flexibility are presented in this thesis. In order to facilitate the evaluation and analysis of insect flight, a CFD data-driven aerodynamic model is developed for fast and precise prediction of flapping unsteady aerodynamics as an alternative to costly numerical simulations. A versatile nonlinear dynamic model for pair-winged systems is also proposed to simulate the free or tethered flight of insects, of which the flapping wings are either actively controlled or passively driven.

Incorporating the CFD simulations of bumblebee hovering into the nonlinear dynamic model, it is found that the robust flapping dynamics can be achieved via elastic wing hinge modelled by torsional-spring model through fluid-structure interaction modeling. A strategy of active-controlled stroke, passive-controlled wing pitch and deviation achieves optimal elastic storage, and aerodynamic force generation high power efficiency over a broad range of wing-hinge stiffness. In addition, the aerodynamic performance is also essentially influenced by the occurrence of resonance.

Upon the simplified dynamic equation, a control-theoretic analysis framework based on a proportional-derivative (PD) control strategy in terms of Laplace transformation and root locus method is established. It is discovered that various insects and hummingbird achieve the fastest or minimized flight stabilization, given the passive aerodynamic damping and neural feedback delay. The passive aerodynamic damping can facilitate the flight stabilization while the neural feedback delay has disastrous implications.

A bioinspired PD controller is thereby designed for longitudinal and full 6 DoF flight control. The closed-loop nonlinear dynamic model is linearized around hovering, of which the aerodynamic effects are modelled by the CDAM. After decoupling the dynamic model from a MIMO system to multi SISO systems, the proportional and derivative gains are optimized following the Laplace transformation and root locus method. It is worth noting that the PD for

6 DoF is hierarchical that enables 6 DoF control with only 4 wing kinematics inputs. In addition, the PD controller generated from small perturbations is also applicable to large perturbations, showing the potential for the FMAVs autonomy.

6.2 Future tasks

6.2.1 Implementations to FMAVs

Up to now, most flapping-wing micro air vehicles (FMAVs) are designed without considering the elevation motion for one reason to reduce the complexity of fabrication and it turns out that the produced lift is enough to suspend the FMAVs. However, such design eliminating elevation is suboptimum. Setting the wing hinge along elevation to be flexible with appropriate stiffness can further improve the performance of FMAVs. In addition, the available controllers for FMAVs are rather complicated (Tu, Fei *et al.* 2020). The future work will attempt to incorporate the simple bioinspired PD controller proposed in this thesis to FMAVs

6.2.2 Active and passive roles of insect body

This thesis mainly focuses on the passive and active mechanisms of the insect flapping wings, while the insect body may also affect the flight dynamics, such as the stability and controllability (Luu, Cheung *et al.* 2011; Dyhr, Morgansen *et al.* 2013; Noda, Nakata *et al.* 2014). The abdomen of the insect body are found to be able to deflect about the thorax as a Stewart Platform (Liang, Zhao *et al.* 2019). There are two potential benefits by deflecting the abdomen relative to the thorax: first, the deflection to abdomen changes the configuration of insect body, resulting in a shift of the center of body mass, thereby the aerodynamic force generates a net torque; second, due to the conservation of angular momentum, a deflection of abdomen controlled by the action of the muscles at the thoracic–abdominal joint also induces a direction change of thorax, which redirect the aerodynamic force. How the insects adjust the flexible thoracic–abdominal joint to achieve flight control remains unknown.

References

Dyhr, J. P., Morgansen, K. A., Daniel, T. L., Cowan, N. J., Flexible Strategies for Flight Control: An Active Role for the Abdomen, The Journal of Experimental Biology, Vol. 216, No. 9 (2013),pp. 1523.

Liang, Y., Zhao, J., Yan, S., Cai, X., Xing, Y., Schmidt, A., Kinematics of Stewart Platform Explains Three-Dimensional Movement of Honeybee's Abdominal Structure, Journal of Insect Science, Vol. 19, No. 3 (2019),pp.

Luu, T., Cheung, A., Ball, D., Srinivasan, M. V., Honeybee Flight: A Novel 'Streamlining' Response, The Journal of Experimental Biology, Vol. 214, No. 13 (2011),pp. 2215.

Noda, R., Nakata, T., Liu, H., Body Flexion Effect on the Flight Dynamics of a Hovering Hawkmoth, Journal of Biomechanical Science and Engineering, Vol. 9, No. 3 (2014),pp. 14-00409-00414-00409.

Tu, Z., Fei, F., Zhang, J., Deng, X., An at-Scale Tailless Flapping-Wing Hummingbird Robot. I. Design, Optimization, and Experimental Validation, IEEE Transactions on Robotics, Vol. 36, No. 5 (2020),pp. 1511-1525.

Appendix

The expressions of the coefficients of equations (2.37) are listed as follows,

$$a_{1v} = 2m_w \tag{1}$$

$$A_{1o} = -m_w\left[R_{hR} + R_{wgR}\right]_\times - m_w\left[R_{hL} + R_{wgL}\right]_\times \tag{2}$$

$$B_{1wR} = -m_w\left[R_{wgR}\right]_\times \tag{3}$$

$$B_{1wL} = -m_w\left[R_{wgL}\right]_\times \tag{4}$$

$$\begin{aligned} a_1 = m_w &\left(- {}_b g + {}_b\omega_{bd} \times {}_b v_{cg} + {}_b\omega_{bd} \times \left({}_b\omega_{bd} \times \left(R_{hR} + R_{wgR}\right)\right)\right) \\ +m_w &\left(- {}_b g + {}_b\omega_{bd} \times {}_b v_{cg} + {}_b\omega_{bd} \times \left({}_b\omega_{bd} \times \left(R_{hL} + R_{wgL}\right)\right)\right) \end{aligned} \tag{5}$$

$$\begin{aligned} b_1 = m_w &\begin{bmatrix} \left(E_{wR2b}\dot{E}_{b2wR}\left({}_b\omega_{bd} + \omega_{R0b}\right)\right) \times R_{wgR} \\ +\left({}_b\omega_{bd} + \omega_{R0b}\right) \times \left(\omega_{R0b} \times R_{wgR}\right) + \omega_{R0b} \times \left({}_b\omega_{bd} \times R_{wgR}\right) \end{bmatrix} \\ +m_w &\begin{bmatrix} \left(E_{wL2b}\dot{E}_{b2wR}\left({}_b\omega_{bd} + \omega_{L0b}\right)\right) \times R_{wgL} \\ +\left({}_b\omega_{bd} + \omega_{L0b}\right) \times \left(\omega_{L0b} \times R_{wgL}\right) + \omega_{L0b} \times \left({}_b\omega_{bd} \times R_{wgL}\right) \end{bmatrix} \end{aligned} \tag{6}$$

$$A_{2vR} = m_w\left[R_{hR} + R_{wgR}\right]_\times \tag{7}$$

$$A_{2vL} = m_w\left[R_{hL} + R_{wgL}\right]_\times \tag{8}$$

$$A_{2oR} = -m_w\left[R_{hR} + R_{wgR}\right]_\times [R_{hR}]_\times - m_w[R_{hR}]_\times\left[R_{wgR}\right]_\times + E_{wR2b}I_w E_{b2wR} \tag{9}$$

$$A_{2oL} = -m_w\left[R_{hL} + R_{wgL}\right]_\times [R_{hL}]_\times - m_w[R_{hL}]_\times\left[R_{wgL}\right]_\times + E_{wL2b}I_w E_{b2wL} \tag{10}$$

$$\begin{gathered} a_{2R} = m_w\left(R_{hR} + R_{wgR}\right) \times \left(-\,{}_b g\right) + m_w\,{}_b v_{cg} \times \left({}_b\omega_{bd} \times \left(R_{hR} + R_{wgR}\right)\right) \\ +m_w\,{}_b\omega_{bd} \times \left[\left(R_{hR} + R_{wgR}\right) \times \left({}_b v_{cg} + {}_b\omega_{bd} \times R_{hR}\right) + R_{hR} \times \left({}_b\omega_{bd} \times R_{wgR}\right)\right] \\ + {}_b\omega_{bd} \times \left(E_{wR2b} I_w E_{b2wR}\,{}_b\omega_{bd}\right) \end{gathered} \tag{11}$$

$$\begin{gathered} a_{2L} = m_w\left(R_{hL} + R_{wgL}\right) \times \left(-\,{}_b g\right) + m_w\,{}_b v_{cg} \times \left({}_b\omega_{bd} \times \left(R_{hL} + R_{wgL}\right)\right) \\ +m_w\,{}_b\omega_{bd} \times \left[\left(R_{hL} + R_{wgL}\right) \times \left({}_b v_{cg} + {}_b\omega_{bd} \times R_{hL}\right) + R_{hL} \times \left({}_b\omega_{bd} \times R_{wgL}\right)\right] \\ + {}_b\omega_{bd} \times \left(E_{wL2b} I_w E_{b2wL}\,{}_b\omega_{bd}\right) \end{gathered} \tag{12}$$

$$\begin{gathered} b_{2R} = m_w R_{hR} \times \left[\left(\omega_{R0b} + {}_b\omega_{bd}\right) \times \left(\dot{E}_{wR2b} E_{b2wR} R_{wgR}\right)\right] \\ +\dot{E}_{wR2b} I_w\left(E_{b2wR}\omega_{R0b} + E_{b2wR}\,{}_b\omega_{bd}\right) + E_{wR2b} I_w \dot{E}_{b2wR}\omega_{R0b} \\ + {}_b\omega_{bd} \times \left(E_{wR2b} I_w E_{b2wR}\omega_{R0b}\right) + E_{wR2b} I_w \dot{E}_{b2wR}\,{}_b\omega_{bd} \\ +m_w\,{}_b\omega_{bd} \times \left(R_{hR} \times \left(\omega_{R0b} \times R_{wgR}\right)\right) \\ +m_w\left(\dot{E}_{wR2b} E_{b2wR} R_{wgR}\right) \times \left({}_b v_{cg} + {}_b\omega_{bd} \times R_{hR}\right) \\ +m_w\,{}_b v_{cg} \times \left(\omega_{R0b} \times R_{wgR}\right) \end{gathered} \tag{13}$$

$$\begin{gathered} b_{2L} = m_w R_{hL} \times \left[\left(\omega_{L0b} + {}_b\omega_{bd}\right) \times \left(\dot{E}_{wL2b} E_{b2wL} R_{wgL}\right)\right] \\ +\dot{E}_{wL2b} I_w\left(E_{b2wL}\omega_{L0b} + E_{b2wL}\,{}_b\omega_{bd}\right) + E_{wL2b} I_w \dot{E}_{b2wL}\omega_{L0b} \\ + {}_b\omega_{bd} \times \left(E_{wL2b} I_w E_{b2wL}\omega_{L0b}\right) + E_{wL2b} I_w \dot{E}_{b2wL}\,{}_b\omega_{bd} \\ +m_w\,{}_b\omega_{bd} \times \left(R_{hL} \times \left(\omega_{L0b} \times R_{wgL}\right)\right) \\ +m_w\left(\dot{E}_{wL2b} E_{b2wL} R_{wgL}\right) \times \left({}_b v_{cg} + {}_b\omega_{bd} \times R_{hL}\right) \\ +m_w\,{}_b v_{cg} \times \left(\omega_{L0b} \times R_{wgL}\right) \end{gathered} \tag{14}$$

where $[\cdot]_\times$ is the cross product matrix defined as

$$[a]_\times = \begin{bmatrix} 0 & -a_3 & a_2 \\ a_3 & 0 & -a_1 \\ -a_2 & a_1 & 0 \end{bmatrix} \tag{15}$$

The expressions of the coefficients of equations (2.38),

$$C_{vR} = m_w [R_{hR}]_\times \tag{16}$$

$$C_{vL} = m_w [R_{hL}]_\times \tag{17}$$

$$C_{oR} = -m_w [R_{hR}]_\times \left[R_{hR} + R_{wgR}\right]_\times \tag{18}$$

$$C_{oL} = -m_w [R_{hl}]_\times \left[R_{hl} + R_{wgL}\right]_\times \tag{19}$$

$$C_{wR} = -m_w [R_{hR}]_\times [R_{wgR}]_\times \tag{20}$$

$$C_{wL} = -m_w [R_{hL}]_\times [R_{wgL}]_\times \tag{21}$$

$$\begin{gathered} c_R = m_w [R_{hR}]_\times [\,{}_b\omega_{bd}]_\times (\,{}_b v_{cg} + \,{}_b\omega_{bd} \times R_{hR}) \\ + m_w [R_{hR}]_\times [\,{}_b\omega_{bd} + \omega_{R0b}]_\times (\dot{E}_{wR2b} E_{b2wR} R_{wgR}) + \\ m_w [R_{hR}]_\times [\,{}_b\omega_{bd}]_\times [\,{}_b\omega_{bd} + \omega_{R0b}]_\times R_{wgR} - m_w R_{hR} \times \,{}_b g - R_{hR} \times \,{}_b F_{a,R} \end{gathered} \tag{22}$$

$$\begin{gathered} c_L = m_w [R_{hL}]_\times [\,{}_b\omega_{bd}]_\times (\,{}_b v_{cg} + \,{}_b\omega_{bd} \times R_{hL}) \\ + m_w [R_{hL}]_\times [\,{}_b\omega_{bd} + \omega_{L0b}]_\times (\dot{E}_{wL2b} E_{b2wL} R_{wgL}) + \\ m_w [R_{hL}]_\times [\,{}_b\omega_{bd}]_\times [\,{}_b\omega_{bd} + \omega_{L0b}]_\times R_{wgL} - m_w R_{hL} \times \,{}_b g - R_{hL} \times \,{}_b F_{a,L} \end{gathered} \tag{23}$$